2016

# Radioprotective Cerium Oxide Nanoparticles: Molecular Imaging Investigations of CONPs' Pharmacokinetics, Efficacy, and Mechanisms of Action

Philip R. McDonagh III
*Virginia Commonwealth University*

# RADIOPROTECTIVE CERIUM OXIDE NANOPARTICLES: MOLECULAR IMAGING INVESTIGATIONS OF CONPs' PHARMACOKINETICS, EFFICACY, AND MECHANISMS OF ACTION

A dissertation submitted in partial fulfillment of the requirements for the degree of Doctor of Philosophy in Cancer and Molecular Medicine at Virginia Commonwealth University.

by
Philip Reed Wills McDonagh III
Bachelor of Science in Physics in Medicine
University of Notre Dame, Notre Dame, Indiana, 2009

Director: Jamal Zweit, PhD, DSc
Professor, Department of Radiology
Director, Center for Molecular Imaging

Co-Director: Ross B. Mikkelsen, PhD
Professor and Division Chair, Molecular Radiobiology, Radiation Oncology

Virginia Commonwealth University
School of Medicine
Richmond, Virginia
May 11th, 2016

# Abstract

RADIOPROTECTIVE CERIUM OXIDE NANOPARTICLES: MOLECULAR IMAGING INVESTIGATIONS OF CONPS' PHARMACOKINETICS, EFFICACY, AND MECHANISMS OF ACTION

By Philip Reed Wills McDonagh III, BS

A dissertation submitted in partial fulfillment of the requirements for the degree of Doctor of Philosophy in Cancer and Molecular Medicine at Virginia Commonwealth University.

Virginia Commonwealth University, 2016

Director: Jamal Zweit, PhD, DSc
Professor, Department of Radiology
Director, Center for Molecular Imaging

Cerium oxide nanoparticles (CONPs) are being investigated for several anti-oxidant applications in medicine. One of their most promising applications is as a radioprotective drug, an area of research in need due to the severe side effects from radiation therapy. In this work, the potential of CONPs as a radioprotective drug is examined using four criteria: favorable biodistribution/pharmacokinetics, low toxicity, ability to protect normal tissue from radiation damage, and lack of protection of tumor. The mechanisms of action of CONPs are also studied. Biodistribution was determined in radiolabeled CONPs with surface coatings including citrate, dextran T10-amine (DT10-NH$_2$), dextran T10-polyethylene glycol (DT10-PEG), dextran T10-sulfobetaine (DT10-SB) and poly(acrylic acid) (PAA), and compared to uncoated. $^{89}$Zr was incorporated into CONPs for positron emission tomography (PET) imaging and *ex vivo* tissue analysis in tumor bearing mice. Compared to uncoated [$^{89}$Zr]CONPs, coated [$^{89}$Zr]CONPs

showed improved biodistribution, including significantly enhanced renal clearance of PAA-$[^{89}$Zr]CONPs. The toxicity of CONPs was evaluated *in vitro* and *in vivo,* with low toxicity at therapeutic doses. After clinically mimetic radiation therapy, pre-treatment of mice with coated and uncoated CONPs showed greater than 50% reduction of cell death in normal colon tissue, comparable to the clinically available radioprotective drug amifostine. Tumor control after irradiation of spontaneous colon tumors was unchanged with PAA-CONP pre-treatment, while citrate, DT10-PEG, and uncoated CONP pre-treatment had slightly less tumor control. Xenograft tumors were irradiated after pH normalizing treatment with sodium bicarbonate and PAA-CONP pre-treatment. Treatment of these tumors showed slightly less tumor control than irradiation alone or PAA-CONP plus irradiation, demonstrating that the acidic pH of the tumor microenvironment may be the basis of preventing CONPs' radioprotective properties in tumor. These studies show that, among the variations of CONPs tested, PAA-CONP shows the most promise for its good biodistribution and quick clearance, low toxicity, ability to protect normal tissue, and lack of protection of tumor, meeting all the criteria set forth for an ideal radioprotective drug. Further studies on the effects of pH on CONPs actions may further elucidate their mechanisms of action, advancing them as a candidate for use as a radioprotective drug during radiation therapy.

# Acknowledgements

I would like to first thank my advisor, Dr. Jamal Zweit, who has been an amazing mentor for me, giving me guidance when needed, but giving me the freedom to make this project my own. His knowledge base in molecular imaging is unmatched and I leave with a much better understanding and a great appreciation for the field. I appreciate the time that he always made for me when I had questions or needed critiques, and always motivating me to succeed.

Dr. Zweit's lab, the Center for Molecular Imaging (CMI), has many present and past members who must be named for the immense support and camaraderie they provided. Dr. Sundaresan Gobalakrishnan provided PET imaging support, but much more than that he was a second mentor in the CMI who helped design and critique many of my experiments. Dr. Likun Yang and Dr. Minghao Sun taught me everything I needed to know about nanoparticle synthesis and characterization and were always willing to lend a helping hand when needed. Purnima Jose provided help with the cell biology experiments and always had a cheerful attitude that made my day brighter. Li Wang was there through almost every experiment helping me, which was such a huge help because she almost always could get things done faster than me. Dr. Vimalan Vijayaragavan provided the MRI imaging support and thankfully withstood and exceeded my expectations as the pressure was on finishing my final experiments. Celina Thadigiri was also always there, happy to help whenever I needed it. Past PhD students Naru Lamichhane and David Hoffman gave me a great examples of how students should approach and develop research projects and became close friends. Most importantly, the CMI felt like a home for me where the lab members were not only my colleagues, but also my friends who helped make it easy to always do my research with a smile.

I would also like to especially thank Dr. Ross Mikkelsen, my co-advisor. He and his lab were such a crucial support for the radiation aspects of my project and allowed the project to become a truly translational work. His expertise in radiobiology was a resource that I relied on heavily and his mentorship in helping me develop the radiation studies was invaluable. I would like to also thank two members of Dr. Mikkelsen's lab, Asim Alam and Chris Rabender, who taught me many of the techniques used for irradiation, radiobiology assays, and microscopy. Asim was also a huge help with animal care for mice in the AOM/DSS protocol.

An additional thank you to the others who assisted this project, including former medical physics PhD student Chris Bass introduced me to the small animal radiation research platform (SARRP) system and taught me all the important ways to troubleshot when it inevitably would have an error. Thanks to Dr. Joseph Turner who provided the support for inductively coupled plasma measurements and never complained when I was predictably late to show up to the other campus for my appointment or left my USB drive behind.

I would like to thank my family, my parents Cindy and Phil McDonagh, for their unending support and for raising me to pursue my passions, and my sister Sheridan for helping give me confidence to take on so much. I certainly wouldn't be here doing what I love without their love and guidance. To my friends along the way, you helped shape my life into what it is and I'm so thankful for your support. Finally, to my girlfriend Cori Atkinson, thank you for sticking with me through the tough times finishing up my work. I look forward to you being by my side through the rest of my journey through academia.

# Vita

Philip Reed Wills McDonagh III was born December 13th, 1986 in Annapolis, Maryland and is an American Citizen. He graduated from St. Mary's Ryken College Preparatory School, Leonardtown, Maryland in 2005. He received his Bachelor of Science in Physics in Medicine from University of Notre Dame, Notre Dame, Indiana in 2009. In June 2010 he entered the MD/PhD graduate program at Virginia Commonwealth University School of Medicine.

# Table of Contents

# List of Tables

# List of Figures

xiii

xvi

xviii

# List of Abbreviations

The reader is assumed to possess basic knowledge of measurement units and their prefixes, scientific symbols, and abbreviations in common usage. Examples are meters (m), grams (g), liters (L), kilo- (k), Fluorine-18 ($^{18}$F), Zirconium-89 ($^{89}$Zr), deoxyribonucleic acid (DNA). Where appropriate, units were chosen to be consistent with those employed by other investigators in the field. Some quantities are therefore non in SI units, such as mCi.

| | |
|---|---|
| %ID/g | Percent injected dose per gram |
| [$^{18}$F]-FDG | [$^{18}$F]-fluorodeoxyglucose |
| [$^{18}$F]-FLT | [$^{18}$F]-fluorothymidine |
| 3D-CRT | Three dimensional conformal radiation therapy |
| AcOH | Acetic Acid |
| APUD | Amine precursor uptake and decarboxylation |
| BEC | Blood endothelial cells |
| BSA | Bovine serum albumin |
| CAF | Cancer associated fibroblasts |
| CEST | Chemical exchange saturation transfer |
| CHT | Choline transporter |
| CNT | Concentrative nucleoside transporter |

| | |
|---|---|
| COLO-205 | Dukes' type D, colorectal adenocarcinoma cell line |
| CONP | Cerium oxide nanoparticle |
| CT | Computed tomography |
| Cu(ATSM) | Copper(II)-diacetyl-bis($N^4$-methylthiosemicarbazone) |
| DAT | Dopamine transporter |
| DFO | Desferoxamine |
| DIPEA | N,N-Diisopropylethylamine |
| DLS | Dynamic light scattering |
| DMSO | Dimethyl sulfoxide |
| DOTA-TOC | 1,4,7,10-tetraazacyclododecane-1,4,7,10-tetraacetic acid - $Tyr^3$-Octreotide |
| DSC | di(N-succinimidyl)carbonate |
| DTPA | Diethylenetriaminepentaacetic acid |
| dUTP | Deoxyuridine triphosphate |
| ECM | Extracellular matrix |
| EDTA | Ethylenediaminetetraacetic |
| EDTMP | ethylenediamine tetra(methylene phosphonic acid) |
| EGFR | Epidermal growth factor receptor |
| ENT | Equilibrative nucleoside transporter |
| FAZA | Fluoroazomycin arabinoside |
| FDA | United States Food and Drug Administration |
| FDOPA | 3,4-dihydroxy-6-fluoro-l-phenylalanine |
| FES | Fluoroestradiol |

| | |
|---|---|
| FET | Fluoro-ethyl-tyrosine |
| FHBG | Fluoro-3-hydroxymethylbutyl)guanine |
| GLUT | Glucose transporter |
| GRP | Glucose regulated protein |
| HCT-116 | Colorectal carcinoma cell line |
| HDR | High dose rate |
| HTP | 5-hydroxy-L-tryptophan |
| IACUC | Institutional Animal Care and Use Committee |
| ICP-OES | Inductively coupled plasma – optical emission spectrometry |
| IMRT | Intensity-modulated radiation therapy |
| LAT | L-amino acid transporter |
| LDR | Low dose rate |
| LEC | Lymphatic endothelial cells |
| LOR | Line of response |
| MET | Methionine |
| MISO | Misonidazole |
| MLC | Multileaf collimator |
| MR | Magnetic resonance |
| MRI | Magnetic resonance imaging |
| MSC | Mesenchymal stem cells |
| MW | Molecular weight |
| MWCO | Molecular weight cutoff |
| NET | Norepinephrine transporter |
| NP | Nanoparticle |

| | |
|---|---|
| OCT | Optimal cutting temperature |
| PAA | Poly(acrylic acid) |
| PEG | Polyethylene glycol |
| PET | Positron emission tomography |
| RCF | Relative centrifugal force |
| RES | Reticuloendothelial system |
| RF | Radiofrequency field |
| RGD | Arginylglycylaspartic acid |
| ROI | Region of interest |
| RPM | Rotations per minute |
| SEM | Standard error of the mean |
| SERT | Serotonin transporter |
| SNARF | Seminaphtharhodafluor |
| SPECT | Single photon emission tomography |
| SPION | Superparamagnetic iron oxide nanoparticle |
| SUV | Standardized uptake value |
| T1 | Longitudinal relaxation time |
| T2 | Transverse relaxation time |
| TdT | Terminal deoxynucleotidyl transferase |
| TE | Echo time |
| TME | Tumor microenvironment |
| TOA | Trioctylamine |
| TR | Repetition time |
| TUNEL | Terminal deoxynucleotidyl transferase deoxyuridine triphosphate nick end labeling |

| UT | Ultrasound |
| UV | Ultraviolet |
| VEGFR | Vascular endothelial growth factor receptor |

# Thesis Organization

This thesis is divided into seven chapters. The first chapter is a general introduction to the project, including an overview of cerium oxide nanoparticles (CONPs) as a radioprotective drug, the hypothesis being tested, and strategies to test that hypothesis. The second chapter discusses the background and significance of the project, giving an overview of the rationale for the research and the development of the many techniques used. The third chapter details the methods used to accomplish the goals of the project. Chapter 4 gives the results of the research and Chapter 5 discusses the impact of these results. Chapter 6 summarizes all the findings in conclusion. Finally, Chapter 7 discusses future work as research continues with CONPs as radioprotective drugs and are aimed towards applications in other medical areas and clinical trials.

# 1. Chapter 1 – General Introduction

## *1.1.  Radioprotective Drugs and Cerium Oxide Nanoparticles*

The study of drug therapies to reduce side effects from radiation therapy is a promising area of research for its implications on improving quality of life of patients and the curative effects of cancer radiation therapy. Currently, very few drugs are available for treatment of radiation therapy side effects, but many are being studied as the mechanisms of radiation cell damage and methods to prevent them are being better understood. Agents that are able to prevent radiation damage are likely to be antioxidant, with the ability to reduce radiation-produced radical species and prevent them from damaging cellular components, especially DNA. An antioxidant agent should have several qualities that would make it ideal for use as a radioprotective agent in the setting of radiation therapy. These qualities include: 1) *Favorable biodistribution/pharmacokinetics* – the agent should reach the tissue that would be damaged by radiation, with proper clearance and higher uptake in normal tissues than cancerous tissue, 2) *Low toxicity* – the agent should not cause more side effects than expected from radiation therapy, 3) *Minimal protection of cancerous tissue* – the radioprotective effects should be absent or minimal in cancerous tissue so that the tumor control by the radiation treatment is not significantly altered, and finally 4) *Protection of normal tissue* – the agent should reduce radiation damage to normal cells in the area of radiation therapy to the point where side effects can be reduced and quality of life can be improved. This projects aims to determine if cerium

2

oxide nanoparticles (CONPs) meet these criteria and show promise for use in the clinic, using molecular imaging techniques.

## 1.2. Hypothesis and Aims

The hypothesis of this project is that *CONPs are radioprotective in a pH dependent manner and altering surface chemistry can improve pharmacokinetics and advance application to reduce/prevent side effects in the setting of cancer patients treated with radiation therapy.*

The aim of this research is to develop, characterize, and evaluate several coated cerium oxide nanoparticles for their application as a radioprotective drug. The specific objectives of this project are:

1. Optimize synthesis and characterization of coated and radiolabeled CONPs
2. Use molecular imaging to determine and compare biodistribution and pharmacokinetics of coated and uncoated CONPs
3. Compare coated and uncoated CONPs in terms of *in vivo* radioprotection
4. Determine if CONPs' radioprotection is dependent on pH environment

## 1.3. Strategy

This project aims to examine cerium oxide nanoparticles (CONPs) as a potential radioprotective agent using a variety of nanosynthesis, molecular imaging, and pre-clinical radiation therapy techniques.

### 1.3.1. Synthesis of Coated CONPs

Utilizing the intrinsic ability to alter the surface chemistry of nanoparticles by addition of small molecules or polymers, five coated CONPs will be tested and compared to uncoated CONPs.

3

The five coatings on CONP will include citric acid/ethylenediaminetetraacetic acid (EDTA), henceforth simplified to "citrate," dextran T10-amine (DT10-NH$_2$), dextran T10-polyethylene glycol (DT10-PEG), dextran T10-sulfobetaine (DT10-SB), and polyacrylic acid (PAA). These coatings will alter the size and surface charge of the nanoparticles, dependent on the properties of the coating molecules, and will affect their biodistribution and pharmacokinetics accordingly.

### 1.3.2. Intrinsically Radiolabeled CONPs with $^{89}$Zr

CONPs' biodistribution and pharmacokinetics will be examined through molecular imaging of $^{89}$Zr radiolabeled CONPs for PET imaging and *ex vivo* biodistribution. The synthesis of CONPs can be altered with the addition of $^{89}$ZrCl$_2$ to intrinsically incorporate the isotope into the core of the nanoparticles, as seen in **Figure 1B**.[1] This method is more stable than the chelator model of radiolabeling, seen in **Figure 1A**, preventing the release of isotope and corresponding loss of coordinated radioactivity and nanoparticle concentration, and avoiding alteration of surface chemistry. The $^{89}$Zr isotope is a clinically relevant PET imaging isotope and allows for both high activity PET imaging, including dynamic scans which create a video of the distribution of the nanoparticles over the first hour after injection, and *ex vivo* biodistribution to more precisely measure uptake in specific organs.
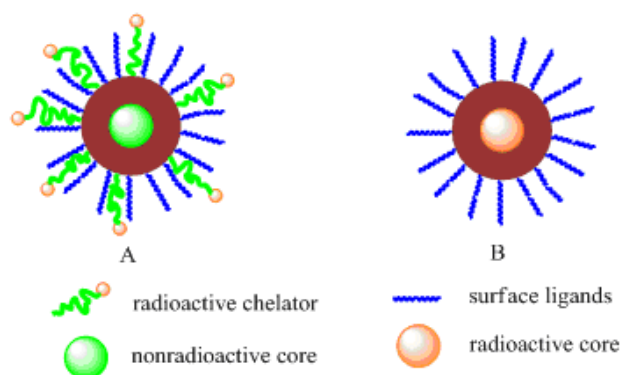


**Figure 1:** A) External radiolabeling of nanoparticles using the radioactive chelator model, compared to B) the radio-intrinsic model, which incorporates the radioactive isotope into the core of the nanoparticle. Reproduced from Journal of Materials Chemistry B, **Ref. 1**, copyright 2014, with permission of The Royal Society of Chemistry.

### 1.3.3. Pre-clinical Radiation Therapy and Colon Cancer Tumor Model

Mice with and without cancer are treated with CONPs and undergo clinic mimicking radiation therapy to examine effects on normal and cancerous tissue. A small animal radiation research platform (SARRP) is able to mimic clinical conformal radiation therapy in animal models. The platform simulates doses, cell damage, and side effects produced by clinical radiation therapy by delivery precision doses of radiation to collimated areas, guided by CT imaging. While normal C57BL/6 mice are used to examine the results of radiation on normal tissue, a spontaneous colon cancer tumor model was used to examine results of radiation on cancerous tissue. This model better mimics the spontaneous tumors of cancer patients, compared to xenograft tumor bearing mice. Response to therapy is monitored by apoptosis labeling of *ex vivo* colon slices and [$^{18}$F]FDG PET imaging to determine tumor metabolic activity.

### 1.3.4. Molecular Imaging of pH and Effects of Tumor Microenvironment on CONP Radioprotection

The mechanisms of CONPs' action will be examined in the context of the tumor microenvironment (TME), specifically in regards to the acidic pH of tumors. *In vivo* imaging of pH is a developing field, and an MR imaging technique utilizing a clinically available contrast agent was used. This method utilizes chemical exchange saturation transfer (CEST) imaging to selectively saturate several exchangeable protons in the contrast agent that have pH specific response, allowing for concentration independent ratiometric pH mapping overlaid on MRI images. This *in vivo* measurement of pH allows for the determination of pH effects *in vivo* using baseline scans before irradiation of tumors. Tumor bearing mice can be treated with sodium bicarbonate to alkalinize the tumor microenvironment and determine if a change in pH affects how CONPs affect radiation damage to tumors.

5

# 2. Chapter 2: Background and Significance

## *2.1.    Significance and Scope of Project*

Over one and a half million people are expected to be diagnosed with cancer in 2016, with almost six hundred thousand expected to die.[2] While these are staggering numbers, the contributions of early detection and advances in therapy have led to more than 14 million cancer survivors currently in the United States and a 5 year survival rate that has increased by 20% in the last 30 years.

The three main treatment options for cancer include surgical resection, radiation therapy, and chemotherapy, but may also include hormone therapy, immune therapy, or targeted therapies that specifically interfere with cancer growth. The appropriate therapy is determined by tumor type and stage, which includes the extent of the primary tumor (T), spread to and number of involved lymph nodes (N), and the presence or absence of metastasis (M).  If metastasis is detected, resection of the tumor is less likely to be possible as a curative option, and radiation therapy and chemotherapy become the most viable options for curative therapy. Despite advances in drug targeting and conformal radiation therapy, these treatments can have serious side effects due to their non-specific damage which causes destruction of normal tissues. These side effects can drastically decrease the quality of life of patients undergoing therapy. It is therefore an important area of research in discovering treatments that may prevent the collateral normal tissue damage of these therapies. Such a treatment would lead to an enhanced therapeutic index of radiation

6

therapy and chemotherapy and improve quality of life and possibly increase survival for cancer patients.

Nanomedicine is a field that studies the application of nanoscale compounds for medical application in areas such as targeted drug therapy, implantable materials, biosensors, and molecular imaging. There are currently over 200 nanomedicine products that are approved for clinical use or in clinical trials.[3] The most common type of nanomedicine is nanoparticles, which have unique physiochemical and biological properties for many biomedical applications, including cancer. One such nanoparticle is the cerium oxide nanoparticle (CONP). Research on CONPs has demonstrated their radioprotective qualities for protection of normal tissue and prevention of side effects during radiation therapy.[4–9] This research has also shown *in vitro* that their protective effect on cancerous tissue is minimal. While the mechanisms of this discrepancy in protection are not yet completely understood, it may have to do with the different microenvironment of tumor tissue compared to normal tissue. Prominent features of the TME include changes to the extracellular matrix, a unique immune cell makeup, abnormal leaky vasculature, increased interstitial pressure, and uneven blood flow.[10,11] These factors contribute to tumor hypoxia and acidic pH, which can affect drug uptake, metabolism, and mechanisms.[12]

Many developments in nanomedicine have also incorporated the use of molecular imaging, using the nanomedicines as imaging agents, such as iron oxide nanoparticles as MRI contrast agents, quantum dots in fluorescence imaging, and incorporation of radionuclides into nanoparticles for SPECT/PET imaging. Molecular imaging is an integral part of diagnosing cancer patients and planning and following response to therapy. Several imaging modalities are commonly used in cancer patients, including MRI, PET, and CT. MRI images can better distinguish soft tissue

7

structures, and can therefore better identify the boundaries of tumors. CT images are commonly used as guides for biopsy and radiation therapy. PET imaging, specifically using [$^{18}$F]FDG, can best identify small tumor metastasis and tumor response to therapy. Research in molecular imaging continues to improve the application of these imaging modalities in cancer, and clinical translation of new imaging modalities, such as photoacoustic imaging, will make possible a promising future of earlier detection and improved therapy for cancer patients.

## *2.2. Radiation Therapy*

Fifty percent of cancer patients currently undergo some form of radiation treatment during the course of their disease. Several types of radiation treatments are available to patients. There are three broad categories of treatment: brachytherapy, systemic radioisotope therapy, and, most commonly, external beam. All of the methods have the same goal, to deliver a high dose of radiation to cancerous tissue with the intent to kill cancerous cells, while best preventing dose to surrounding normal tissue and associated side effects. Despite advances in radiation therapy techniques, significant radiation dose to normal tissues remains unavoidable.

### 2.2.1. Brachytherapy and Systemic Radioisotope Therapy

Brachytherapy utilizes sealed radioactive sources which can be placed in close proximity to tumors. The sources deposit a high dose to tumor while sparing surrounding normal tissue due to rapid falloff of dose. The methods of implantation can be interstitial, placing the source directly inside the target tissue, intracavity, mostly for uterine, cervical, or vaginal cancer, or external applicators for surface treatment. Typical radioactive sources used in brachytherapy, listed in **Table 1**, come in sealed containers to prevent leakage of activity. The sources can used for permanent interstitial placement or for low dose rate (LDR) or high dose rate (HDR) temporary

8

placement. Permanent placement involves isotopes with a short half-life and is used for slow

growing tumors, such as prostate, due to the slow dose deposition, which is less effective in

rapidly growing tumors.[13] Iodine-125 is the most common permanently placed source, but Gold-

| Radionuclide | Half Life | Photon Energy (MeV) | Half-Value Layer (mm Lead) | Exposure Rate Constant $(\Gamma_\delta)$[a] | Clinical Application |
|---|---|---|---|---|---|
| *Sealed Sources* | | | | | |
| **Cesium-137** | 30 yr | 0.662 | 5.5 | 3.26 | LDR intracavitary |
| **Cobalt-60** | 5.26 yr | 1.17, 1.33 | 11.0 | 13.07 | HDR intracavitary |
| **Iodine-125** | 60.2 d | 0.028 avg | 0.025 | 1.46 | Permanent interstitial |
| **Iridium-192** | 74.2 d | 0.38 avg | 2.5 | 4.69 | LDR temporary interstitial; intracavitary; HDR interstitial and intracavitary |
| **Gold-198** | 2.7 d | 0.412 | 2.5 | 2.38 | Permanent interstitial |
| **Palladium-103** | 17 d | 0.021 avg | 0.008 | 1.48 | Permanent interstitial |
| **Radium-226** | 1600 yr | 0.83 avg | 12.0 | 8.25[b] | LDR intracavitary and interstitial |
| *Unsealed Sources* | | | | | |
| **Iodine-131** | 8.06 d | 0.61 ($\beta_{max}$) 0.364 ($\gamma$) | - | - | Thyroid cancer |
| **Phosphorous-32** | 14.3 d | 1.71 ($\beta_{max}$) | - | - | Ovarian cancer seeding; peritoneal surface; chronic leukemia |
| **Radium-223** | 11.4 d | 5.78 ($\alpha_{avg}$) | - | - | Diffuse bone metastases |
| **Samarium-153** | 46.3 h | 0.81 ($\beta_{max}$) 0.103 ($\gamma$) | - | - | Diffuse bone metastases |
| **Strontium-89** | 51 d | 1.4 ($\beta_{max}$) | - | - | Diffuse bone metastases |

**Table 1:** Characteristics of radionuclides used in brachytherapy and their clinical applications. Lower energy isotopes with short half-lives, such as ^{125}I, [198]Au, and [103]Pd are used for permanent implantation, while higher energy and longer half-life isotopes, including ^{137}Cs, ^{60}Co, ^{192}Ir, and [226]Rd are used for LDR and HDR temporary interstitial and intracavitary placement. Unsealed sources can be given orally (^{131}I), intraperitoneally (^{32}P), or intravenously ([223]Rd, [153]Sa, or [89]St).
[a]Unfiltered, units $Rcm^2/mCi\text{-}h$
[b]Filtered by 0.5mm Pt, units $Rcm^2/mg\text{-}h$

198 or Palladium-103 may also be used. LDR sources, defined as rates between 0.4 and 0.8 Gy/hr, and HDR, rates greater than 12 Gy/h, are used in both intracavitary and interstitial placement. The most common intracavitary placement is uterine/cervical, usually with a tandem and ovoid device, seen in **Figure 2**, with isotopes such as Cesium-137 (LDR) or Iridium-192 (HDR).[14] Interstitial brachytherapy usually requires surgical placement of sources with needles or catheterization for afterloading the sources. Radium-226 was the most commonly used source, but has since been replaced because of concerns of leaking. Iridium-192 is now commonly used, which has a small source size and low photon energy for easier shielding. If catheters are placed in the patient, a computer controlled afterloader can be used to automatically place and remove radioactive seeds in the patient therefore minimizing dose to personnel.
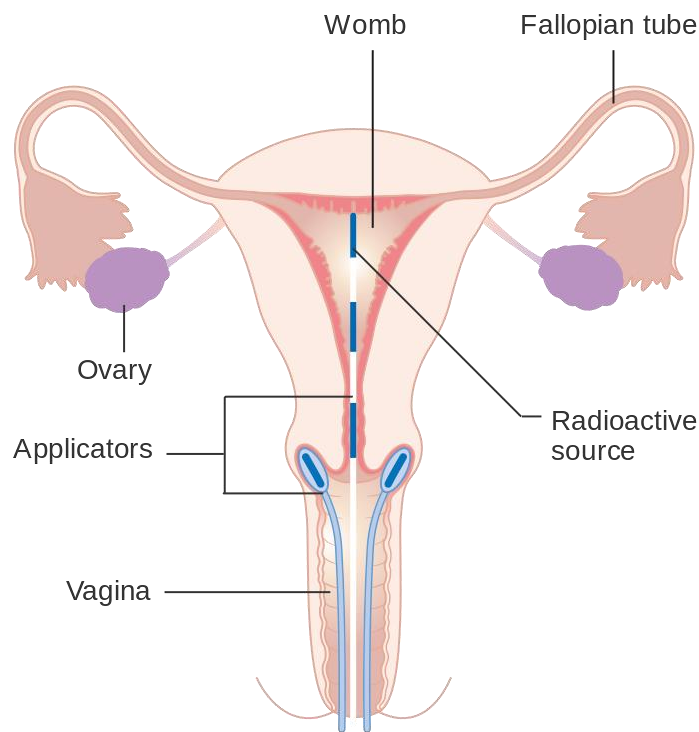


**Figure 2:** Example of tandem and ovoid device implanted in a patient's vagina/uterus for brachytherapy of uterine or cervical cancer. The tandem (protruding tube in center), containing radioactive brachytherapy seeds, provides a dose to the uterus and the ovoids (oval shapes at base of tandem), which also contain radioactive seeds, give dose to the cervix. © Cancer Research UK / Wikimedia Commons / CC BY-SA 4.0.[15]

Systemic radiation therapy is used by intravenous, intraperitoneal, or oral administration of radioactivity, with a few example agents in **Table 1**. The agents must be taken up with high specificity by the target organ to prevent damage to systemic tissues. One example is Iodine-131, which is administered orally as NaI and localizes almost exclusively to the thyroid to treat thyroid cancer. Phosphrous-32 can be used as an intraperitoneal injection as a chromic phosphate colloid to deliver dose to the peritoneal surface. This therapy is used in conjunction with brachytherapy for uterine cancer.[16] Samarium-153 and Strontium-89 can be used to palliatively treat diffuse bone metastases as these isotopes are taken up preferentially by bone, samarium when chelated to ethylenediamine tetra(methylene phosphonic acid) (EDTMP) and strontium as a substitute for calcium.[17] Similarly, radium-223 is used to treat bone metastases with curative intent and, as an alpha emitter, has high dose deposition at low range (<100 μm), decreasing dose to surrounding tissues.[18]

### 2.2.2. External Beam Radiation

External beam radiation therapy is the most common type of radiation therapy. It can use photons, electrons, protons, neutrons, or heavier ions as the energetic source of radiation. During radiation therapy, patients are stationary and the source of radiation is pointed at the location of the tumor. Radiation will deposit in tissue in a non-linear fashion that is dependent on radiation type and energy, as seen in **Figure 3**. High energy electrons are deposited mostly near the surface, with poor depth of penetration, and are only useful for superficial tumors less than 5cm deep. High energy protons lose energy as they pass through matter at a rate which is inversely proportional to their velocity, so as they slow down they deposit more energy, leading to what is called a Bragg peak. Proton therapy utilizes this peak to create higher dose deposition to tumors compared to surrounding tissue, but cost and few available facilities makes it less feasible as a

11

common treatment. High energy photon therapy in the tens of MeV have a peak in dose deposition a few centimeters deep, which can be a benefit for skin sparing, that then tapers as depth increases, allowing for dose deposition deeper in tissue. This type of radiation is the most common form of external radiation therapy with applications for almost all tumor types.

The dose distribution profile of photon radiation therapy can be manipulated in several ways, including beam flattening, wedges, shielding, and intensity modulation. Beam flattening ensures that the same dose is deposited across the radiation field by making the beam intensity uniform across the field. Similarly, wedges can prevent increases in dose deposition when using more than one beam angle by partially blocking the radiation for overlap areas that would otherwise get an increased dose. Shielding is most commonly used in the form of multileaf collimators
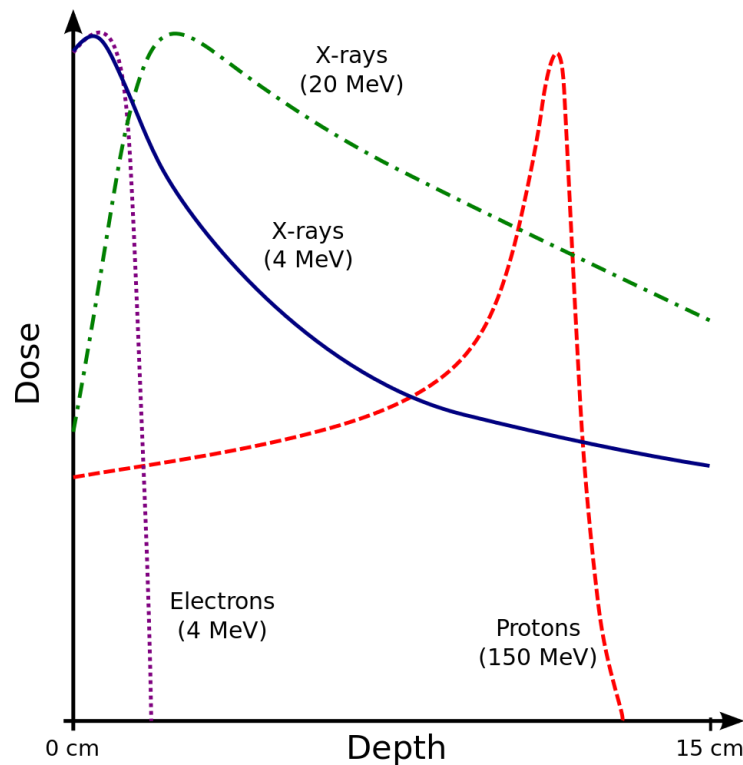


**Figure 3:** Depth dose distribution for 4 MeV electrons (purple/dotted), 4 MeV X-rays (blue/solid), 20 MeV X-rays (green/dash-dot), and 150 MeV protons (red/dashed). The deposition of dose depends on both the energy and type of radiation, with electrons showing deposition only at the surface, X-rays (photons) with excellent depth of penetration and surface sparing at high energies, and protons with gradual deposition until a high deposition at the Bragg peak. © Username: Cepheiden / Wikimedia Commons / CC BY-SA 3.0 / GFDL.[19]

(MLCs), "leaves" of highly attenuating material that can move independently to create dynamic patterns that collimate the beam to conform to the contours of the tumor, as seen in **Figure 4**. Intensity modulated radiation therapy (IMRT) utilizes MLCs and computer assisted treatment planning to optimize dose to tumor with minimal dose to surrounding at risk tissues. This involves using several different configurations or dynamic movement of the MLCs at several beam locations. The result of these dose distribution manipulations is a dose distribution that is
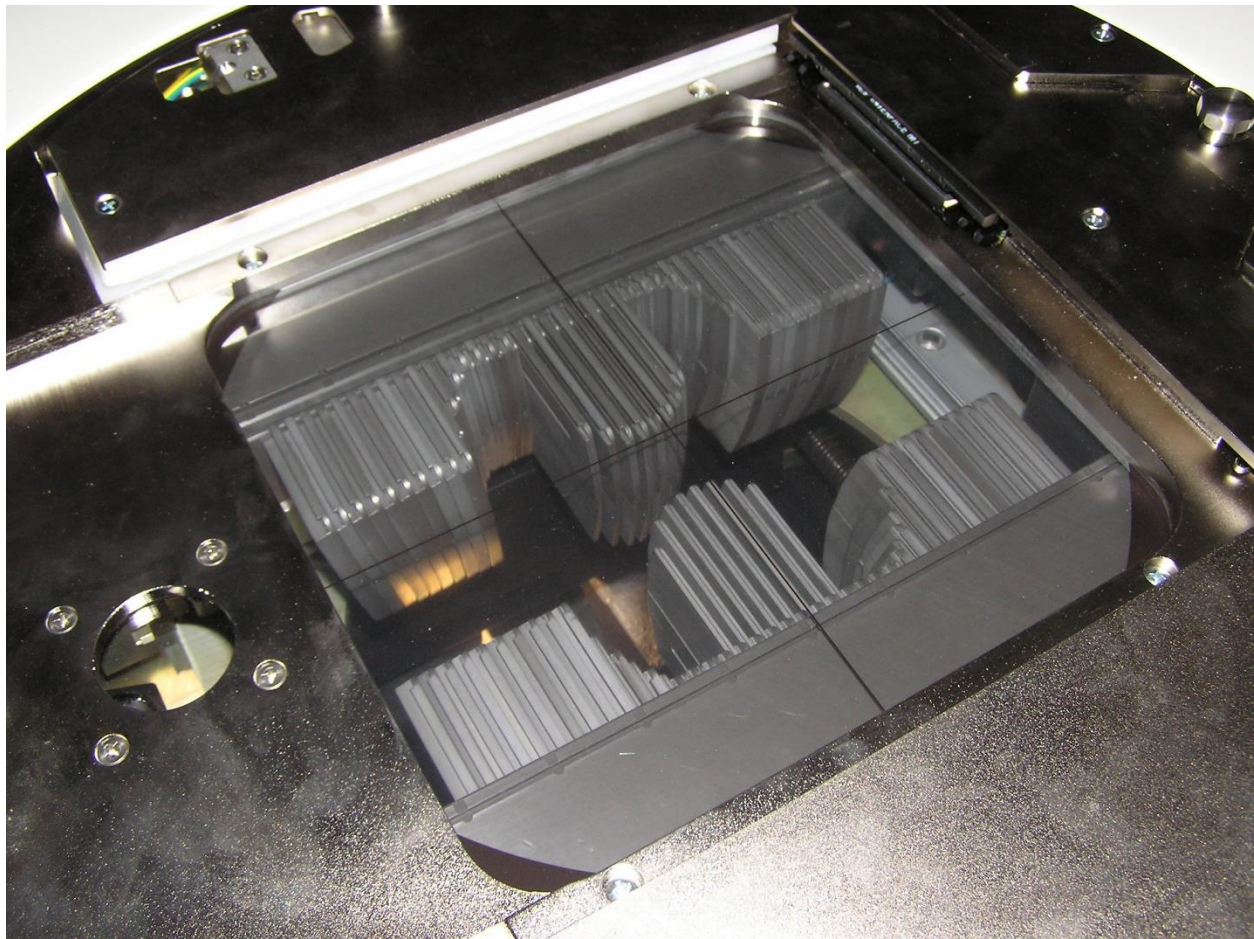


**Figure 4:** Multileaf collimator, which, when attached to a beam accelerator, can block and contour the beam. Each "leaf" can be programed to move independently to create a collimated window. Single windows can be used per beam in conformal radiation therapy (CRT), or have different windows stacked at the same beam position or make the leaves move dynamically while the beam is on in intensity modulated radiation therapy (IMRT). © Username: Egg / Wikimedia Commons / CC BY-SA 2.5.[20]

13

highly concentrated in the tumor with the minimal dose possible to surrounding normal tissue, as seen in comparison of 3-D conformal radiation therapy (3D-CRT) to IMRT in **Figure 5**.[21] While reduction dose deposition to normal tissue has continued to improve, radiation damage to normal tissues surrounding tumors continues to be an issue.
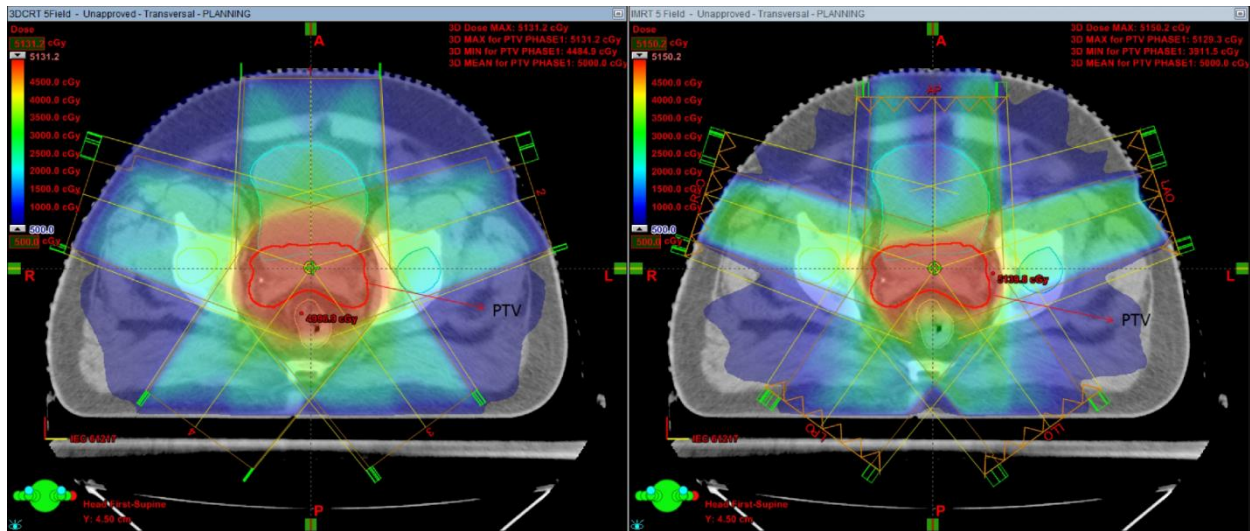


**Figure 5:** A comparison of 3D conformal radiation therapy (3D-CRT), left, and intensity modulated radiation therapy (IMRT), right. While both techniques use the same beam positions, the modification of the beams by multileaf collimators in IMRT allows for a radiation dose that conforms to the shape of the tumor and better spares surrounding structures from radiation damage. © International Journal of Cancer Therapy and Oncology (IJCTO) / CC BY-SA 3.0.[21]

### 2.2.3. Radiobiology and Radiation Side Effects

The effects of radiation that lead to tissue damage occur at the subcellular level. The most significant factor in radiation induced cellular damage is how the radiation affects DNA. There are two mechanisms by which radiation can damage DNA, direct and indirect. Radiation can directly damage DNA through breaking of the DNA backbone leading to single strand breaks, or more damaging double strand breaks. Radiation can also cause the ionization of molecules in the cell and produce free radicals, including hydrogen peroxide ($H_2O_2$) and superoxide ($O_2^{\cdot-}$). These free radicals can then go on to damage DNA base pairs. When DNA damage occurs and passes the threshold where the cell cannot repair the damage, the cell signals to undergo apoptosis or

mitotic catastrophe and the cell dies.[22] If enough cells undergo apoptosis, the tissue or organ

which they make up may have reduced function, leading to significant side effects.

Damage to normal tissues is the limiting factor for radiation therapy with proportionally

escalating dose to surrounding tissue as the dose is increased to tumor. The measurement of this

factor is called the therapeutic ratio or therapeutic index, the amount of expected tumor control to

expected side effects, as illustrated in the dose response relationship in **Figure 6**.[23] The higher

the therapeutic index, the more likely treatment can be effective without significant side effects.

Radiation damage to tissue can cause side effects that present early or late. Acute side effects are

most common in radiosensitive organs. These are organs that have cells that are constantly

multiplying with stem cells replenishing tissue, such as in skin, the gastrointestinal tract, and

bone marrow. These organs show acute side effects that show up days to weeks after irradiation.

Skin irradiation causes reddening of the skin and hair loss. Gastrointestinal effects from radiation

include xerostomia (dry mouth), nausea and vomiting, and diarrhea. Irradiation of large sections

of bone marrow can cause pancytopenia and subsequent risk of infection. While these tissue are
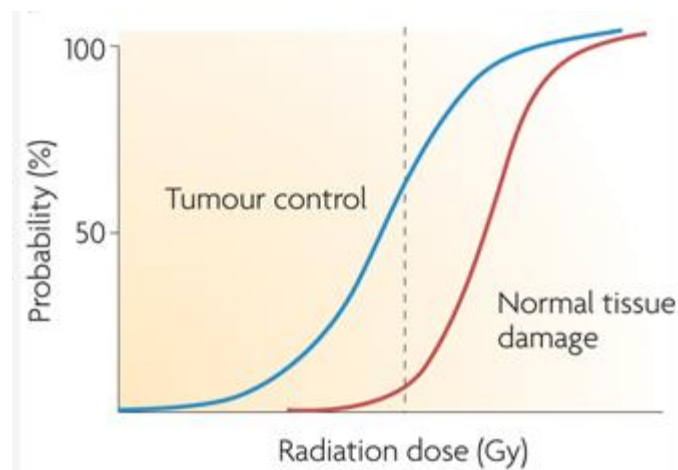


**Figure 6:** Dose-response relationship demonstrating that an increase in probability of tumor control also leads to in increased likelihood of complications from normal tissue damage. The dashed line represent the ideal point at which tumor control is likely (>50%), but normal tissue damage is unlikely (<5%). The ratio of these values is the therapeutic ratio or therapeutic index. Reprinted by permission from Macmillan Publishers Ltd: Nature Reviews Cancer, **Ref. 23**, copyright 2009.

15

some of the most radiosensitive, all organs can be damages by radiation, and can present late effects. Some of the most important organs to protect due to more consequential side effects include the heart, liver, and lungs. Late effects in these tissues include hepatitis in the liver, pneumonitis and pulmonary fibrosis in the lungs, and fibrosis and cardiomyopathy in the heart. Currently, the most common method to prevent the acute and late side effects from radiation damage to normal tissues is using IMRT to avoid irradiating the tissue and decreasing the total dose prescribed. There is currently only one drug approved for radiation protection, with many more currently being researched.

### 2.2.4. Radioprotective Drugs

Research into radioprotective drugs began in 1948 with the discovery that high doses of cysteine, a semi-essential amino acid with a sulfhydryl group, could protect mice if administered before whole body irradiation. After administration of the drug at about 150mg/kg, mice required 1.8 times the radiation dose to produce the same mortality rate. The military implications of radiation protection from atomic bomb fallout led to a program at Walter Reed Institute of Research to develop similar drugs with less toxicity. Over 4000 compounds were tested, most sharing the sulfhydryl group. It was found that the sulfhydryl group conferred radioprotection by acting as a radical scavenger and assisted in DNA damage repair, but total mechanistic understanding was not complete. Newer compounds decreased toxicity by covering the sulfhydryl group with a phosphate group. Two compounds that came into common use from those studied were WR-638 (cystaphos) and WR-2721 (amifostine).[24] Other drugs capable of reducing RT side effects have also been developed, such as thiols and nitroxides. However, their own side effects can be self-limiting and their use is controversial as they lack mechanistic data demonstrating if and how they completely prevent tumor radio-protection.[25,26]

16

### 2.2.4.1. Amifostine

Amifostine is the only radioprotective drug approved by the U.S. Food and Drug Administration (FDA) for use in radiation therapy. In a phase III clinical trial, it was shown to decrease xerostomia (dry mouth) in patients undergoing radiation therapy for head and neck cancer, while preserving antitumor treatment efficacy.[27] The main drawback of amifostine is the high dose required, about 400mg/kg, which led to significant side effects in these patients, with over 50% having an incidence of nausea or vomiting and also having risks for hypocalcemia and hypotension.[28] Current use of the drug is still limited to head and neck cancer and concerns of protection of tumor and loss of therapeutic efficacy, combined with its own side effect profile, prevents its universal adoption in radiation therapy.

### 2.2.4.2. Characteristics of an Ideal Radioprotective Drug

As outlined in the introduction, an ideal radioprotective drug can be defined by four characteristics.

1) *Favorable biodistribution/pharmacokinetics*

    To prevent any excess toxicity, the drug must accumulate in normal tissue and have its effect at low dose. It should not have tumor uptake that exceeds normal tissue uptake to prevent any radioprotective effects on cancerous tissue. To prevent any long term effects, it should clear from the body. Ideally the drug would be administered orally, which is the simplest method of administration, but other options include intraperitoneal, intramuscular, or intravenous administration.

2) *Low toxicity*

    The drug should not have a side effect profile that may decrease the quality of life as much as the expected side effects from radiation therapy. Some side effects can be

17

tolerable if they are outweighed by the expected decrease in side effects from radiation therapy.

3) *Minimal protection of cancerous tissue*

The treatment should have minimal effect on the dose response for tumor, having little effect on the curve for tumor control seen in **Figure 6**, and preventing the need for significant dose escalation. If the drug protects cancerous tissue as much as it does normal tissue, the dose of radiation would need to be increased to have the intended cancer killing effects, which would also likely negate the radioprotective effects in normal tissue. The effects on cancer tissue should be predictable to allow for consistent adjustment of treatment planning to retain the efficacy of radiation therapy. It would also be desirable for the agent to have a synergistic anti-tumor effect to potentially compensate for any protection in the tumor.

4) *Protection of normal tissue*

The drug should prevent damage to normal tissue from radiation damage enough that expected side effects are reduced or prevented entirely. The dose response curve for normal tissue, seen in **Figure 6**, should shift significantly to the right, thereby increasing the expected therapeutic index and allowing a higher dose for a better chance at tumor control.

These would be the most important qualities for an ideal radioprotective drug, while more pharmacodynamics information on dose response and mechanisms of action would further support translation of the drug to the clinic.

18

## *2.3.* *Nanomedicine*

Nanotechnology applications in medicine is an exciting field that has only existed for a few decades. Clinical application of nanotechnology did not start until 1995 with FDA approval of Doxil, a nanosize liposomal formulation of doxorubicin that enabled targeted delivery of the chemotherapeutic drug with less toxicity.[29] Though nanomedicine presents the possibility of great leaps in medical therapy, it comes with many drawbacks including cost of development and difficult standards for safety and efficacy due to the complex nature of many nanotherapies compared to traditional molecular drugs. However, the potential benefits greatly outweigh the drawbacks and nanomedicine continues to be at the forefront of research. Applications of nanomedicine extend to almost all medical fields and include diagnostics, pharmaceuticals, regenerative medicine, implants, nanosurgery, and nanorobotics.[30–33]

### 2.3.1. Nanoparticles

Nanoparticles (NPs) have combined unique physicochemical and biological properties for many biomedical applications.[34–38] NPs are made of various materials, including those made from bio-organic chemicals (e.g., phospholipids, lipids, dextran and chitosan), carbon-based materials (e.g. carbon nanotubes) and inorganic NPs (e.g. those based on metals, metal oxides and metal sulfides), also including semiconductor NPs (e.g. quantum dots).[34,35,39–46] The design of NPs, in terms of shape, size, surface charge, and material composition, will their physicochemical properties, which in turn drives their *in vivo* biochemical interactions at the cellular and organ levels. The unique ability to change these properties allows the control of NPs' pharmacokinetic properties, imaging properties, and toxicity.[39,40,47–53] Compared to conventional drugs, this multi-functionality offers a novel approach to cancer therapy, giving them combined applications in such areas as drug delivery, diagnostic imaging, and image-guided surgery.

19

### 2.3.1.1.  Intrinsic Radiolabeling of Nanoparticles

Deriving direct *in vivo* data on the behavior of NPs is essential to understanding overall pharmacokinetics of various NP-chemical constructs. Incorporating an imaging signal in the NP-construct enables *in vivo* imaging using various modalities, such as fluorescence and positron emission tomography (PET). This can be accomplished either by covalently binding an imaging molecule to the NP surface or by incorporating the imaging molecule into the NP core (intrinsic labeling), as seen previously in **Figure 1**.[52,54,55] Metal-based NPs are particularly attractive for the latter approach as many elemental metals allow inherent radio-isotopic or fluorescent detection. The Center for Molecular Imaging at Virginia Commonwealth University has demonstrated the intrinsic labeling approach, using various radioisotopes, for three types of NPs: cerium oxide NPs (CONPs) with Cerium-141, Indium-111, and Zinc-65, quantum dots with Indium-111, and superparamagnetic iron oxide NPs (SPIONs) with Iron-59 and Manganese-52.[1,52,56]

## 2.4.  *Cerium Oxide Nanoparticles (CONPs)*

Cerium oxide nanoparticles (CONPs) are unique among metal oxide nanoparticles for the catalytic redox properties of their surface. Though the bulk material of CONPs is in the form $CeO_2$, with cerium in the $Ce^{4+}$ oxidation state, oxygen vacancies on the surface of CONPs lead to both $Ce^{3+}$ and $Ce^{4+}$ oxidation states being present. When reacting with oxidative species, these oxidation states are able to auto-regenerate, as seen in **Figure 7**, allowing for catalyst-like radical scavenging that mimics both superoxide dismutase (SOD) and catalase.**[8,43,57–60]** These properties have been extensively studied and have led to applications in industry and numerous pre-clinical medical studies. Industrial applications include fuel cells, ultraviolet absorbance, oxygen sensing, and automotive catalytic convertors.[61–64]

Oxidative stress is ubiquitous as a common aspect in many clinical pathologies, and therefore CONPs also have a broad potential for therapeutic applications. Within the last 15 years, CONPs have been developed and studied for protection of tissues from oxidative and inflammatory damage, which has been demonstrated in neuronal, ocular, and heart tissue.[65–69] CONPs have also demonstrated radioprotection of normal tissues, as seen in **Figure 8**, and lack of protection of cancer cells *in vitro*, seen in **Figure 9**.[4–9] Compared to conventional drugs, CONPs are a unique radioprotective drug candidate with documented low toxicity.[70] Other studies have shown that redox-active CONPs exhibit cytotoxic and anti-invasive effects on several cancer cells and are capable of sensitizing tumor cells to radiation, while protecting normal cells in the tumor stroma.[34,71,72] At pH 4.0 CONPs not only lose their ability to cycle back to the $Ce^{4+}$ state, a property that remains even after return to neutral pH, but also show significant oxidative capabilities that could lead to cell damage.[43,73] Tumor microenvironments provide a medium of low pH that could selectivity reduce the radioprotective abilities of CONPs in tumor tissue.

$$Ce_2O_3 + 2[OH\cdot] \longrightarrow 2CeO_2 + H_2O$$

$$Ce^{3+} \qquad \textbf{Oxidation - reduction cycle} \qquad Ce^{4+}$$

$$Ce_2O_3 + O_2 + 2H^+ \longleftarrow 2CeO_2 + H_2O$$
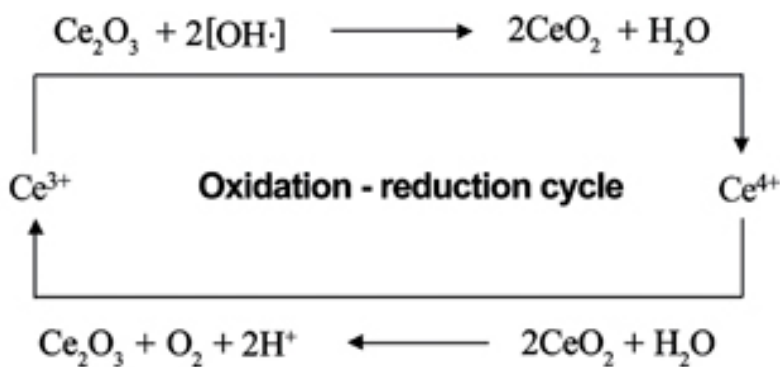
**Figure 7:** Auto-regenerative properties of cerium oxide nanoparticles. In this proposed mechanism of CONPs' reaction with hydroxyl radical [OH•], $Ce^{3+}$ is converted to $Ce^{4+}$, which then catalytically converts back to $Ce^{3+}$. Reprinted by permission from John Wiley & Sons Inc.: Small, **Ref. 43**, copyright 2008.

**Figure 8:** CONPs improve toxicity after head and neck radiation. Radiation-induced dermatitis is reduced in mice exposed to 30 Gray in 6 fractions to the head and neck region. Mice were given 15 nM or 15 μM uncoated CONPs and showed quicker resolution of radiation dermatitis at 12 weeks in comparison to the control group that was only irradiated. Reprinted by permission from Elsevier: Nanomedicine: Nanotechnology, Biology and Medicine, **Ref. 6**, copyright 2012.
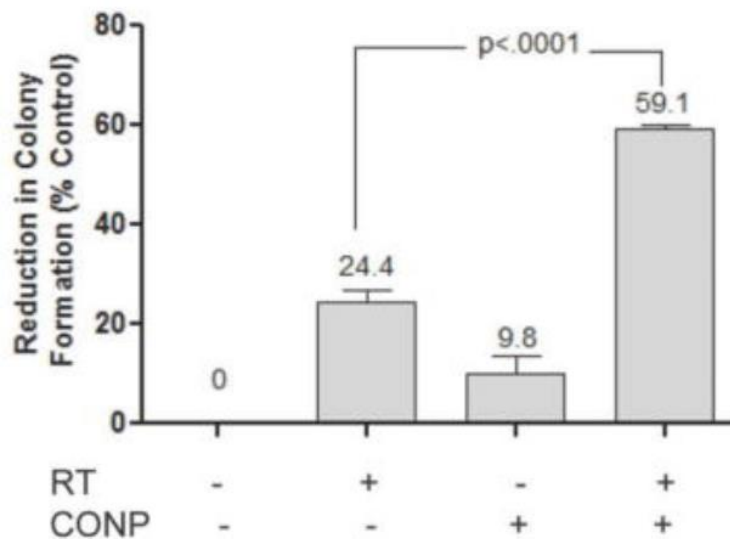


**Figure 9:** L3.6pl (pancreatic tumor) cells pre-treated with 10 μM CONPs for 24 hours followed by RT at 5 Gy show a greater reduction in colony formation compared to radiation alone, indicating a possible radiosensitizing effect. . Reprinted by permission from Elsevier: Nanomedicine: Nanotechnology, Biology and Medicine, **Ref. 9**, copyright 2013.

## 2.5.     *The Tumor Microenvironment*

While many mutations in tumor cells may affect their uptake of drugs, the tumor

microenvironment (TME), with similar characteristics across many cancer types, also presents a

major hurdle for drug delivery to and therapy of cancer.[12] An overview of the TME is seen in

**Figure 10**.[74] A prominent feature of the TME is the abnormal leaky vasculature, allowing

passage of large molecules and causing increased interstitial pressure, and the uneven blood flow

leads to hypoxia and low pH.[12,75,76] The immune cell makeup of the tumors is also drastically

different, with cell type changes that prevent immune destruction of the tumor.[10] The

extracellular matrix also changes composition.[11] All of these factors affect how drugs are

delivered to, taken up by, and chemically interact with the tumor cells, making cancer therapy

very unpredictable without precise understanding of the effects of the TME.
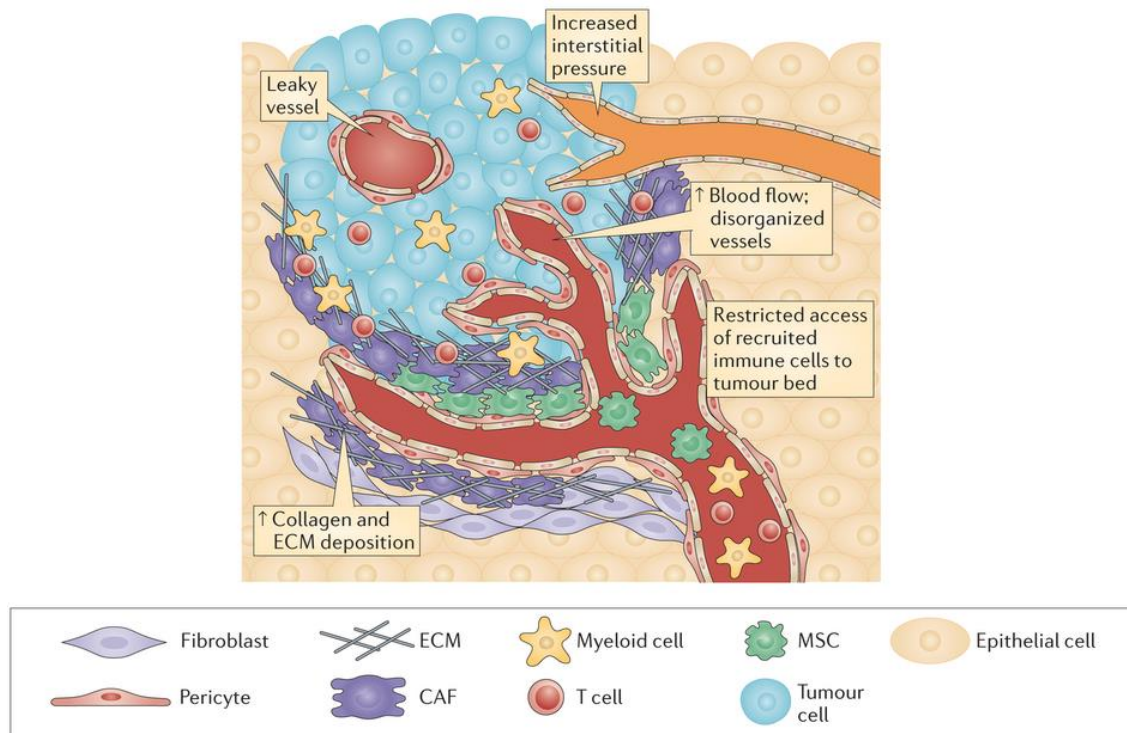


**Figure 10:** Overview of the tumor microenvironment (TME) and associated cells compared to normal tissue. Prominent features of the TME include recruitment of mesenchymal stem cells (MSCs), activation of cancer-associated fibroblasts (CAFs), immune cell infiltration, leaky vasculature, increased interstitial pressure, abnormal extracellular matrix (ECM), and areas of necrosis, hypoxia, and low pH. . Reprinted by permission from Macmillan Publishers Ltd: Nature Reviews Immunology, **Ref. 74**, copyright 2015.

23

### 2.5.1. pH and Hypoxia of the Tumor Microenvironment

The pH of the tumor microenvironment is lower than normal tissue pH 7.4, with an average of 7.0 with wide variance.[77]. Hypoxic regions are common to almost all solid tumors due to the abnormal vasculature, with $[O_2]$ below 2%, compared to 7-10% in normal tissues, giving rise to tumor radio-resistance.[78] Drug therapies to normalize the pH and vasculature of the TME have been studied, but the effects of altering the microenvironment are still not completely understood.[79,80]

## 2.6.    Molecular Imaging

Molecular imaging modalities allow unique methods to non-invasively observe morphology or biological processes *in vivo*. Modalities include positron emission tomography (PET), single photon emission computed tomography (SPECT), optical fluorescence imaging, magnetic resonance imaging (MRI), x-ray computed tomography (CT), ultrasound, and photoacoustic imaging. Development of these imaging modalities has gone from focus on anatomical information, to more detailed functional and molecular information, as outlined in **Figure 11**. Each have their own advantages and disadvantages, as outlined in the two parts of **Table 2**. This project utilized four modalities of molecular imaging: PET, CT, MRI, and fluorescence.
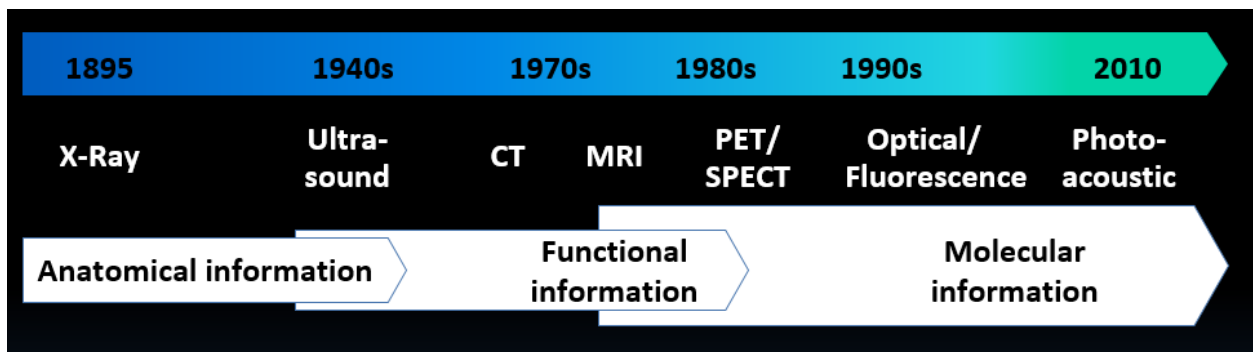


**Figure 11:** Development of biomedical imaging has progressed from a focus on anatomical information, to more revealing and clinically relevant functional and molecular information.

| Imaging technique | Detected signal for image generation | Spatial resolution | Depth | Temporal resolution | Sensitivity | Quantitative degree |
|---|---|---|---|---|---|---|
| Positron emission tomography (PET) | high-energy γ rays | 1-2 mm | no limit | 10 sec to minutes | $10^{-11}$–$10^{-12}$ mole/L | +++ |
| Single photon emission computed tomography (SPECT) | lower-energy γ rays | 1-2 mm | no limit | minutes | $10^{-10}$–$10^{-11}$ mole/L | ++ |
| Optical fluorescence imaging | visible light or near-infrared | 2-3 mm | <1 cm | seconds to minutes | not well characterized, likely $10^{-9}$–$10^{-12}$ mole/L | + to ++ |
| Magnetic resonance imaging (MRI) | radiowaves | 25-100 μm | no limit | minutes to hours | $10^{-3}$–$10^{-5}$ mole/L | ++ |
| Computed tomography (CT) | X-rays | 50-200 μm | no limit | minutes | not well characterized | ++ |
| Ultrasound | high-frequency sound | 50-500 μm | several centimeters | seconds to minutes | not well characterized | + |
| Photoacoustic | high-frequency sound (laser excitation) | 50-500 μm | several centimeters | seconds to minutes | not well characterized, likely $10^{-9}$–$10^{-12}$ mole/L | ++ |

**Table 2:** Characteristics of medical imaging modalities that have molecularly targeted imaging agents or non-targeted agents. Adapted from © Genes and Development / CC BY-NC 4.0.[81]

| Imaging technique | Principal Use | Advantages | Disadvantages | Clinical Application | Cost |
|---|---|---|---|---|---|
| Positron emission tomography (PET) | metabolic, reporter/gene expression, receptor/ligand, enzyme targeting | high sensitivity, isotopes can substitute naturally occurring atoms, highly quantitative | PET cyclotron or generator needed, relatively low spatial resolution, radiation to subject, low specificity of tracers (FDG) | Yes | $$$$ |
| Single photon emission computed tomography (SPECT) | reporter/gene expression, receptor/ligand | many molecular probes available, can image multiple probes at same time, may be adapted to clinical imaging systems | relatively low spatial resolution because of sensitivity, collimation, radiation | Yes | $$$ |
| Optical fluorescence imaging | reporter/gene expression, cell trafficking | high sensitivity, quick, easy, low cost | relatively low spatial resolution, surface-weighted | Yes, but limited (surgical) | $–$$ |
| Magnetic resonance imaging (MRI) | morphological reporter/gene expression, receptor/ligand if many receptors | highest spatial resolution, combines morphological and functional imaging | relatively low sensitivity, long scan and post processing time, mass quantity of probe may be needed | Yes | $$$$ |
| Computed tomography (CT) | morphological | bone and tumor imaging, anatomical imaging | limited "molecular" applications, limited soft tissue resolution, radiation | Yes | $$ |
| Ultrasound | Morphological, blood flow | real-time, low cost | limited spatial resolution, mostly morphological | Yes | $$ |
| Photoacoustic | melanoma and lymph node metastases | spectral information and optical contrast characteristics, high resolution, deeper into body than fluorescence imaging | shielding by strongly absorbing objects newer technology with few current probes | Yes, but limited (skin and shallow depth examination) | $$-$$$ |

**Table 2 (continued):** Characteristics of medical imaging modalities that have molecularly targeted imaging agents or non-targeted agents. Adapted from © Genes and Development / CC BY-NC 4.0.[81]

## 2.6.1. Positron Emission Tomography (PET) Imaging

PET imaging is based on radioactive isotopes that can emit a positron during decay. Some samples of isotopes used for PET imaging are found in **Table 3**. This positron is almost immediately annihilated upon production when it comes in contact with an electron. The annihilation produces two photons of 511 keV that are emitted along the line of response (LOR) with nearly 180° separation, as seen in **Figure 12**.[82,83] Once detected by photomultiplier tubes surrounding the patient, a computer can calculate the origin of the photons by coincidence detection and reconstruct into a three dimensional image. The intrinsic limitation of resolution for PET imaging comes both from the distance the positron travels before it is annihilated, and the slight deviation from 180° for the dual-photon release. For the positron, the mean free path before annihilation is proportional to the maximum positron energy, so isotopes that produce less energetic positrons will have better inherent resolution. Due to residual momentum of the

| Nuclide | Half-life | Decay Modes | Maximum positron energy (MeV) and yield (%) | Production |
|---------|-----------|-------------|---------------------------------------------|------------|
| $^{11}C$ | 20.4 mins | EC, $\beta^+$ | 0.961 (99.8%) | $^{14}N(p,\alpha)^{11}C$ |
| $^{13}N$ | 9.96 mins | EC, $\beta^+$ | 1.2 (99.8%) | $^{16}O(p,\alpha)^{13}N$ |
| $^{15}O$ | 2.04 mins | EC, $\beta^+$ | 1.73 (99.9%) | $^{15}N(p,n)^{15}O$ $^{14}N(d,n)^{15}O$ |
| $^{18}F$ | 109.8 mins | EC, $\beta^+$ | 0.634 (96.7%) | $^{18}O(p,n)^{18}F$ $^{20}Ne(d,\alpha)^{18}F$ |
| $^{52}Mn$ | 5.6 days | EC, $\beta^+$ | 0.575 (29.6%) | $^{52}Cr(p,n)^{52}Mn$ |
| $^{52}Fe$ | 8.275 hrs | EC, $\beta^+$ | 0.804 (55.5%) | $^{52}Cr(^3He,2n)^{52}Fe$ $^{52}Cr(\alpha,3n)^{52}Fe$ $^{55}Mn(p,4n)^{52}Fe$ |
| $^{89}Zr$ | 3.27 days | EC, $\beta^+$ | 0.90 (22%) | $^{89}Y(d,n)^{89}Zr$ $^{89}Y(d,2n)^{89}Zr$ |
| $^{124}I$ | 4.18 days | EC, $\beta^+$ | 2.138 (23.0%) | $^{126}Te(p,3n)^{124}I$ |

**Table 3:** The characteristics of various PET radionuclides.

27

cannot be corrected for. The mechanical limit to resolution for PET comes from the detector size. The resolution of commercial PET scanners, with wider bore and larger detectors, can be reduced to around 5mm, while pre-clinical PET systems, usually with smaller bore and detectors, can achieve a resolution as low as 1mm. Commonly, PET systems are combined with CT to provide anatomical reference. Applications for PET imaging are focused on metabolic and molecular information, with many compounds used to determine cell specific interactions in the body, as seen in **Figure 13**.[84]
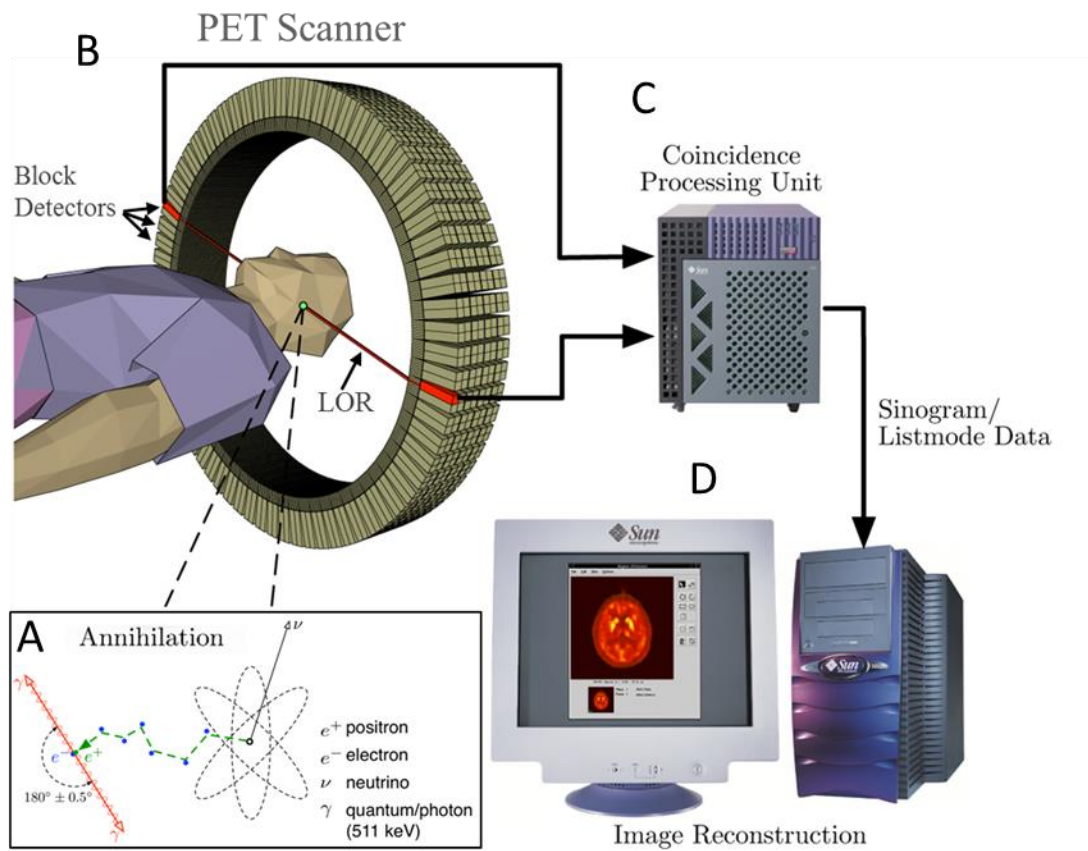


**Figure 12:** PET Scanner Schematic. An imaging agent with a positron emitting isotope is injected into a patient. A) The positron will travel a short distance, proportional to its energy, before annihilating with an electron and emitting two 511 keV photons. These photons, which are emitted at $180 \pm 0.25°$, travel to block detectors of the PET scanner (B) which send data on the line of response (LOR) to a coincidence processing unit (C) and a computer for image reconstruction (D). A) Jens Maus / Wikimedia Commons / Public Domain.[82] B-D) Jens Maus / Wikimedia Commons / Public Domain.[83]

28
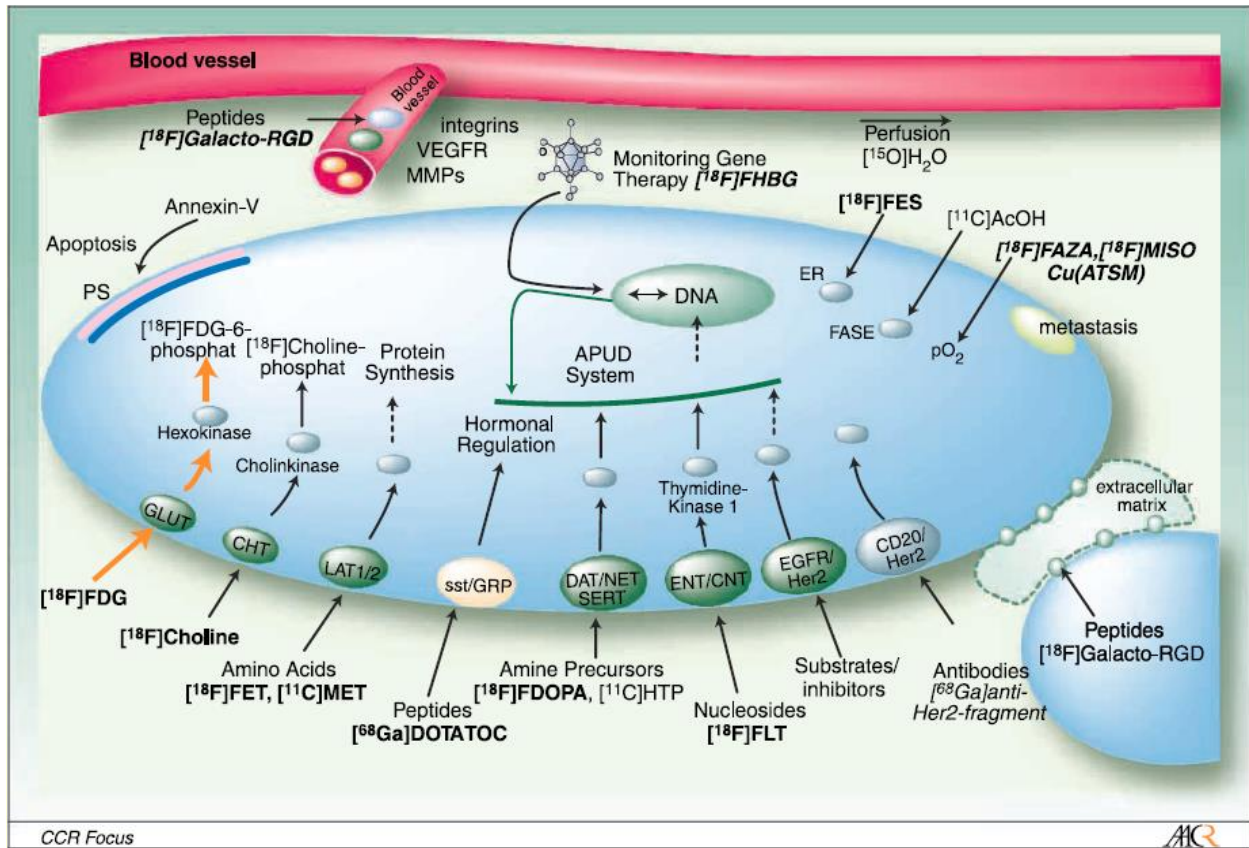
**Figure 13:** Selected targets and corresponding nuclear imaging probes already established for nuclear molecular imaging in the clinic (bold) or currently under assessment in clinical studies (italic). Reprinted from Clinical Cancer Research, **Ref. 84**, copyright 2007, with permission from AACR.

## 2.6.1.1. [$^{18}$F]-fluorodeoxyglucose

While many PET imaging compounds are approved for use in the clinic, the PET imaging agent in most common clinical use is [$^{18}$F]-fluorodeoxyglucose ([$^{18}$F]-FDG). This molecule is structurally similar to glucose, as seen in **Figure 14**, and is taken up by cells by the same
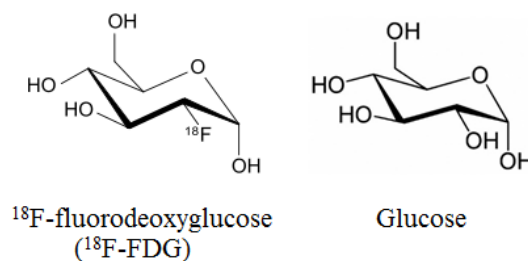


**Figure 14:** Chemical structure of [$^{18}$F]-fluorodeoxyglucose ([$^{18}$F]-FDG), left, compared to glucose, right. Due to the similar chemical structure, the body takes up [$^{18}$F]-FDG as it would glucose. PET imaging after injection of [$^{18}$F]-FDG allows for determination of metabolically active sites, such as tumors.

29

transporters. Once [$^{18}$F]-FDG enters the cell, it is phosphorylated to [$^{18}$F]-FDG-6-phosphate, which cannot leave the cell. Therefore, the radioactivity of $^{18}$F, detected by PET imaging, only represents cells that take up the molecule. Uptake of [$^{18}$F]-FDG mirrors metabolic activity, and is therefore high in organs such as the heart and brain, and is particularly useful for detecting the high metabolic activity of tumors. For [$^{18}$F]-FDG imaging, the patient must fast for several hours before administration of the activity to put the body in a glucose deficient state and increase uptake of [$^{18}$F]-FDG when administered.

Evaluation of [$^{18}$F]-FDG imaging measures the standardized uptake value (SUV) of a region on interest (ROI). This calculates the amount of [$^{18}$F]-FDG taken up in a certain area relative to the expected distribution based on the injected activity and body weight. The equation for SUV is:

$$SUV = \frac{c_{img}}{ID'/BW}$$

where $c_{img}$ is the activity in the ROI, *ID'* is the injected dose, decay corrected to the time of the PET scan, and *BW* is the body weight. By correcting the activity of the injected dose for the decay of $^{18}$F, the whole body will have an average SUV of 1. Areas of high metabolic activity will have higher SUV values than surrounding tissue, with tumors and metastases having an SUV that can range from 2 to 12.[85,86]

### 2.6.1.2. Zirconium-89

Zirconium-89 ($^{89}$Zr) is an isotope that has increased in use in pre-clinical PET imaging studies. The short half-life of $^{89}$Zr, 3.27 days, makes for an ideal candidate for clinical application in the "happy medium" where longer studies can be performed but the patient dose will not be too high. This is especially relevant for antibodies and macromolecules that have a similar biological half-life in the blood. Compared to $^{124}$I, a commonly used PET radiotracer with a similar half-life

30

and positron yield, [89]Zr is superior due to its lower positron energy, allowing for higher

resolution imaging due to the shorter mean path of the positron before it is annihilated.[87]

### 2.6.2. Magnetic Resonance Imaging (MRI)

Magnetic resonance imaging (MRI) has become an important imaging modality in the clinic,

used primarily to examine anatomical structures with excellent soft tissue contrast when

compared to CT. MRI has many clinical applications, including cardiac imaging, neuroimaging,

musculoskeletal imaging, and angiography.[88] The mechanism of MR imaging has to do with the

spin of an atom's nucleus and its reaction to a magnetic field. For clinical MRIs, imaging is

exclusively done with hydrogen nuclei, which are abundantly present in the body in water

molecules. An MRI system is composed of a large magnet with a field strength of 0.2 to 7 Tesla.

The magnetic moment of hydrogen nuclei align themselves with this field when placed in the

bore of an MRI system, such that they spin at an angle, or precess, along this axis at a frequency

proportional to the magnetic field strength, as seen in **Figure15.A and B**.[89] The frequency is

given by the Larmor equation:

$$f_0 = \gamma B_0$$

where $f_0$ is the precessional frequency, $\gamma$ is the gyromagnetic ratio (42.57 MHz T$^{-1}$ for hydrogen

nuclei), and $B_0$ is the magnetic field strength. Higher field strength leads to higher signal to noise

ratio for images, but also results in inhomogeneities in the radiofrequency field and increased

specific absorption rate. When all the hydrogen nuclei are aligned in a field, there is a net

magnetic moment due to the slightly larger ratio of protons in the parallel, lower energy

orientation, than the anti-parallel, higher energy orientation (ratio = 1.000004). This magnetic

moment is on the order of 1 $\mu$T, which cannot be measured in the large magnetic field of the

MRI magnet. However, if this magnetic moment is shifted out of the plane of the MRI magnet's

31

field, it can be measured. To shift the magnetic moment to the transverse plane, an RF pulse at the Larmor frequency is delivered, as seen in **Figure 15.C**. The magnetic moments in the transverse and longitudinal planes are then measured continuously as the nuclei return to equilibrium along the $B_0$ field. The rate at which they return to equilibrium is measured as T1, recovery of longitudinal magnetization, and T2, decay of transverse magnetization, as seen in **Figure 15.D and E**. These two measurements are used to reconstruct images where different tissues show different values for T1 and T2. T1 weighted images show better differentiation for fatty tissues, while T2 weighted images are better for showing water content.

Contrast agents may be used to enhance contrast by affecting T1 and T2 specifically where they are distributed in the body. Agents such as gadolinium and iron oxide nanoparticles are paramagnetic and cause magnetization transfer to local bound hydrogen nuclei, reducing the T1
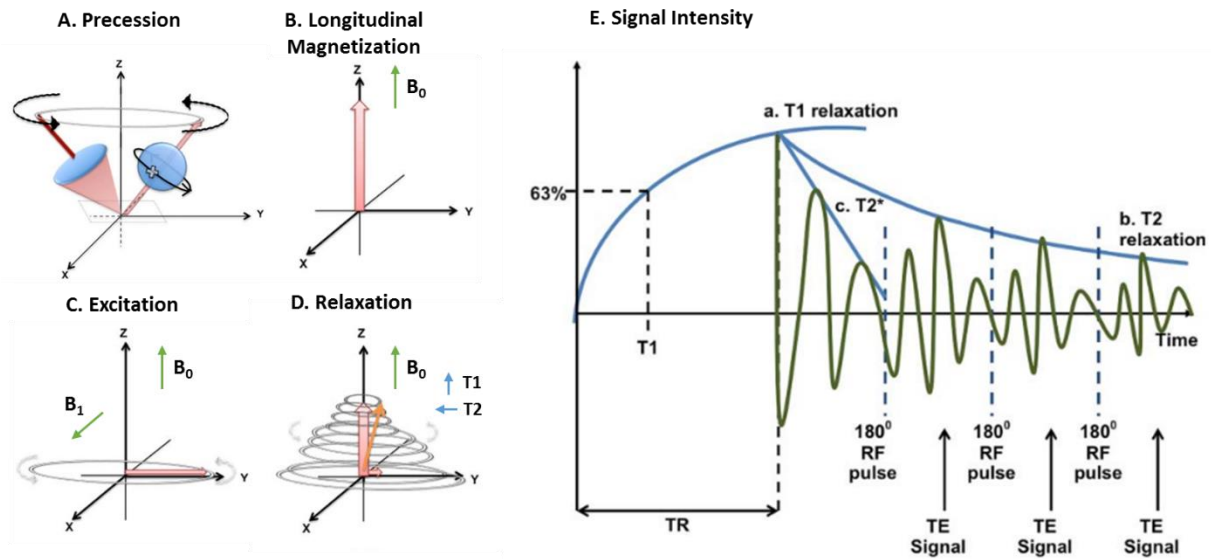


**Figure 15:** The precession, excitation, and relaxation of spins in MRI. A) Protons precess in a magnetic field. B) The protons align in the magnetic field of the MRI, $B_0$, creating a magnetic moment along the z-axis or longitudinal plane. C) An excitation RF pulse, $B_1$, is applied and the magnetic moment shifts to the y-axis, or transverse plane. D) After the RF pulse, the magnetic moment shifts back to the longitudinal plane. The parameter T1 measures the longitudinal magnetization and the parameter T2 measures the transverse magnetization. E) T1 is measured as the time it takes for the magnetic moment to reach 63% of its initial intensity in the longitudinal plane. $T2^*$ is the time it takes for signal in the transverse plane to decrease due mainly to inhomogeneities in the field. T2 is measured by repeat RF pulses and measurement of maximum TE, echo time, signal. Reproduced from Postgraduate Medical Journal, **Ref. 89**, copyright 2013 with permission from BMJ Publishing Group Ltd.

32

to show as brighter areas or reducing T2 values to cause darker areas to appear where they are

concentrated, as seen in **Figure 16**.[56]
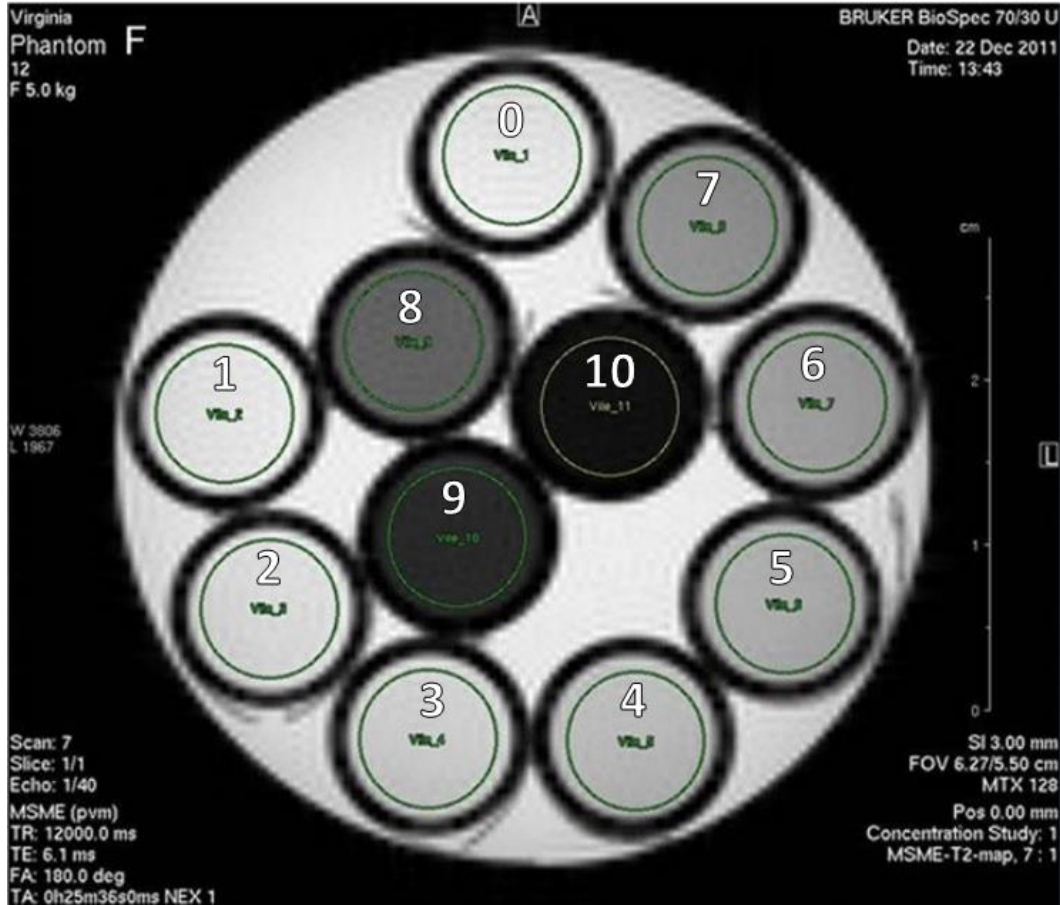


**Figure 16:** MRI phantom image for super paramagnetic iron oxide nanoparticles (SPIONs) with increasing concentrations of Fe. Water, vial #0, is compared to vials containing SPIONs at increasing concentration of Fe from #1 – 0.51 mg/L to #10 – 69.3 mg/L. This T2 weighted image shows decrease in signal at increasing concentrations of SPIONs, demonstrating its ability to decrease T2 time. © American Journal of Nuclear Medicine and Molecular Imaging, Creative Commons Attribution Noncommercial License.**[56]**

### 2.6.2.1.  Chemical Exchange Saturation Transfer (CEST) MR Imaging and pH Mapping

Chemical exchange saturation transfer (CEST) MR imaging is an MRI contrast imaging method

by which endogenous or exogenous compounds containing exchangeable protons or molecules

are selectively saturated and, after transfer of saturation, detected indirectly through

enhancement of water signal, as seen in **Figure 17**.[90] Quantification of this signal is translated

33

into maps that can be overlaid onto background MRI. CEST agents are beneficial compared to typical contrast agents due to their ability to be turned on and off, allowing unaltered images to be captured at the same time, they can be sensitive to environmental parameters such as temperature, metabolite concentration, or pH, allowing quantitative measurement, and can be administered as a cocktail for multiplex imaging, probing several targets. Applications for CEST imaging include metabolite detection, imaging of mobile proteins or peptides in tissues, metal
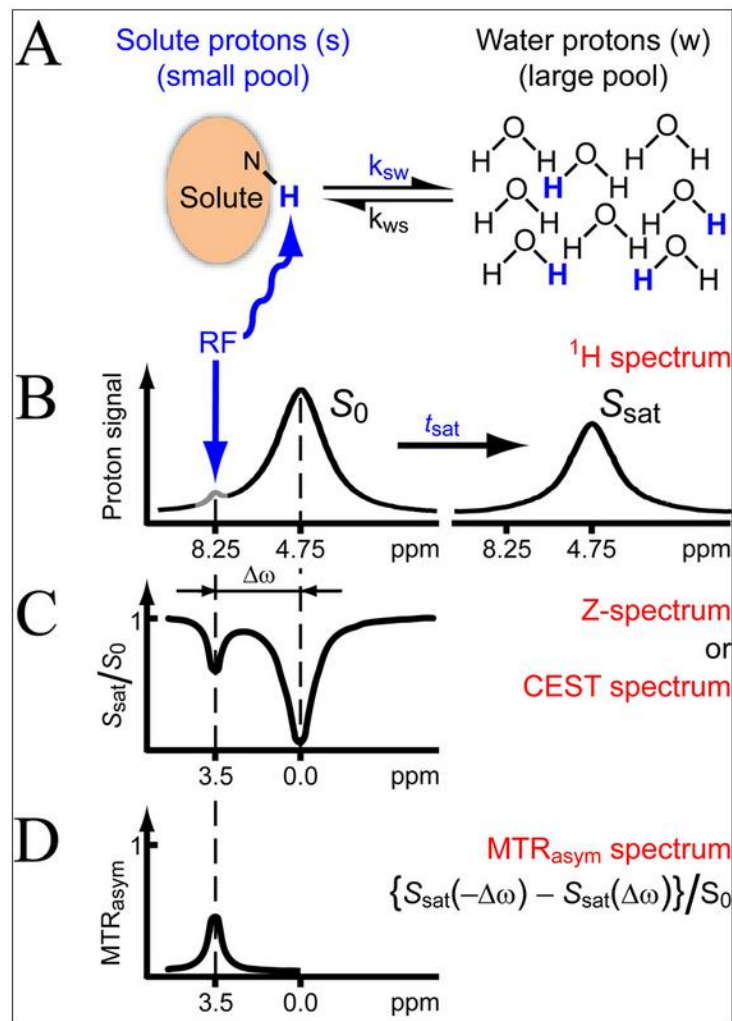


**Figure 17:** Principles of chemical exchange saturation transfer (CEST) MR imaging. A,B) An endogenous or exogenous agent with exchangeable protons are saturated at their resonance frequency, here 8.25 ppm, which is visible initially ($S_0$, B, left) until they are exchanged with water molecules after a period, $t_{sat}$, decreasing the water signal at 4.75 ppm ($S_{sat}$, B, right). C) Normalized water saturation ($S_{sat}/S_0$) generates a Z- or CEST spectrum where the direct saturation water peak is assigned 0 ppm. D) Magnetization Transfer Ratio (MTR) asymmetry analysis of the Z-spectrum removes the direct saturation peak. Reprinted by permission from John Wiley & Sons Inc.: Magnetic Resonance in Medicine, **Ref. 90**, copyright 2011.

34

ion detection, liposome labeling, nanoparticle/polymer labeling, protein binding, RNA and

DNA-protein binding, temperature imaging, detection of enzyme activity, CEST reporter genes,

and pH imaging.[91]

Though many CEST methods have only been used for *in vitro* imaging, pH imaging has shown

promise for *in vivo* determination of acidic and basic regions and shows great promise for

clinical application. Although endogenous agents for CEST are ideal, pH CEST imaging uses

established CT contrast agents so clinical translation becomes much easier. These CT contrast

agents are iodine based, but contain amide protons for exchange with water, such as iopromide,

iobitridol, and iopamidol (trade names Ultravist, Xenetix, and Isovue, respectively). pH imaging

with these contrast agents is based on the pH dependent saturation transfer of several amide

protons within the contrast agent which can be expressed as a ratio that relates to the pH, as seen

in **Figure 18**.[92] Measurement of the ratio of the saturation transfer of these protons allows for

concentration independent measurement of pH, as seen in **Figure 19**.[93] *In vivo* imaging of mice

after intravenous injection of iopamidol has been used to determine pH in tumors and kidneys, as
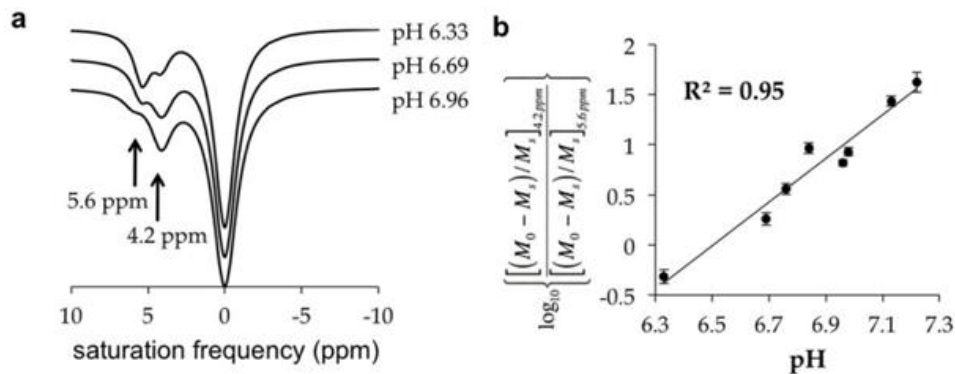


**Figure 18:** pH responsive amide proton peaks in iopamidol and ratiometric measurement of pH. a) Iopamidol has two amide protons with different chemical exchange saturation based on pH at 5.6 ppm and 4.2 ppm, seen in the Z-spectrum of solutions ranging in pH from 6.33 to 6.96. b) Based on the known pH of solutions with iopamidol, a correlation and equation can be created for the ratiometric determination of pH using the MTR spectrum from the two peaks. Reprinted by permission from John Wiley & Sons Inc.: Magnetic Resonance in Imaging, **Ref. 92**, copyright 2013.

35

seen in **Figure 20**.[94] Iopamidol has also been tested in a human volunteer using a clinical 3T MR

scanner to determine the pH of urine in the bladder, compared to pH of a urine sample, with

good correlation.[95]
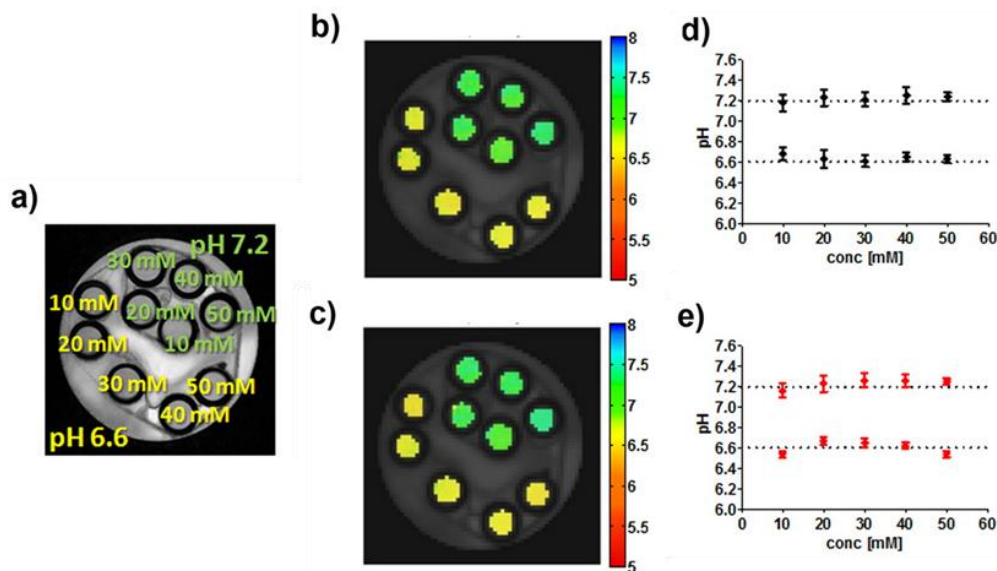


**Figure 19:** Demonstration of concentration independent response of iobitridol as pH contrast agent. a) Iobitridol-containing phantoms at different concentrations (10–50 mM) and pH values (6.6 and 7.2). MRI-CEST pH maps show RF irradiation powers of 1.5/6 µT (b) and of 3/6 µT (c). Mean pH values calculated for several concentrations upon ratioing 1.5/6 µT (d) and of 3/6 µT (e) demonstrating concentration independent pH measurements. © American Chemical Society, ACS AuthorChoice License.[93]
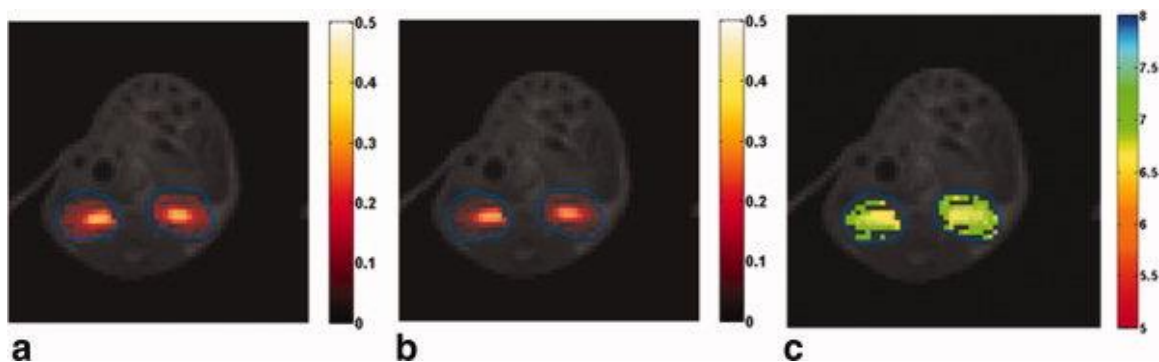


**Figure 20:** Saturation transfer maps of iopamidol in the kidneys, with ratiometric pH map. Saturation transfer maps were created for amide proton peaks at 4.2 ppm (a) and 5.5 ppm (b). After applying the equation for ratiometric pH dependence, a pH map is created showing slight acidity in the kidneys (c). Reprinted by permission from John Wiley & Sons Inc.: Magnetic Resonance in Imaging, **Ref. 94**, copyright 2010.

## 2.7.　Fluorescence Imaging and SNARF pH Indicators

Fluorescence imaging is based on the emission of light from a substance that has absorbed light or other electromagnetic radiation, as seen in **Figure 21A**.[96] The emitted light is always of lower energy and higher wavelength than the absorbed light, seen in **Figure 21B**.[97] Seminaphtharhodafluor (SNARF) compounds are a class of fluorescent molecules that have pH sensitive fluorescent emission, as seen in **Figure 22**.[98] These compounds can be made with carboxylic acid, which makes them cell impermeable for determining external pH, or with acetate ester, which causes cell uptake and can determine intracellular pH. Using a multispectral fluorescence imaging system, images of cells or tissue treated with SNARF can be analyzed to determine the pH based on the shift in fluorescent peaks.
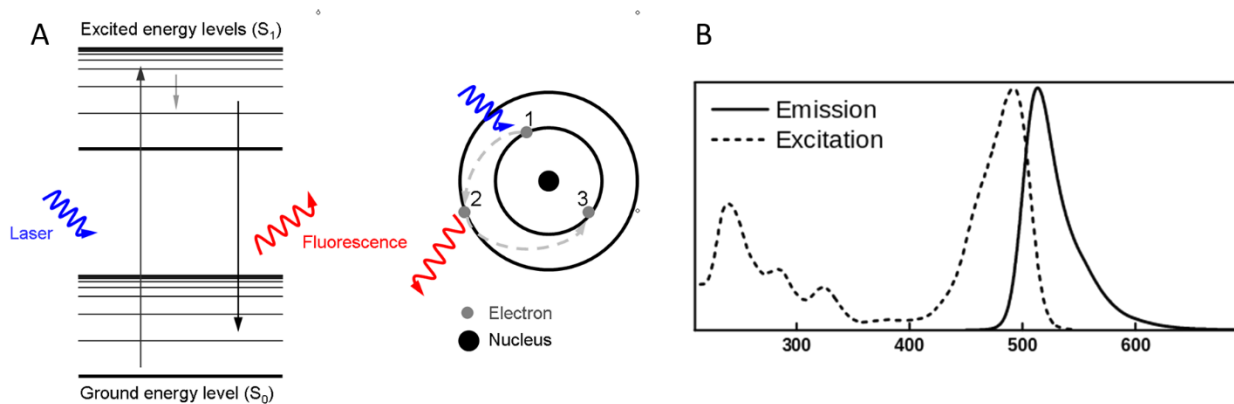


**Figure 21:** Fluorescence of compounds is due to excitation and emission by electrons in the compound. A) Electrons in the compound are excited from ground state (1) to an excited state (2) by in incident photon (blue), and when they return to ground state (3) they lose energy in the form of light at an energy slightly below the incident photon at a longer wavelength (red). B) Fluorescence spectrum demonstrating wavelengths absorbed (dashed) and emitted (solid) by a fluorescent compound, fluorescein. A) Username: Mythealias / Wikimedia Commons / Public Domain.[96] B) © Username: Zadelrob / Wikimedia Commons / CC BY-SA 3.0.[97]
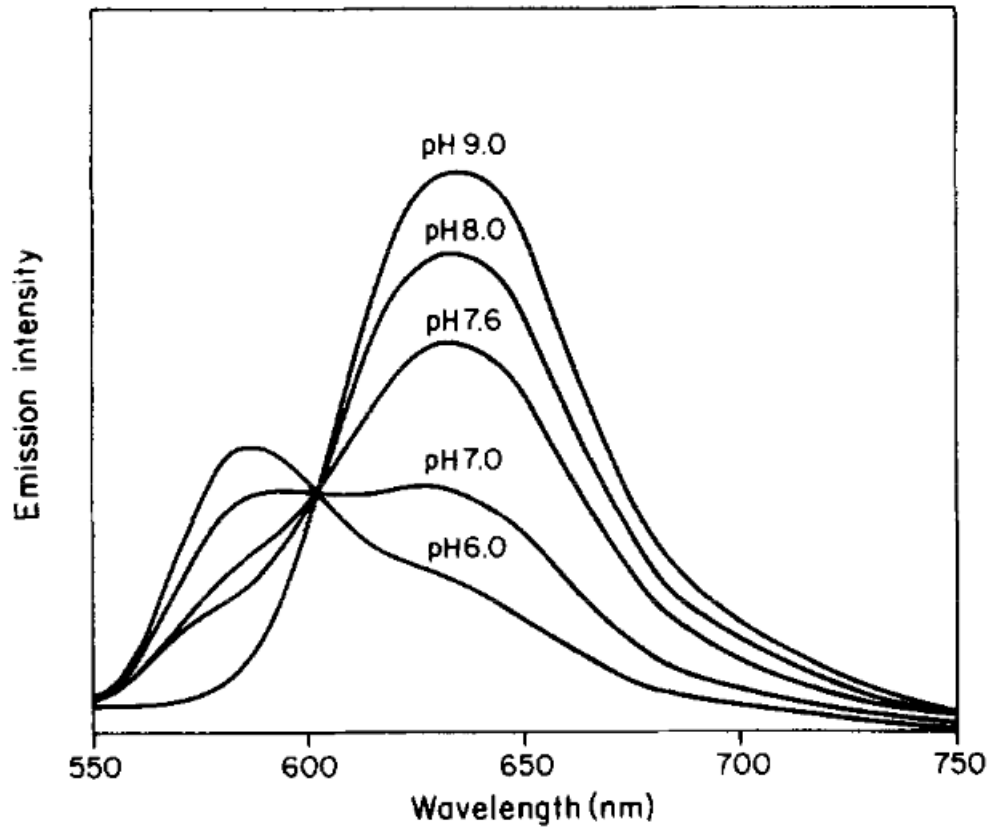
**Figure 22:** pH dependent fluorescence emission by SNARF-1. SNARF-1, when excited at 534 nm, shows a shift in fluorescent peak from 580 nm to 640 nm as its pH is increased from 6.0 to 9.0. Reprinted by permission from Elsevier: Analytical Biochemistry, **Ref. 98**, copyright 1991.

# 3. Chapter 3 - Approach and Methods

## 3.1.    *Approaches to Gaps in Current Research on CONPs*

Based on the current literature, this work aims to fill in some significant gaps in research on cerium oxide nanoparticles that will hopefully advance their application towards the clinic as a radioprotective drug. The first area to be studies is the biodistribution of CONPs once injected into the body. This will be addressed through the synthesis of radiolabeled CONPs which can be used for PET imaging and *ex vivo* biodistribution. Small molecule and polymer coatings on the CONPs will also be studied to determine if altering CONPs' size and surface charge affects their biodistribution. With the new synthesis of coated CONPs, it will be determined if they retain the same antioxidant properties as uncoated CONPs. Their toxicity *in vitro* will also be examined. To determine their efficacy, the coated and uncoated CONPs will be tested for their radioprotective properties in both tumor (*in vitro* and *in vivo*) and normal tissues (*in vivo*). Their protection of normal tissue will be compared to the clinically available drug amifostine to compare efficacy. Finally, the mechanism of action of changes in radioprotection in normal and tumor tissue will be examined. The prevalent theory on CONPs lack of protection of tumor tissue is that the acidic pH microenvironment of the tumor prevents radioprotection. This theory will be tested *in vitro* and *in vivo* with a molecular imaging approach. By focusing on these gaps in the research, this work presents novel contributions that may have an immediate impact on the translation of CONPs into the clinic.

39

## 3.2. Synthesis of Non-Radiolabeled and $^{89}$Zr radiolabeled CONPs

Synthesis of radiolabeled and non-radiolabeled CONPs is a single pot co-precipitation reaction. Reactants include cerium(III) nitrate hexahydrate ($Ce(NO_3)_3 \cdot 6H_2O$), small molecule or polymer for coating, and ammonium hydroxide ($NH_4OH$). The small molecules and polymers used in coating CONPs include citric acid, ethylenediaminetetraacetic acid (EDTA), dextran T10-amine (DT10-NH$_2$), dextran T10-polyethylene glycol (DT10-PEG), dextran T10-sulfobetaine (DT10-SB) and poly(acrylic acid) (PAA). While all other polymer and small molecules in the synthesis of CONPs were purchased and used without further modification, the DT10-NH$_2$, DT10-PEG, and DT10-SB polymers were synthesized *de novo*. $^{89}$Zr is produced by proton irradiation of a natural yttrium target on a PET-Trace Cyclotron by IBA Molecular (Richmond, VA, USA). $^{89}$Zr activity is radiochemically separated from the target using ion exchange chromatography to produce $^{89}$Zr-oxalate in a solution of 1M oxalate. Due to the precipitation of cerium salts when added to oxalate, the radioactive reaction yields of radiosynthesis of CONPs with $^{89}$Zr-Oxalate were very low, less than 50% with significant precipitation visible in the reaction vial. To prevent precipitation and increase radioactive yield, $^{89}$Zr-Oxalate was converted to $^{89}$ZrCl$_2$ in 1M HCl.

### 3.2.1. Functionalized Dextran T10 Synthesis

The dextran T10 based polymers used for coated CONP synthesis were synthesized *de novo* using previously described methods.[52] Briefly, 2-amino-ethyl-sulfobetaine (2-amino-ethyl-SB) and amino-polyethylene glycol-600 (amino-PEG-600) were synthesized as precursors for synthesis of dextran T10-sulfobetaine and dextran T10-polyethylene glycol, respectively. N,N-

40

dimethylethylenediamine was purchased and used unaltered for synthesis of dextran T10-NH₂. Dextran T10 (1.0 g) was dissolved in DMSO (10 mL) with gentle heating and then cooled to room temperature. N,N-Diisopropylethylamine (DIPEA, 0.64 mL) and di(N-succinimidyl)carbonate (DSC, 0.48g/0.96g/1.44g) in dimethyl sulfoxide/dimethylformamide (DMSO/DMF, 2mL/2 mL) were added dropwise to the resultant solution with stirring to activate the hydroxyl groups. The reaction mixture was left for 3 hours at room temperature and a corresponding amount of amino derivatives (2-amino-ethyl-SB, amino-PEG-600, or N,N-dimethylethylenediamine) dissolved in DMSO or DMF or H₂O (1.5 mL) was added to the reaction mixture swiftly. The reaction was kept overnight at room temperature while stirring. Functionalized DT10 (DT10-SB, DT10-PEG or DT10-NH₂) was dialyzed against DI water (dialysis cassette, molecular weight cut off: 2000 Da) and then dried under vacuum. The functional degree could be tuned to 10%, 20% or 30%. DT10-SB-20%, DT10-PEG-20% and DT10-NH₂-10% were used for the synthesis of coated CONPs.

### 3.2.2. Preparation of $^{89}ZrCl_2$

$^{89}$Zr-Oxalate in 1M oxalate was converted to $^{89}ZrCl_2$ in 1M HCl using previously described methods.[99] Briefly, a Waters Sep-pak Light QMA strong anion exchange cartridge was pre-washed with 6mL acetonitrile, 10mL 0.9% saline, and 10mL nanopure water. The $^{89}$Zr-Oxalate was loaded onto the column and then rinsed with 40mL nanopure water. The $^{89}$Zr activity is retained (>99%) in the column and oxalate is washed out by the water (<0.2% retained). The $^{89}$Zr is eluted by 1mL 1M HCl and fractions are collected, with the highest activity fractions combined (>90%) and used for subsequent reactions.

41

### 3.2.3. Synthesis Scheme

An outline of the synthesis of coated and uncoated CONPs, with incorporation of [89]Zr is seen in

**Figure 23**. Before beginning synthesis of CONPs, all of the reactants were prepared in solution,

as detailed in **Table 4**. Using the ratios described in **Table 4**, the non-radiolabeled synthesis is

detailed below:

(1) Combine the cerium salt and small molecule/polymer for coating in a vial. If synthesizing uncoated-CONP, only cerium salt is required
  a. For citrate-CONP, a neutral solution is required to prevent the precipitation of cerium salt in EDTA. Mix citric acid and EDTA first, and then add NaOH to neutralize, testing that the pH is between 6-7 (approximate volume of NaOH required to neutralize is given). Add cerium nitrate solution last.
(2) By adding water, bring the total volume of the solution to 1mg $Ce(NO_3)_3 \cdot 6H_2O$ per 300 µL
(3) Fill a separate vial with $NH_4OH$ (2.8% $NH_3$ in water, 10x dilution of concentrated 28% $NH_3$ stock) to the same volume as the cerium salt solution in step (2). Using a stir bar, stir the solution at 400 rpm.
(4) To the $NH_4OH$ solution, add the cerium salt solution from step (2) in a bolus.
(5) Allow the reaction to react for ~20 hours at room temperature (overnight)
(6) Pass the solution through a 0.2µm filter to remove large particles, rinsing the vial and filter with water to maximize yield
(7) Do not use 0.2µm filter for uncoated CONPs (will not pass through filter) Transfer the solutions into a molecular weight cutoff (MWCO) centrifugal filter, diluting the solution to the recommended maximum volume and spin at ~5000 rcf for 30 minutes at room temperature to remove any unreacted reactants.
  a. Use 3 kDa centrifuge filter for citrate/EDTA and PAA coatings
  b. Use 30 kDa centrifuge filter for uncoated and DT10-NH$_2$, DT10-PEG, and DT10-SB coatings
(8) Repeat step (7) 3 times, disposing of the filtrate and diluting the CONP solution each time to the recommended maximum volume
(9) Collect the CONPs directly from the MWCO filter and rinse several times to collect entire sample
(10) Bring the final collected solution to a standard volume
(11) Prepare samples for ICP-OES as detailed later in **Section 3.2.1.1**

| Reactant | Concentration | Mass Ratio | Volume Ratio | Mass Example | Volume example |
|---|---|---|---|---|---|
| $Ce(NO_3)_3 \cdot 6H_2O$ | 100 mg/mL | 1 | 1 | 4 mg | 40 µL |
| $NH_4OH$ | 2.8% $NH_3$ in $H_2O$ | - | 15 | - | 600 µL |
| Citric Acid[a] | 200 mg/mL | 2.7 | 1.35 | 10.8 mg | 54 µL |
| EDTA[a] | 50 mg/mL | 0.3 | 0.60 | 1.2 mg | 24 µL |
| NaOH[a] | 160 mg/mL | 1.6 | 1 | 6.4 mg | 40 µL |
| DT10-$NH_2$[b] | 200 mg/mL | 2.5 | 1.25 | 10 mg | 50 µL |
| DT10-PEG[c] | 75 mg/mL | 2.5 | 3.33 | 10 mg | 133.3 µL |
| DT10-SB[d] | 100 mg/mL | 2.5 | 2.5 | 10 mg | 100 µL |
| PAA[e] | 100 mg/mL | 2.5 | 2.5 | 10 mg | 100 µL |
| $^{89}ZrCl_2$[f] | Variable | - | - | - | - |

**Table 4:** Reactants for non-radiolabled and radiolabeled CONP synthesis with several coatings. While concentrations of starting reactants may vary, the mass ratio of the reactants should remain the same.
[a]used only for citrate-CONP synthesis
[b]used only for DT10-$NH_2$-CONP synthesis
[c]used only for DT10-PEG-CONP synthesis
[d]used only for DT10-SB-CONP synthesis
[f]used only for radiolabeled CONPs synthesis
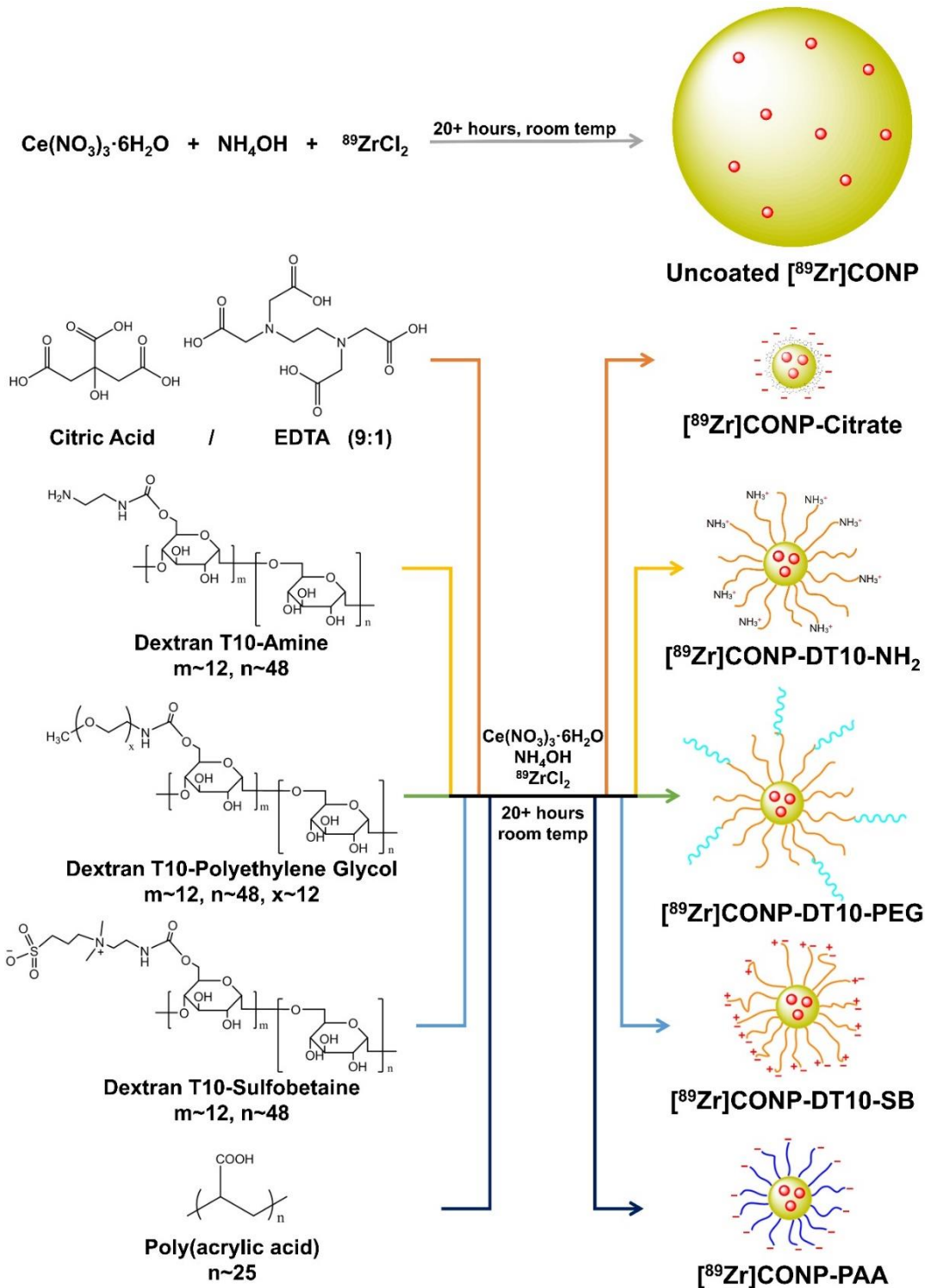
**Figure 23**: Synthesis scheme for uncoated and coated [$^{89}$Zr]CONPs. For uncoated [$^{89}$Zr]CONPs, cerium nitrate salt and $^{89}$ZrCl$_2$ solution was added to ammonium hydroxide to form a core of cerium oxide with stable incorporation of $^{89}$Zr into the lattice. Similarly, coated [$^{89}$Zr]CONPs were synthesized with the addition of polymers/small molecules to the reaction mixture. The uncoated and coated [$^{89}$Zr]CONPs (A-F) show the cerium oxide core (yellow spheres), incorporating $^{89}$Zr (red dots) into the core. Also shown is the smaller size of the coated [$^{89}$Zr]CONPs compared to uncoated, but not to scale.

44

To determine if zirconium could be efficiently incorporated into the core of CONPs, non-radioactive synthesis of stable zirconium labeled DT10-CONPs was performed as a proof of concept. In these reactions, all conditions were kept the same except a solution of zirconyl chloride octahydrate ($ZrOCl \cdot 6H_2O$) was added to the cerium salt solution during step (1). In three separate syntheses, the amount of zirconium added for incorporation was 0.5% (50 µg for 10 mg Ce), 1% (100 µg for 10 mg Ce), and 5% (500 µg for 10 mg Ce) of the mass of cerium in the reaction. These concentrations were varied to reflect the trace amount of $^{89}Zr$, which is on the order of 10 -100 ng.

The synthesis of any coated or uncoated CONPs can be altered to incorporate $^{89}Zr$ into the core of the nanoparticle. The radiosynthesis of CONPs is slightly altered from the synthesis above with addition of $^{89}ZrCl_2$ and dose calibrator measurements for radioactive yield, as detailed below:

(1) Combine the cerium salt and small molecule for coating in a vial. If synthesizing uncoated-CONP, only cerium salt is required
   a. For citrate-CONP, a neutral solution is required to prevent the precipitation of cerium salt in EDTA. Mix citric acid and EDTA first, and then add NaOH to neutralize, testing that the pH is between 6-7 (approximate volume of NaOH required to neutralize is given). Add cerium nitrate solution last.
(2) By adding water, bring the total volume of the solution to 1mg $Ce(NO_3)_3 \cdot 6H_2O$ per 300 µL, minus the volume of $^{89}ZrCl_2$ to be added in step 3
(3) Add a volume of $^{89}ZrCl_2$ with the desired amount of radioactivity to the cerium salt solution
(4) Fill a separate vial with $NH_4OH$ (2.8% $NH_3$ in water, 10x dilution of concentrated 28% $NH_3$ stock) to the same total volume as the final volume of the cerium salt solution in step (3). Using a stir bar, stir the solution at 400 rpm.
(5) To the $NH_4OH$ solution, add the cerium salt solution from step (3) in a bolus.
(6) Allow the reaction to react for ~20 hours at room temperature (overnight)
   a. Measure and record the total activity of the reaction vial in a dose calibrator, noting or setting the time of measurement for decay correction
(7) Pass the solution through a 0.2µm filter to remove large particles, rinsing the vial and filter with water to maximize yield
   a. Do not use 0.2µm filter for uncoated CONPs (will not pass through filter)

45

      b. Measure and record the activity remaining in the 0.2µm filter and empty original reaction vial

(8) Transfer the solutions into a molecular weight cutoff (MWCO) centrifugal filter, diluting the solution to the recommended maximum volume and spin at ~5000 rcf for 30 minutes at room temperature to remove any unreacted reactants.
      a. Use 3 kDa centrifuge filter for citrate/EDTA and PAA coatings
      b. Use 30 kDa centrifuge filter for uncoated and DT10-NH$_2$, DT10-PEG, and DT10-SB coatings
      c. Measure and record the total activity in the MWCO filter

(9) Repeat step (8) 3 times, disposing of the filtrate in radioactive waste and diluting the CONP solution each time to the recommended maximum volume

(10)      Collect the CONPs directly from the MWCO filter and rinse several times to collect entire sample
      a. Measure and record the remaining activity in the MWCO filter

(11)      Bring the final collected solution to a standard volume
      a. Measure and record the total activity collected in CONP solution

(12)      Prepare samples for ICP-OES as detailed later in **Section 3.2.1.1**

Typical addition of $^{89}$ZrCl$_2$ was 0.1 to 1.0 mCi in 10 to 50 µL 1 M HCl.

### 3.2.4. Other CONP Coatings

Several other polymers and small molecules were tested for coating CONPs, including glucose, cyclodextran, mannose, maltose, dextran T10, ascorbic acid, and dehydroascorbic acid. These coatings were abandoned without further study *in vitro* or *in vivo* due to low reaction yields or instability where significant aggregation was evident after a short period in solution.

## *3.3.    CONP Characterization*

CONPs were characterized to determine concentration, size, and surface charge using inductively couple plasma – optical emission spectrometry (ICP-OES), dynamic light scattering, and zeta potential measurement, respectively. A dose calibrator was used during radiosynthesis for radioactive yields.

46

### 3.3.1. Concentration and Yield

To determine the concentration of CONPs in solution, inductively couple plasma – optical emission spectrometry (ICP-OES) was used to measure the concentration of cerium in solution. This value could also determine the reaction yield for CONPs. For radioactive yield, a dose calibrator was used. ICP-OES was also used for testing of incorporation of non-radioactive zirconium into CONPs.

### 3.3.1.1.  Inductively Couple Plasma – Optical Emission Spectrometry (ICP-OES) Measurement of Cerium

Inductively couple plasma – optical emission spectrometry (ICP-OES) is an instrument used to detect trace metals in a sample. It uses an argon plasma torch to ionize metal atoms from a liquid sample, usually in acid solution, which then produce photons at characteristic wavelengths that can be detected by photomultiplier tubes. The amount of light given off from the sample is proportional to the concentration of the metal in solution. This method can detect metals as low as 2 ppb (2 ng/mL). The system used was a Vista-MPX CCD Simultaneous ICP-OES. Preparation of cerium standards used 7% nitric acid as solution and ranged in concentration from 0.25 to 50 ppm and showed linear response across that range, as seen in **Figure 24**. To saturate
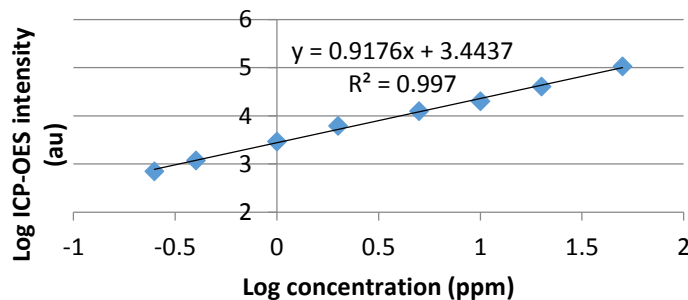
**Figure 24**: Inductively couple plasma – optical emission spectrometry (ICP-OES) of cerium shows good response across a wide range of concentrations. Due to the wide range of response of ICP-OES and the range of concentration of samples that can be used, a log-log plot was used to weigh each concentration equally, here showing concentration ranging from 0.25 ppm (log value -0.6) to 50 ppm (log value 1.7).

47

ionization and increase sensitivity, 0.01 M KCl was added to solution. CONP samples were prepared by adding a volume of CONPs from the stock solution expected to create a concentration within the range of the standards (1 – 100 μL) to 10mL 7% nitric acid solution. The nitric acid dissolves the CONPs, producing free ions in solution for detection. A standard curve was produced from the results of the standards, as seen in Figure X. The same methods of sample preparation were used for determining non-radioactive zirconium incorporation into CONPs by using zirconium standards from 20 to 400 ppb ($R^2 = 0.9964$). AlCl$_3$ (0.1 M) was along with KCl (0.01 M) to increase sensitivity.

### 3.3.1.2. Radiochemical Yield Measurement

Radioactive reaction yields of $^{89}$Zr incorporation into CONPs was done using a Capintec CRC-15 PET ionization chamber based dose calibrator. Using the steps outlined in the [$^{89}$Zr]CONP radiosynthesis detailed above, measurements were taken along the radiosynthesis to determine the yield and if/when the radioactive yield decreased.

### 3.3.2. Size and Surface Charge

The coating of CONPs alters their size and surface charge. To determine these changes in particle size and surface charge, a Zeta Sizer Nano Series ZEN3600 (Malvern, USA) was used. Particle size is measured as the hydrodynamic size in water and is determined by dynamic light scattering (DLS). DLS operates by diffraction of monochromatic light (635 nm) by particles in solution. The diffraction pattern fluctuates in a manner that is due to the Brownian motion of the particles, which can be correlated to the particle size. The diffraction patterns are analyzed by the system correlator which can determine the size distribution of the particles. This method is able

48

to determine particle size down to 1nm. Surface charge is measured as zeta potential. Zeta potential is the electrokinetic potential of a particle compared to the dispersal media. It is measured by electrophoretic mobility whereby an electric current is applied to the solution and particle motion is measured. Concentrations used for hydrodynamic size and zeta potential measurements were at least 0.1 mg/mL Ce.

## 3.4.    Autocatalytic Activity

To ensure the coating of CONPs and $^{89}$Zr incorporation into CONPs does not compromise their unique redox properties, a previous method of measuring their redox reaction with $H_2O_2$ and subsequent cycling back to original oxidative state was used.[43,52] To determine the catalytic activity of CONPs, their reaction with hydrogen peroxide ($H_2O_2$) was monitored using the absorbance of CONPs, which changes depending of the oxidation state on the surface of the nanoparticle, as seen in **Figure 25**. The immediate color change observed when $H_2O_2$ is added to a solution of CONPs indicates the oxidation of $Ce^{3+}$ to $Ce^{4+}$ within the CONPs. This change in absorption is most apparent at a wavelength of 420 nm, so this wavelength was used to measure
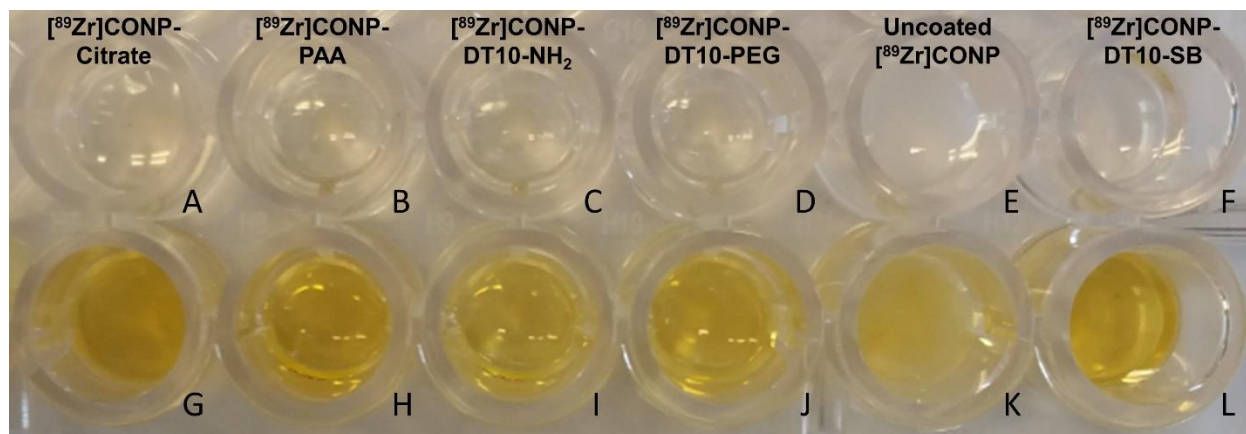


**Figure 25**: Solutions of [$^{89}$Zr]CONPs before and after addition of $H_2O_2$. Solutions of [$^{89}$Zr]CONP-Citrate (A,G), [$^{89}$Zr]CONP-PAA (B,H), [$^{89}$Zr]CONP-DT10-NH$_2$(C,I), [$^{89}$Zr]CONP-DT10-PEG (D,J), Uncoated [$^{89}$Zr]CONP (E,K), and [$^{89}$Zr]CONP-DT-SB (F,L) show very light yellow color before addition of $H_2O_2$ (A-F) and immediate change to dark yellow after addition (G-L). Uncoated [$^{89}$Zr]CONP (E,K) shows milky solution due to large particle size and aggregation while all coated CONPs (A-D, F-J, L) are transparent in solution.

49

the change in absorption over time after the reaction with $H_2O_2$. The solutions gradually shift back to a light yellow over the course of a few days, which indicates the auto-reduction of $Ce^{4+}$ to $Ce^{3+}$ within CONP. The experimental conditions for the autocatalytic reaction measurement was 100 µL of 0.5 mg/mL of each type of CONPs or $[^{89}Zr]CONPs$ was added to a 96 well plate and a multiwell plate reader (Beckman Coulter DTX880) was used to monitor the autocatalytic activity by the absorbance at 420 nm (n=3). 20 µL of 7.5 mM $H_2O_2$ was added to each well to oxidize the CONPs. The absorption was then monitored after addition of $H_2O_2$ over 5 days (t = 0, 1 hour, 1 day, 2 days, 3 days, 4 days, and 5 days). A repeat addition of 20 µL of 7.5 mM $H_2O_2$ was added to each well on day 6 to test the recycling of redox properties. Solutions of CONPs without $H_2O_2$ were used as control to normalize reported percent absorbance.

## 3.5. Cell Culture

Colorectal adenocarcinoma cell lines (COLO-205 and HCT-116) were maintained under standard culture conditions (37º C and 5% $CO_2$) in a humid environment. Cells were grown in DMEM/High glucose medium supplemented with 10% fetal bovine serum. The cells were grown to 70-80% confluency before using in the experiments.

## 3.6. Cell Viability

Cell Titer-Glo Luminescent Cell Viability Assay kit (Promega) was used to evaluate the cytotoxicity of CONPs on COLO-205 and HCT-116 cells. Briefly, $10^4$ cells were plated in opaque 96 well plates in triplicate for each concentration and treated with increasing concentrations of citrate, DT10-NH$_2$, DT10-PEG, DT10-SB, PAA coated and uncoated CONPs and $[^{89}Zr]CONPs$ for 24 hrs. At the end of incubation period Cell Titer-Glo reagent was added to

50

untreated and each treatment groups. The cell viability was assessed by measuring the luminescence, detected by a multiwell plate reader (Beckman Coulter). The luminescent signal generated being directly proportional to the ATP produced by metabolically active cells. The luminescence detected in untreated cells was used as control (100% viability) to calculate percent viability in treatment groups.

### 3.6.1. pH Effects on [$^{89}$Zr]CONP Uptake *In Vitro*

For pH dependent uptake of [$^{89}$Zr]CONPs, cells were incubated in DMEM/high glucose media with 0.1 M MOPS buffer at pHs of 7.4, 7.0, and 6.6. To stabilize the media pH, 0.055 mol MOPS buffer was added to 500mL of the media. The media was put on a heating/stir plate and the temperature was kept at 37°C. A tube was placed in the media and room air (0.5% $CO_2$) was bubbled through the solution. After equilibrating with the room air, small volumes of 6 M NaOH or 6 M HCl were added to the media until pH's of 6.6, 7.0, or 7.4 were reached. Fetal bovine serum (55 mL) was added after bubbling to prevent the solution from bubbling over. Final pH values were ±0.01 pH units. Stability of pH was tested by incubating the media in an incubator at 37°C and 5% $CO_2$. Media was stable at ±0.1 pH units for up to 3 days. The same methods for cell uptake described above were used, with the cells pre-incubated in pH 6.6. 7.0, or 7.4 media. COLO-205 cells grown in pH 6.6 media were not adherent, so the cell pellet was recovered from the supernatant by spinning at 800 rpm and repeat washes with PBS and acid buffer wash were done in a test tube with repeated spinning between each wash.

### 3.7.   *Stability of [$^{89}$Zr]CONPs*

The most important concept in radiolabeling molecules for biodistribution studies is ensuring that the radioactive signal represents the location of the molecule and can continue to do so *in*

51

*vivo* over extended periods of time. During synthesis and collection, [$^{89}$Zr]CONPs are purified using a MWCO filter four times, removing any unreacted $^{89}$Zr, which passes through the MWCO filter, from solution. This should indicate all radioactivity remaining is in the core of the nanoparticle.  To examine the stability of $^{89}$Zr incorporation into the core of [$^{89}$Zr]CONPs, several methods were used. A molecular weight cutoff (MWCO) method was developed to determine stability of $^{89}$Zr in the core of [$^{89}$Zr]CONPs after challenge with a strong chelating agent, desferoxamine (DFO). Reversed phase high-performance liquid chromatography (RP-HPLC) was also used for [$^{89}$Zr]CONPs in water solution and for *ex vivo* plasma samples. The inclusion of inline radioactive and UV detection system allows for simultaneous detection of $^{89}$Zr radioactivity and CONP UV absorption.

### 3.7.1. Desferoxamine (DFO) Challenge

All of the coated and uncoated [$^{89}$Zr]CONPs were incubated in 0.05 M desferoxamine (DFO) for 2 and 24 hours to test for chelation of free 89Zr. A separation test was performed based on size by running samples through a 3,000 MWCO filter. This filter separates [89Zr]CONPs, which are retained in the filter, from free 89Zr bound to DFO, which passes through the filter at >95%. [$^{89}$Zr]CONPs were run within two days of synthesis.

### 3.7.2. Radio- and UV-HPLC

Uncoated and citrate, PAA, DT10-NH$_2$, DT10-SB and DT10-PEG coated [$^{89}$Zr]CONPs in water solution were analyzed by reversed phase high-performance liquid chromatography (RP-HPLC) on a 8 x 300 mm, 200 Å Diol (YMC, Japan) size-exclusion column. Also analyzed were plasma samples of C57BL/6 mice tail vein injected with [$^{89}$Zr]CONPs taken 2 hours post-injection. 20 μL of sample solutions were injected into the HPLC with DI water as the mobile phase and a

52

flow rate of 1 mL/min. Analysis of UV absorbance (254nm; model 2489, Waters) and radioactivity (model B-FC-3300, Bio-scan) permits comparative analysis of CONP and $^{89}$Zr signal, respectively.

## 3.8.    *Spontaneous Colon Tumor Model*

Colorectal cancer was produced in C57BL/6 mice (National Cancer Institute). Mice were given an i.p. injection of the carcinogen azoxymethane (AOM) at 15mg/kg followed by three cycles of colitis induction with dextran sodium sulfate (DSS) in drinking water (2% wt/vol) over 10 weeks, as previously described.[100] Mice were monitored over the course of treatment for diarrhea, blood in stool, and weight loss. Any mice that showed too much distress or lost greater than 20% of their body weight were sacrificed. After tumor growth, some mice developed prolapsed rectums, which were monitored closely and treated with antibacterial ointment. This model is advantageous because of the fast time frame, 10+ weeks, for tumors to develop, and use of spontaneous tumors better mimics human tumor development and response compared to xenograft tumors in immunocompromised nude mice.

## 3.9.    *Biodistribution*

Animal experiments were performed according to the policies and guidelines of the Animal Care and Use Committee (IACUC) at Virginia Commonwealth University. Adult female C57BL/6 mice (NCI) with colon tumors, induced as described above, were injected with the solution of each variation of [$^{89}$Zr]CONPs 0.37-11.1 MBq) in saline via the tail vein (i.v., n=3-6), oral gavage (n=1), or intraperitoneal (i.p., n=1). Mice were given a dose used only for *ex vivo* biodistribution were given a low dose of [$^{89}$Zr]CONPs  Mice were euthanized and blood samples and other major organs were collected at 2 hours and 24 hours post injection. Radioactivity of

53

each sample was measured by gamma counter. The percentage of the injected dose per gram (%ID/g) of tissues was calculated according the total injected dose, results of gamma counting and organ weights.

### 3.9.1. *Ex Vivo* Biodistribution

Mice to be used only for *ex vivo* biodistribution were given a low dose of [$^{89}$Zr]CONPs (5-25 μCi) and organs were excised and collected for gamma counting on a Perkin Elmer Wallac Wizard 1470. The organs excised for counting are given below:

| | | | |
|---|---|---|---|
| (1) | Blood | (9) | Intestine |
| (2) | Urine | (10) | Kidneys |
| (3) | Heart | (11) | Colon |
| (4) | Lung | (12) | Tumor |
| (5) | Liver | (13) | Brain |
| (6) | Gallbladder | (14) | Bone (Tibia) |
| (7) | Spleen | (15) | Feces |
| (8) | Stomach | | |

### 3.9.2. Whole Body Radioactivity

For determining excretion of CONPs, a large dose was given to C57BL/6 mice (89-128 μCi) and the whole body activity was recorded over the course of 7 days using a dose calibrator. Measurements were taken initially, and at 5 minutes, 15 minutes, 30 minutes, 1 hour, 2 hours, 4 hours, 8 hours, 1 day, 2 days, 3 days, 5 days, and 7 days. Body weights were measured initially and at each measurement from 1 day on.

### 3.9.3. *In Vivo* PET/CT Imaging of [$^{89}$Zr]CONPs

For dynamic and static PET/CT imaging, animals were anesthetized (2% isoflurane in oxygen) for about 10 minutes before the animals were positioned in a commercial Multi-modality

54

Preclinical System (Inveon, Siemens Healthcare, PA). For dynamic scans, PET data was acquired for 65 continuous minutes under warm conditions. Two minutes after the start of the image acquisition, the various [$^{89}$Zr]CONPs (70 – 320 μCi) were injected via the tail vein through a previously positioned catheter while the PET image acquisition was already commenced (n=1). After 65 minutes of dynamic scan, a CT scan was also acquired for anatomical reference. Static scans were performed at 2 hours and 24 hours after injection of various [$^{89}$Zr]CONPs (50 – 320 μCi) were injected via the tail vein, with follow-up CT scan. A normalization scan and a calibration phantom of known volume and activity were acquired prior to the studies and the PET images were processed using manufacturer recommended procedures. Multiple frame dynamic sequences and ordered subsets expectation maximization three dimensional - maximum a posteriori (OSEM3D-MAP) reconstructions were done using Inveon Acquisition Workplace 1.5 (Siemens Healthcare, PA) and were used for image analysis in the Inveon Research Workplace 4.1 (Siemens Healthcare, PA).

## 3.10.    Irradiation and Radiation Therapy

Two separate systems were used for irradiation of cell culture or mice. A Cesium-137 ($^{137}$Cs) irradiator was used for cell culture and whole body mouse irradiation, while a small animal radiation research platform (SARRP) was used for stereotactic mouse irradiation.

### 3.10.1.    Cesium-137 Irradiation

A $^{137}$Cs source was used for irradiation of cell culture and whole body irradiation of mice. Cell cultures were given a dose of 5 Gray, while mice were given a whole body dose of 10 Gray. Mice were sacrificed immediately following whole body irradiation, so no side effects were experienced.

55

### 3.10.2. Small Animal Radiation Research Platform (SARRP)

The small animal radiation research platform (SARRP) is a radiation system capable of mimicking clinical conformal RT in animal models. The platform simulates doses, cell damage, and side effects produced by clinical RT. The system has a dual source x-ray tube, allowing for cone beam CT imaging and treatment plans that can be developed using 3D software. The treatment plans can be based on pre-clinical imaging through multi-modality image registration encompassing PET, SPECT, MRI, and other CT images. Treatment plans are developed on the SARRP using custom Slicer 3D. The CT scan is transferred to the Slicer 3D software as a DICOM image which contains attenuation information. Using this data, segmentation is performed to determine the soft and hard tissue structures in the mouse, including lungs, fat, tissue, and bone, as seen in **Figure 26**. This data is used to calculate the time of irradiation for the dose prescribed. Several isocenters can be selected for the irradiation of tissue. Beam placement can be done completely in three dimensions with the platform rotatable and the
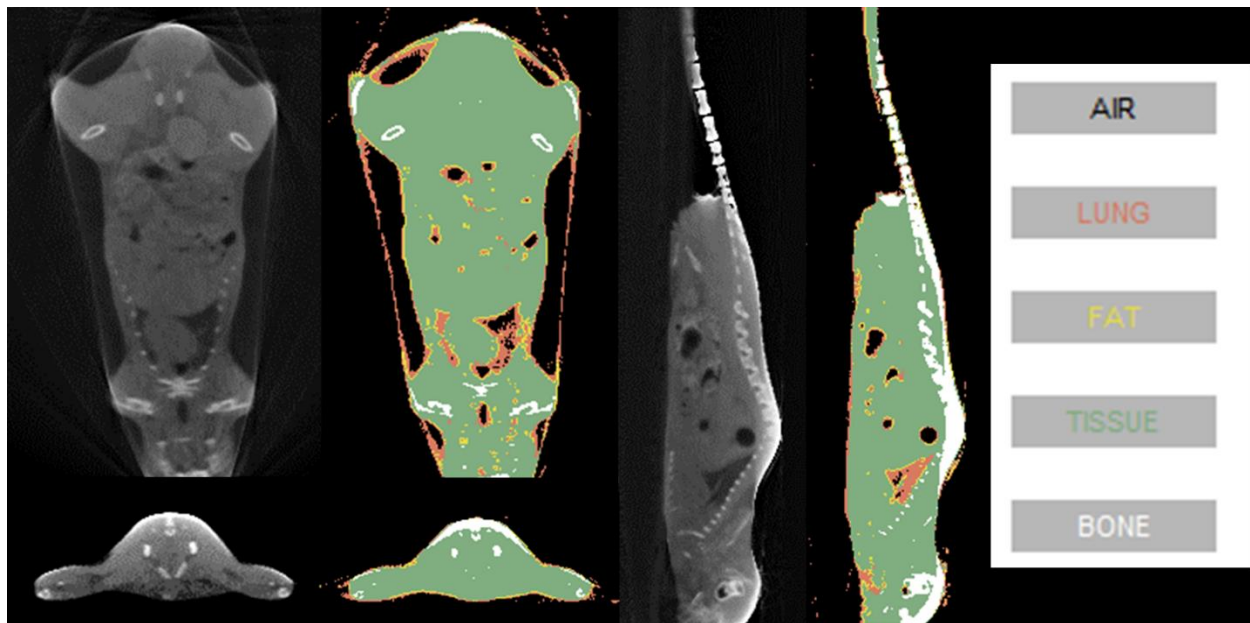


**Figure 26**: Segmentation of SARRP CT. The SARRP system is capable of taking a CT scan of the mouse on the platform for radiation treatment planning. To accurately compute dose and irradiation time, segmentation is performed to tell the system the density of the tissue being irradiated, including lung, fat, tissue, and bone. Views are coronal (top left), axial (bottom left), and sagittal (right).

56

beam head able to rotate in a circle around the platform, as seem in **Figure 27**. The collimators

available range in size from 1 mm circle to 10 mm square for precision dose to specific areas.
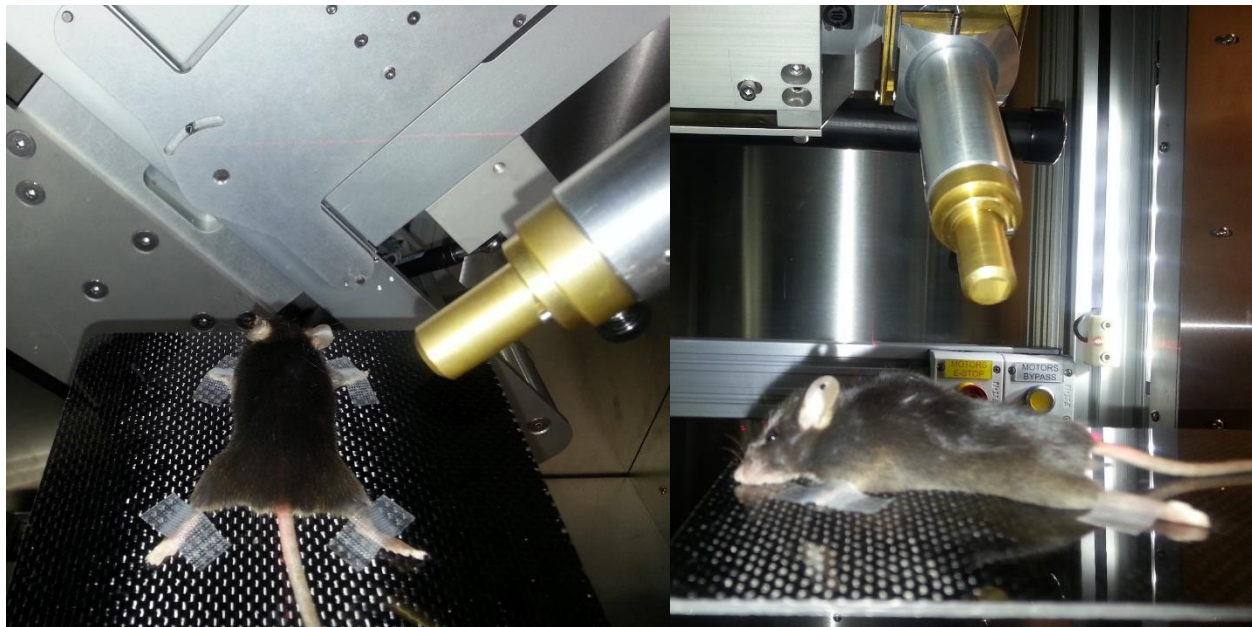


**Figure 27**: Mouse and beam collimator in place for colon irradiation. Mice are anesthetized with ketamine/xylazine and immobilized on the carbon fiber platform, which is able to rotate 360° and move up and down in the z-plane. The beam collimator can move around the mouse 360°, shown here at a 45° angle. Collimators can range in size from 1 mm circle to 10 mm square, seen here.

### 3.10.3.  Normal Colon, Colon Tumor, and Xenograft Irradiation

Based on mouse anatomy, which have a colon that travels along the midline, normal mice and

colon tumor bearing mice were irradiated along the midline from the rectum to 3 cm towards the

cranium to irradiate the entire colon. The beam profile was developed with 2 beam positions

used at each of 3 isocenters. The first isocenter was selected to cover the entire rectum and each

subsequent isocenter was placed exactly 10 mm cranially. The use of the 10 mm collimator

allows for placement of beams directly adjacent without overlap or gaps in dose, as seen in

**Figure 28**. Two beams were used at each beam location at 45° and -45° to prevent high surface

dose deposition and avoid attenuation of the beam by the spine. Xenograft tumor bearing mice

الﻤﻨﺎرة للاستشارات
www.manaraa.com

with tumors on their rear flanks were irradiated from a single beam position, as seen in **Figure 29**.
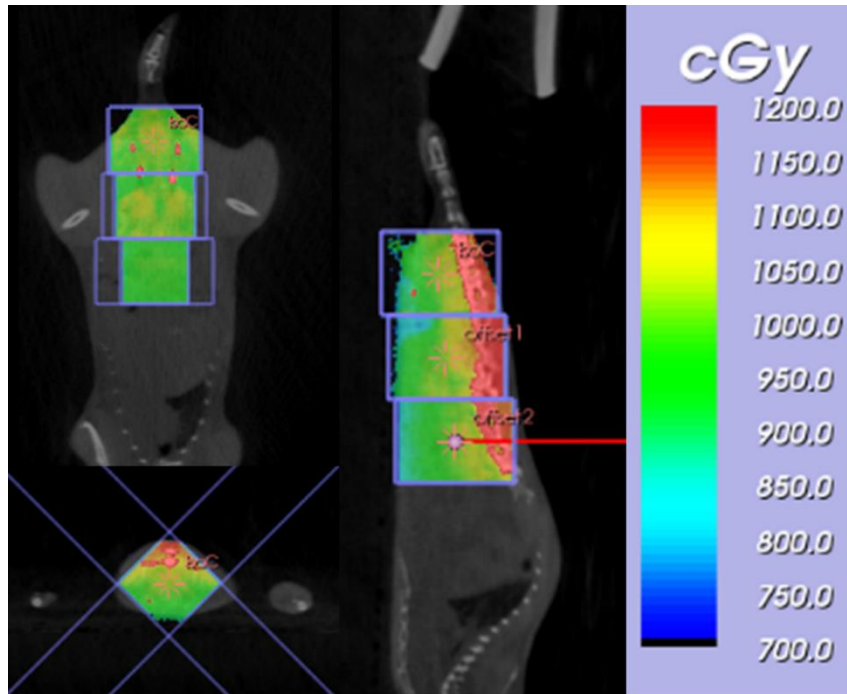


**Figure 28**: Treatment planning for mouse colon irradiation. Three isocenters are placed 10 mm apart for use of the 10 mm beam collimator. Beams are planned at 45° angles, outlined in purple, to prevent high skin dose and attenuation by the spine. Dose is 10 Gy with even distribution across the whole colon, 3 cm from rectum to mid-belly. Views are coronal (top left), axial (bottom left), and sagittal (right).
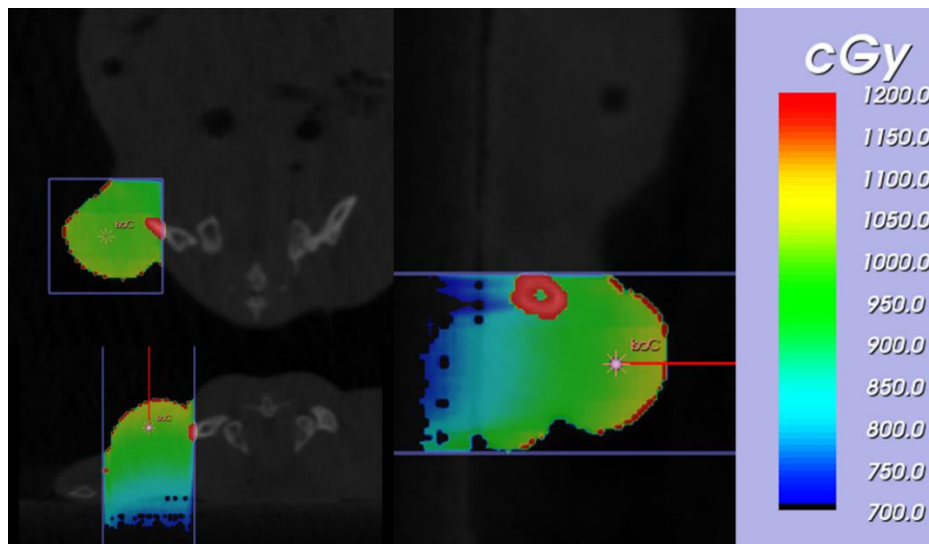


**Figure 29**: Treatment planning for mouse xenograft irradiation. A single isocenter was placed in the center of the xenograft tumor and beam was placed a 0° above the tumor. Dose is 10 Gy with even distribution within the tumor volume. Views are coronal (top left), axial (bottom left), and sagittal (right).

### 3.10.1. CONP and Sodium Bicarbonate Pre-treatment Before Irradiation

The dose given for CONP treatment of mice for therapeutic dose was 1 mg/kg (cerium mass). Based on highest uptake from biodistribution results, mice were given this dose 2 hours before irradiation by tail vein injection in 200 µL saline. To normalize the pH of the tumor microenvironment, treatment with sodium bicarbonate was chosen. Xenograft bearing mice in the group for pH normalization were given 700 µL of 1 M sodium bicarbonate solution by oral gavage. Based on the response of tumor pH in the literature, mice were given sodium bicarbonate three hours before imaging or irradiation.[101]

## 3.11. Evaluation of Response to Radiation

Evaluation of response to radiation was measured from *in vitro*, *ex vivo*, and *in vivo* samples. *In vitro* measurement of pH response was done using clonogenic assays. *Ex vivo* samples of xenograft tumors were also used for clonogenic plating. *Ex vivo* samples of normal colon were stained for apoptosis using a TUNNEL assay. *In vivo* imaging was used to measure tumor response. For spontaneous colon tumors, [$^{18}$F]FDG PET imaging was used to determine tumor metabolic activity. For xenograft tumors, MRI imaging was used to follow tumor growth and regression following irradiation.

### 3.11.1. Effects of pH on Radiation Response of CONP Treated Cancer Cells

HCT-116 colon cancer cells were used to determine the effects of pH on radioprotection of cancer cells by CONPs *in vitro* using clonogenic assay. HCT-116 cells were plated at 500 cells per dish in 10 cm$^2$ dishes. The dishes were separated into sets of controls, PAA-CONP treated only, irradiation only, or PAA-CONP plus radiation and each set was incubated in media pH of

59

7.4 or 7.0 (n=3). The PAA-CONP treated cells were incubated for 2 hours in media containing 15 μg/mL CONP by cerium mass until changing media back to normal. The media was also changed in the other control/irradiation only dishes. For the PAA-CONP plus radiation group, at the two hour time point the dish was irradiated and media was changed after. The irradiated dishes received a 5 Gray dose from the $^{137}$Cs source. Dishes were left alone in the cell incubator for 14 days for colony growth. After 14 days the dishes were removed, media was removed and the colonies were stained with crystal violet (0.5%) for 20 minutes and the dishes were rinsed and colonies counted.

### 3.11.2. Clonogenic Assay of CONP and Irradiation Treatment of Xenograft Tumors

Effects of CONPs on HCT-116 xenograft response to radiation was determined by clonogenic plating of xenograft tumors. Athymic nude mice (NCI) were implanted subcutaneously with 2.5 million HCT-116 cells in matrigel in their rear flank. Mice were separated into groups of control, PAA-CONP treated only, irradiation only, or PAA-CONP plus radiation (n=3). Mice were given whole body radiation dose of 10 Gray from the $^{137}$Cs source. Immediately after irradiation, tumors were excised, minced, and incubated in a solution of 0.25% trypsin and 0.002% DNase I in FBS-free DMEM/high glucose media at 37°C for 20 minutes. After incubation, cells were pelleted and counted and plated at 5000 per dish in 10 cm$^2$ dishes. Dishes were left alone in the cell incubator for 14 days for colony growth. After 14 days the dishes were removed, media was removed and the colonies were stained with crystal violet (0.5%) for 20 minutes and the dishes were rinsed and colonies counted.

### 3.11.3. *In vivo* PET/CT [$^{18}$F]FDG Imaging of Spontaneous Colon Tumors for Response to CONP and Radiation Treatment

To evaluate the effects of CONPs on tumor response to radiation, [$^{18}$F]FDG PET imaging was used before and after irradiation of spontaneous colon tumor bearing animals using the SARRP system. Mice were separated into groups of control, PAA-CONP treated only, irradiation only, citrate-CONP plus irradiation, DT10-PEG-CONP plus irradiation, PAA-CONP plus irradiation, or uncoated CONP plus irradiation (n=3). The initial scan provided a baseline of metabolic activity in the tumors. One day after [$^{18}$F]FDG PET imaging, the mice's colons were irradiated with the SARRP system, as described in **Section 3.10.3**. Two weeks after irradiation, [$^{18}$F]FDG PET imaging was repeated to determine tumor response.

Analysis of [$^{18}$F]FDG PET images was done in Inveon Research Workplace 4.1 (Siemens Healthcare, PA). Regions of interest (ROIs) were created in the coronal plane outlining the colon tumors, careful to avoid inclusion of the bladder due to high urine content of [$^{18}$F]FDG, as seen in **Figure 30**. Tumor volumes were determined using a threshold standardized uptake value
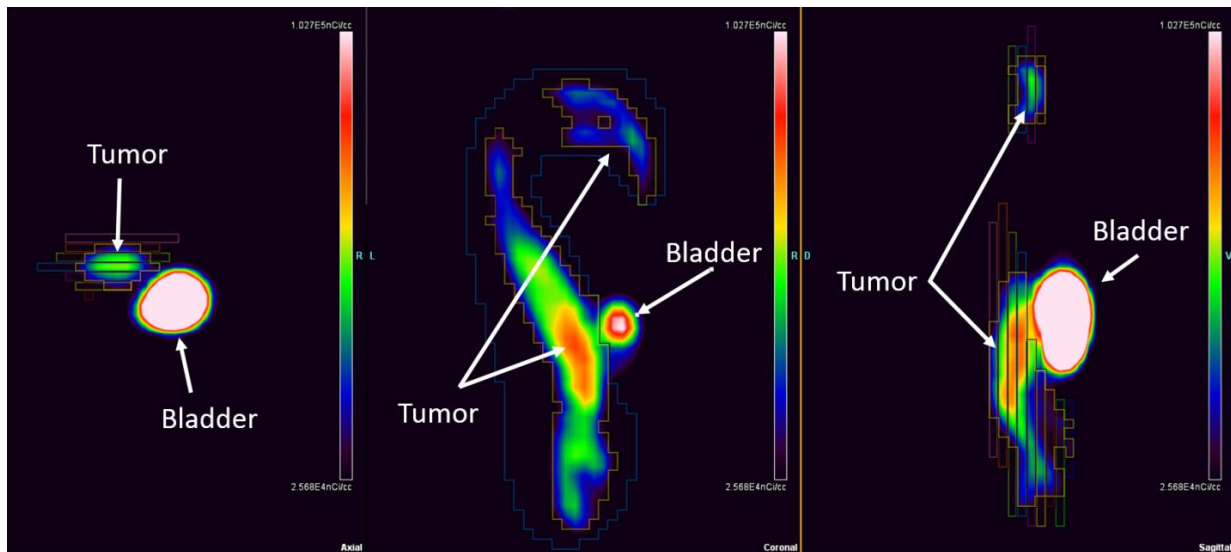


**Figure 30**: Evaluation of tumor volume from [$^{18}$F]FDG PET imaging. Rough outline of tumor was done in all coronal planes, careful to avoid the bladder due to high urine concentration of [$^{18}$F]FDG, seen in the center image as the blue outline. The tumor volume was calculated as any voxels with an SUV greater than 2.5, seen in the center image as the yellow outline. Views are axial (left), coronal (center), and sagittal (right).

61

(SUV) of 2.5, for all images, which corrects for the injected dose and body weight of the animal and does not account for any surrounding [$^{18}$F]FDG tissue uptake.

### 3.11.4. Ex Vivo Normal Colon Tissue Analysis

Testing of the radioprotective effects of CONPs was chosen to be done in the colon because of its high and acute radiosensitivity. The most radiosensitive part of the colon are the crypt stem cells, which divide to produce the cells that migrate and become the colonic villi, as seen in **Figure 31**. To examine colon response to irradiation and potential protection by CONP pre-treatment, C57BL/6 mice were separated into groups of control, irradiation only, citrate-CONP plus irradiation, DT10-PEG-CONP plus irradiation, PAA-CONP plus irradiation, uncoated CONP plus irradiation (n=3). Amifostine pre-treated animals were also irradiated to compare CONPs to an established radio-protective drug (n=3). CONP treatment and amifostine treatment were given 2 hours before irradiation
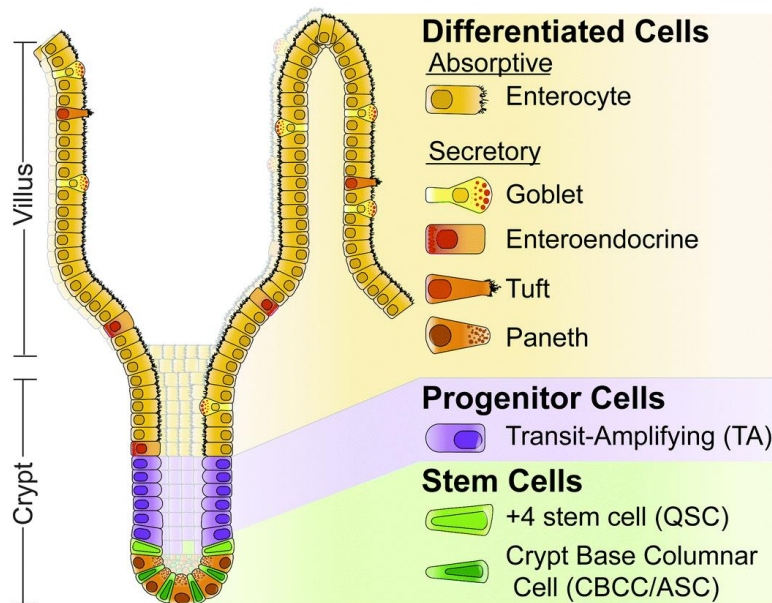


**Figure 31**: Structure of colon villus and crypt cells. The stem cells (green) that divide into the progenitor cells and produce the entire library of colon cells are the most susceptible to radiation damage. © Integrative Biology / CC BY-SA 3.0 [102]

To determine the response of the colon to radiation, measurement of apoptosis was chosen to determine if it could be reduced after radiation treatment. According to the literature, apoptosis is maximally evident in the colon at 4 hours post-irradiation.[103] All mice were therefore sacrificed at 4 hours after irradiation and their colons were excised and frozen in optimal cutting temperature (OCT) compound as a "swiss roll," as seen in Figure 32. A fluorescent terminal deoxynucleotidyl transferase (TdT) deoxyuridine triphosphate (dUTP) nick end labeling (TUNEL) assay (ApopTag® Fluorescein *In Situ* Apoptosis Detection Kit, EMD Millipore) was used to quantify apoptosis. This assay works by detecting the DNA fragmentation that occurs during the apoptosis process. Free 3'-OH termini, or "nick ends," are detected by enzymatic action of TdT and labeled with dUTPs. For the ApopTag assay, digoxigenin labeled dUTPs are included and also label the DNA termini. The tissue is then incubated with an anti-digoxigenin antibody conjugated to fluorescein. This fluorescent labeled antibody can be detected by fluorescent microscopy.



**Figure 32**: "Swiss roll" of mouse colon. A mouse colon is cut longitudinally and rolled from the rectum forward into a cylinder. Cutting along the base of the cylinder allows for staining and microscopy of the entire length of the colon in a small area.

In this experiment, colon cryosections were created at 6 μm on a cryostat (Leica) and placed on a microscope slide, with at least 2 sections from each mouse colon. The sections were preserved at -20°C until staining. The slides were stained using the Apoptag assay and counterstained with nuclear staining 4',6-diamidino-2-phenylindole (DAPI), which binds to the minor groove of double stranded DNA, increasing its fluorescence 20-fold. DAPI was contained in the mounting media (Vectashield) used during slide preparation. Nuclear staining allowed for quantification of apoptosis based on total number of cells present.

Analysis of colon slides was done in ImageJ (NIH) by using a threshold quantification after artifact removal, as seen in **Figure 33** and **Figure 34**. Briefly, apoptosis staining was determined by using the default threshold and sliding it uniformly by 15 units to display only cells that showed apoptosis staining, as seen in **Figure 33 D and H**, and in detail in Figure **34D**. Nuclear staining was determined similarly, using the default threshold with no shifting necessary to
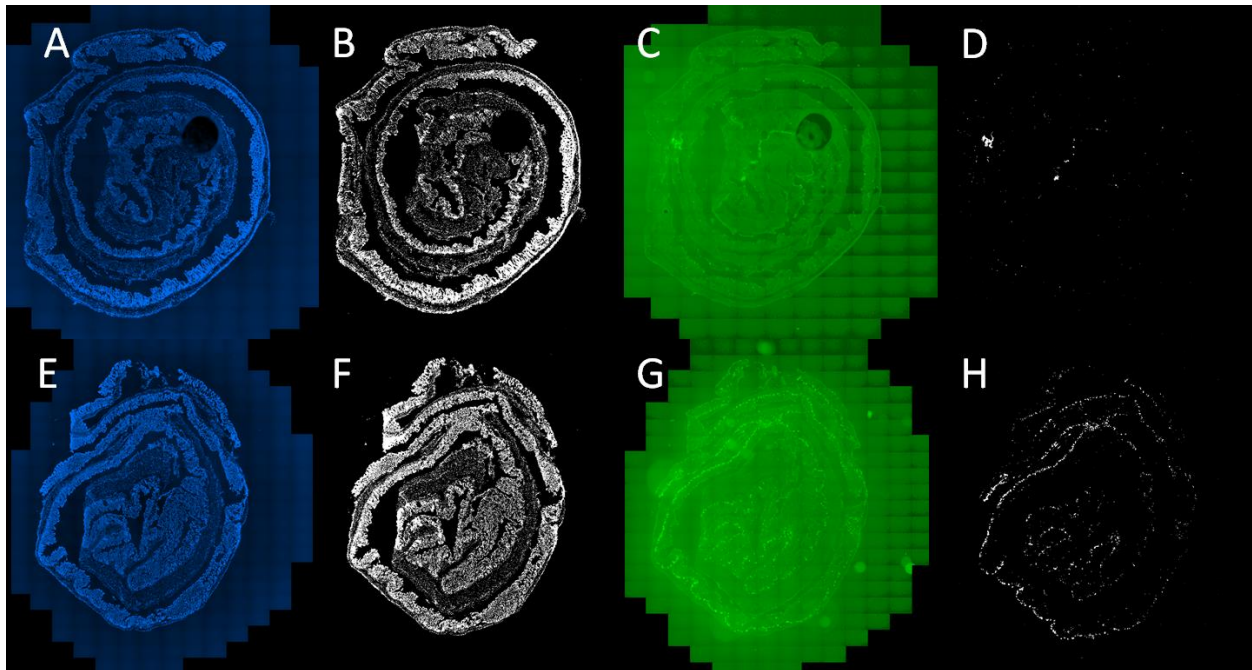


**Figure 33**: Nuclear and apoptosis staining and analysis of swiss rolls of control colon (A-D) and irradiated colon (E-F). DAPI staining of control (A&B) and irradiated (E&F) colons allowed for background nuclear detection, quantified using a threshold, seen in B&F. Apoptag staining of control (C&D) and irradiated (G&H) colons allowed for quantification of cells that were apoptotic. As expected, irradiated colons showed significantly more apoptosis than non-irradiated (H and D, respectively).

64

display only nuclear stained cells, as seen in **Figure 33 B and F**, and in detail in **Figure 34B**. After conversion to binary, ImageJ was used to analyze the area of stained cells. The ratio of apoptosis staining to nuclear staining was used to determine the apoptotic index. It could be seen in the apoptosis staining that the apoptosis in the colon was occurring in the crypt stem cells, which is expected because they are very radiosensitive as highly proliferative cells, as seen in **Figure 34**.
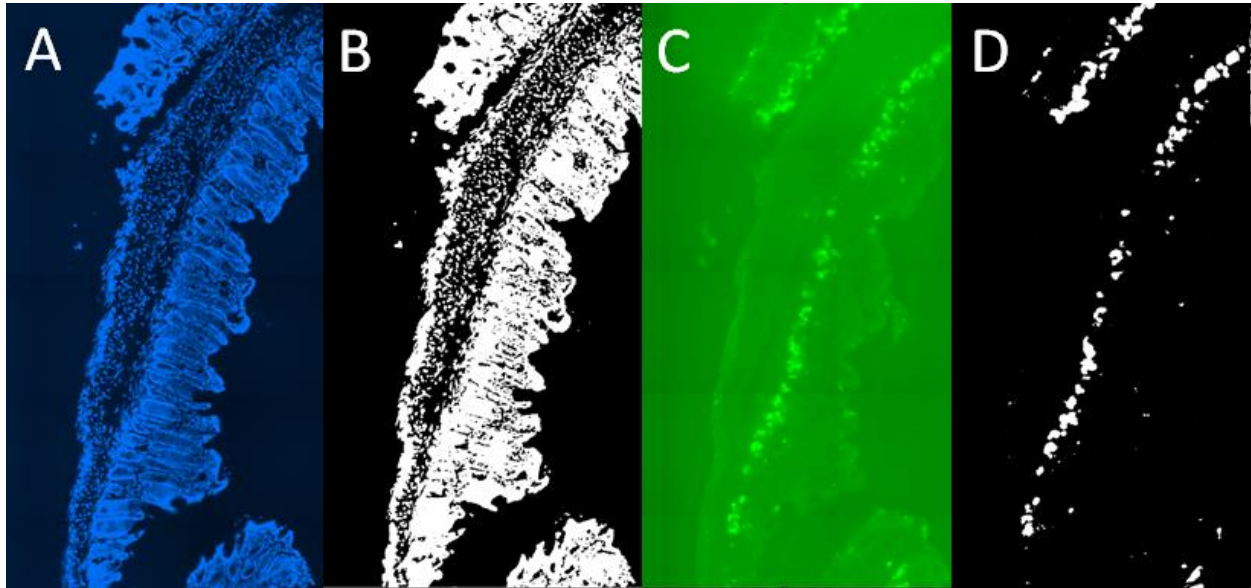


**Figure 34**: Detail of nuclear and apoptosis staining control colon (A&B) and irradiated colon (C&D). Thresholding method allowed for removal of background signal, while only detecting cells stained for nucleus (B) or apoptosis (D).

### 3.11.5. MRI Imaging of Xenograft Tumors to Determine pH Effects on CONPs' Radioprotection of Tumor

To determine if the radiation protection of CONPs within tumors is affected by their pH, mice were treated with sodium bicarbonate to normalize the pH of the tumor microenvironment. In the experiment, mice were separated into groups of control, sodium bicarbonate plus irradiation, PAA-CONP plus irradiation, and sodium bicarbonate and PAA-CONP plus irradiation.

65

To evaluate if pH effects CONPs radioprotective ability in tumors, $T_2$-weighted MRI scans were taken before and 2 weeks after treatment of the xenograft bearing nude mice. Using ImageJ (NIH) and a plugin software called VolumEst, the average tumor volume was determined to compare response to therapy, as seen in **Figure 35**.
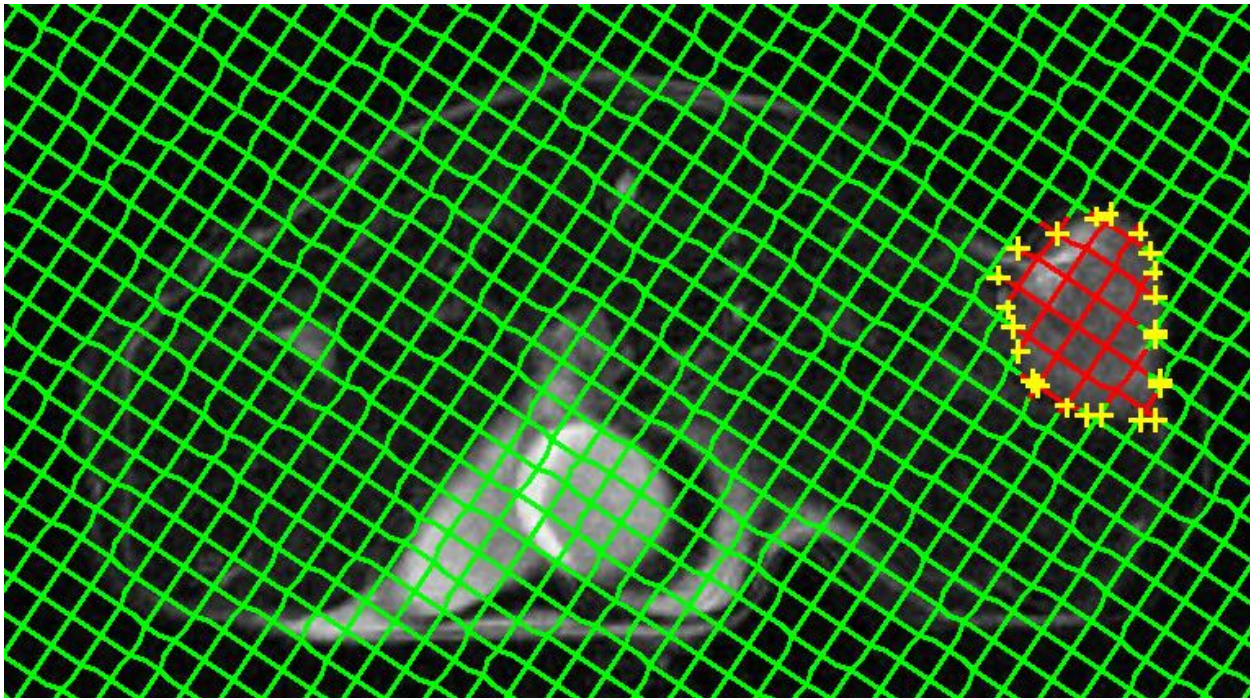


**Figure 35**: Volume estimation of xenograft tumors using ImageJ and VolumEst. DICOM image stacks from $T_2$ weighted MR imaging of xenograft bearing mice before and two weeks after treatment. Tumors were outlined in each slice of the images and the software calculated the tumor volume based on slice thickness.

### *3.12.    pH MRI Imaging*

Using a protocol developed by Dr. Vimalan Vijayaragavan at the Center for Molecular Imaging, VCU, xenograft bearing mice were imaged using a CEST protocol to develop pH maps of the tumors. CEST MRI technique is widely used to calculate pH *in vivo*. In our case we used iopamidol, a CT agent containing amide protons which is exchangeable with bulk water molecule. Athymic nude mice (NCI) with HCT-116 xenograft tumors on their rear flank were anesthetized (2% isoflurane in oxygen) for about 10 minutes before the animals were positioned in a 7 T pre-clinical MRI scanner (Bruker). $T_2$-weighted reference scans were performed before

iopamidol, as clinical grade Isovue 300, was injected by catheter (200 µL, 122.4mg).  The CEST

experimental parameters are as follows: A Rapid Acquisition with Relaxation Enhancement

(RARE) pulse sequence with a saturation module of a block pulse of 5 second duration, with 3

µT amplitude is used for saturation in the frequency offset range -10 ppm to +10 ppm in 0.3 ppm

increment. A slice thickness of 1.5 mm with 9 slices to cover the whole tumor was used. A

matrix size of 64×64 with an isotropic FOV of 35 mm with a rare factor of 64 was used. The

repetition time (RT) and echo time (TE) being 47 sec/4.75 ms. The pH was evaluated based on

ratiometric technique involving the signals at 4.3ppm and 5.5ppm using a Matlab program

developed by Dr. Vijayaragavan.

## 3.13.    *Ex Vivo Validation of pH Imaging*

Two methods were used for *ex vivo* validation of MRI pH imaging. Use of a micro pH electrode

probe with a needle tip (ORION® Needle Tip Micro Combination pH Electrode, Thermo

Scientific) allowed for direct measurement of pH in the tumor, but with little spatial accuracy. A

fluorescent dye with pH sensitive response was used, SNARF-5F 5-(and-6-)-carboxylic acid

(Thermo Fischer).

### 3.13.1.    Tumor pH Imaging Using SNARF-5 Fluorescence

A SNARF compound, as described in **Section 2.7**, was used for *ex vivo* measurement of tumor

pH. With a $pK_a$ value of ~7.2, SNARF-5F 5-(and-6-)-carboxylic acid was chosen as the best

candidate for evaluation of tumor pH before and after normalization with sodium bicarbonate

therapy. The carboxylic acid derivative was chosen to determine extracellular pH to compare

with the MRI pH mapping and pH needle probe measurements. Imaging was done in a

multispectral fluorescence imaging system (Maestro, CRi). Solutions of SNARF, 1 µM, in pH

67

solutions ranging from 6.4 to 7.6, **Figure 36**, were imaged and showed significant shifts of fluorescence peak when excited at 523 nm, as seen in **Figure 37**. Using the Maestro software, images were unmixed based on the known pH of the solutions, producing an image showing the different pH solutions as different colors. Xenograft bearing mice with and without sodium bicarbonate pre-treatment were injected with SNARF-5F (0.25 μmol in 200 μL saline) and sacrificed 15 minutes later. Tumors were excised and sliced before imaging.
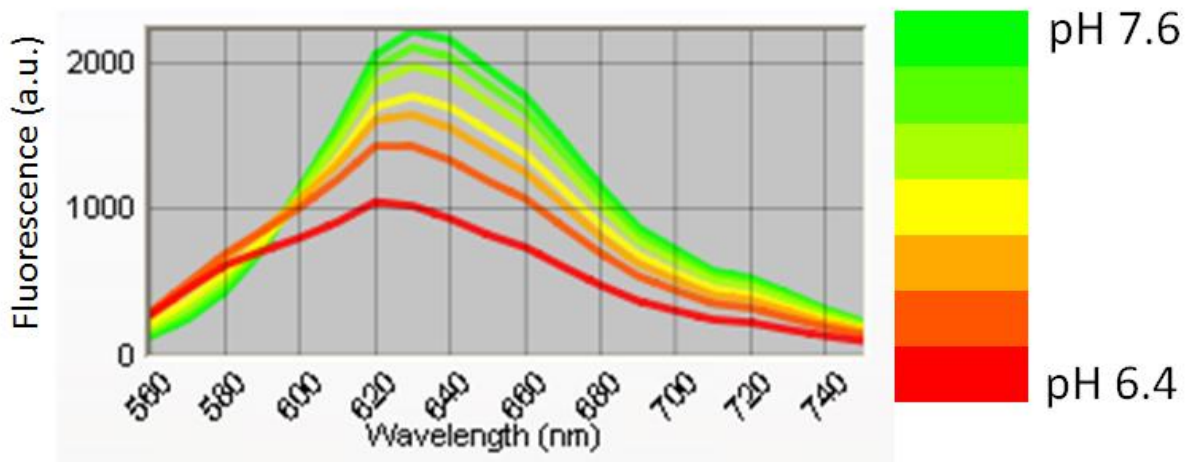


**Figure 36**: Fluorescence emission shifting in SNARF-5F in different pH solutions. 1 μM solutions of SNARF-5F buffered to pHs between 6.4 and 7.6 show significant shift in fluorescent peaks, increasing at 560 nm and decreasing at 630 nm as solutions become more acidic.
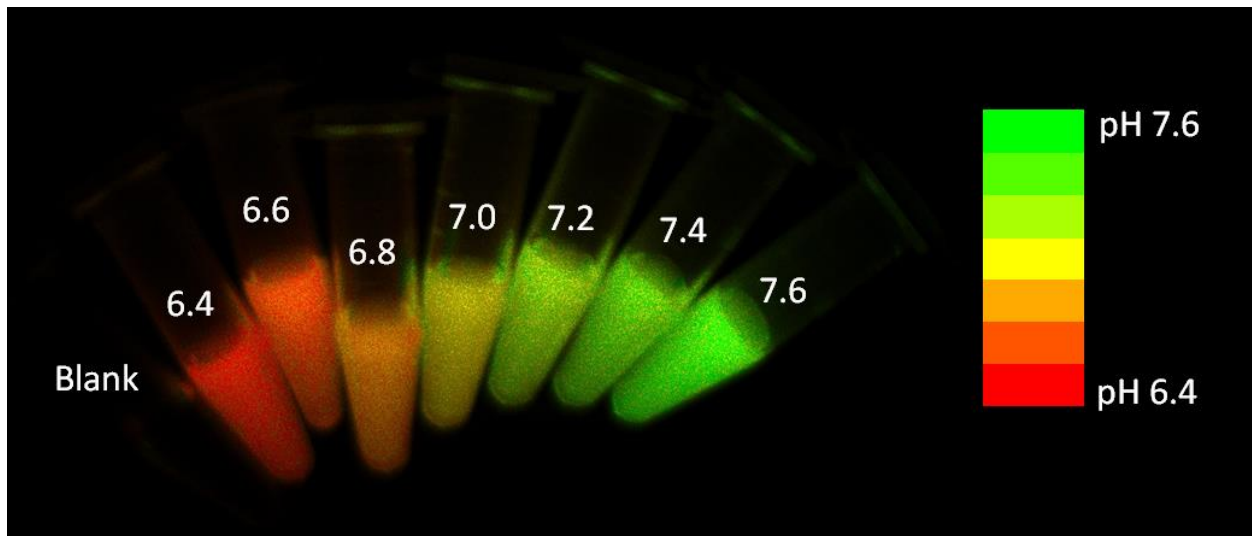


**Figure 37**: Solutions of SNARF-5F after unmixing of fluorescence. Using Maestro software's spectral unmixing, solutions of SNARF-5F with concentration ranging from 6.4 to 7.6 show up in their assigned color. This indicates SNARF-5F's excellent response in the pH range expected in tumors versus normal tissue.

### 3.14. Statistical Methods

Statistical analysis was performed using Student's t-test. A P value of <0.05 was considered statistically significant. Microsoft Excel software was used for all statistical analyses.

69

# 4. Chapter 4 – Results

## 4.1. CONP and [$^{89}$Zr ]CONP Reaction Yield and Physicochemical Properties

The synthetic and radiochemical yields as well as physicochemical properties of the various

CONPs and [$^{89}$Zr ]CONPs are presented in **Table 5** for review in this section.

| CONP Coating | CONP Yield (%) | [$^{89}$Zr ]CONP Yield (%) | CONP Hydrodynamic size (nm ± SD) | [$^{89}$Zr ]CONP Hydrodynamic size (nm ± SD) | CONP Zeta potential (mV ± SD) | [$^{89}$Zr ]CONP Zeta potential (mV ± SD) |
|---|---|---|---|---|---|---|
| Citrate/EDTA | 89.2% | 87.8% | 3.1 ± 0.5 | 3.1 ± 0.7 | -34.7 ± 0.9 | -33.0 ± 5.1 |
| DT10-NH$_2$ | 99+% | 93.0% | 6.3 ± 1.8 | 6.2 ± 1.6 | 17.3 ± 5.0 | 18.5 ± 5.7 |
| DT10-PEG | 99+% | 94.6% | 9.3 ± 2.7 | 9.4 ± 2.4 | 6.6 ± 5.0 | 7.3 ± 4.8 |
| DT10-SB | 99+% | 94.9% | 14.3 ± 4.6 | 14.2 ± 4.4 | -8.4 ± 0.6 | -13.7 ± 0.6 |
| PAA | 96.5% | 97.7% | 3.9 ± 0.9 | 3.8 ± 0.7 | -5.4 ± 1.3 | -5.3 ± 1.2 |
| Uncoated | 78.5% | 80.9% | 156.8 ± 35.4 | 163.3 ± 40.6 (90%) 1128 ± 342 (10%) | -23.2 ± 2.8 | -23.8 ± 10.0 |

**Table 5:** Reaction yields, hydrodynamic size, and zeta potential of the various CONPs and [$^{89}$Zr ]CONPs.

### 4.1.1. Reaction yield of Non-Radioactive CONPs

Synthesis of uncoated CONPs and CONPs with different coatings, as described in **Section 3.1.3**,

resulted in different yields, sizes, and surface charges. The reaction yields of coated CONPs were

70

all above 89% by measure of cerium content by ICP-OES. While the reaction yields of the DT10-based coated CONPs were all nearly 100%, the lower reaction yields of citrate and PAA coated CONPs were due to some of the nanoparticles passing through the MWCO filter due to smaller size of these nanoparticles, as detected by slight yellow color in the filtrate. Uncoated CONPs showed a lower reaction yield of 78.5% due to difficulty in recovering from the MWCO filter because of their insolubility.

## 4.1.2. Non-Radioactive synthesis of Zr-CONPs

ICP-OES results for incorporation of non-radioactive zirconium into CONPs are shown in **Table 6**. The reaction yields become much lower as the percent of zirconium in solution increases. However, during radiosynthesis, the amount of $^{89}$Zr in solution is trace, so the 96% incorporation at 0.5% was encouraging and indicated a likely high yield for radiosynthesis and warranted pursuit of radiosynthesis with $^{89}$Zr.

| Percent Zirconium in solution during CONP synthesis | Percent incorporated into CONPs |
|---|---|
| 0.5% | 96% |
| 1% | 63% |
| 5% | 42% |

**Table 6:** Incorporation of stable zirconium into CONPs. To determine if zirconium could be stably incorporated into CONPs, solutions of zirconyl chloride were added to the synthesis of DT10-CONP and incorporation was measured by ICP-OES as percent of original zirconium amount able to be detected in solution with CONPs.

### 4.1.3. Radiochemical Reaction Yield and Comparison of Physicochemical Properties of [$^{89}$Zr]CONPs to CONPs

Radiochemical reaction yields for the incorporation of $^{89}$Zr into CONPs were in good accordance with the non-radioactive yields, with slight reduction for the DT10-based coatings. Yield was greater than 80% for all coated and uncoated radiosynthesis, with >90% yield for most of the coated preparations, as seen in **Table 6**.

71

Non-radiolabeled and [$^{89}$Zr]CONPs' size and surface charge distribution were characterized by dynamic light scattering (DLS) and zeta potential (**Table 6**). The size of CONPs synthesized by co-precipitation was strongly dependent on the surface coating. Small carboxylate molecules and low molecular weight polymers, in the case of citrate and PAA, lead to smaller NPs at average of

3.1 and 3.8 nm, respectively. The high molecular weight hydroxyl DT10 polymers lead to larger CONP sizes, with their reactive functional groups also playing a role in the size, causing them to produce a size in the range of 6.2 to 14.3 nm. Without polymer or small molecule coating, the growth of the NPs is not limited by a coating and more NP aggregation occurs, as seen in the much larger size of uncoated CONPs at around 156 – 163 nm.[104] While uncoated CONP samples were sonicated before DLS measurement, aggregation into larger particles could still be detected in the uncoated [$^{89}$Zr]CONPs, showing their tendency to immediately aggregate in water solution.

The incorporation of $^{89}$Zr into the core of CONPs had very little effect on their size and charge. The DLS size profiles were almost identical for the non-radiolabeled CONPs and [$^{89}$Zr]CONPs, as seen in **Table 6** and **Figure 38**. Uncoated non-radiolabeled and [$^{89}$Zr]CONPs showed similar size except for 10% aggregation at ~1.1 μm for the uncoated [$^{89}$Zr]CONPs. The surface charges, measured as zeta potential, were also very similar across the uncoated and coated CONPs and [$^{89}$Zr]CONPs, as seen in **Table 6**. These results indicate not only that $^{89}$Zr incorporation has negligible effect on CONP synthesis, but that different batches made under the same conditions have the same physicochemical properties, an important aspect for a reproducible standardized synthesis.
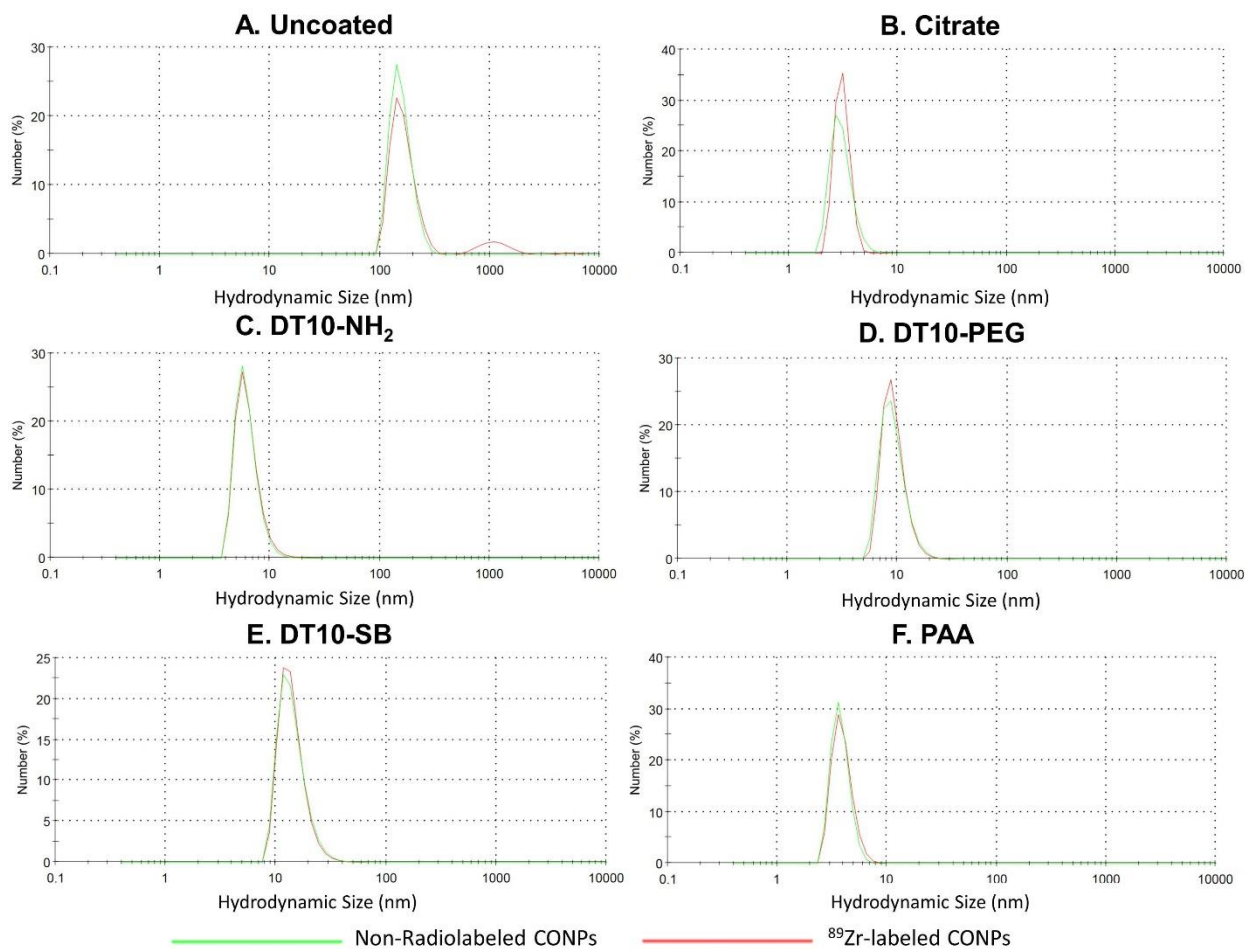
**Figure 38**: DLS measurement of the various coated and uncoated CONPs and [$^{89}$Zr]CONPs. Size distribution of the CONPs is reported in terms of number (%), where the y-axis represents percent of total particles that were detected at that size. All CONPs and [$^{89}$Zr]CONPs show almost the same distribution of sizes, indicating no effect of $^{89}$Zr incorporation on size.

## 4.1.    Stability Studies

Stability studies were done to determine how stably $^{89}$Zr was incorporated into the core of

CONPs to ensure that radioactive signal represents the nanoparticles. Several methods were

used, including radioactive instant thin layer chromatography (Radio-ITLC), and ultraviolet-

(UV-) and radioactive HPLC detection of CONP and $^{89}$Zr signal, respectively.

## 4.1.1. Desferoxamine (DFO) Challenge of [$^{89}$Zr]CONPs

A desferoxamine (DFO) challenge and molecular weight cut off (MWCO) method was used to

determine $^{89}$Zr incorporation into and stability of coated and uncoated [$^{89}$Zr]CONPs, as seen in

**Figure 39**. While these results show a significant loss in activity for citrate and DT10-NH$_2$

coated CONPs after 24 hours of incubation with DFO, all other coatings show $\geq$ 80% retention

of activity after 24 hours, indicating good stability of $^{89}$Zr in the nanoparticle. The loss of activity

can be attributed to the harshness of the chelation test that does not reflect conditions in the body.

Higher loss of activity by citrate and DT10-NH$_2$ coated [$^{89}$Zr]CONPs may be due to chelation of

$^{89}$Zr to the surface coating, which is more easily removed by DFO, especially in the case of

citrate coated [$^{89}$Zr]CONPs due to EDTA, another chelator, used in the surface coating. These

values are also consistent with other studies that use desferoxamine (DFO) as a chelating agent

and show decrease in RCP by as much as 55% when challenged with

diethylenetriaminepentaacetic acid (DTPA).[105]
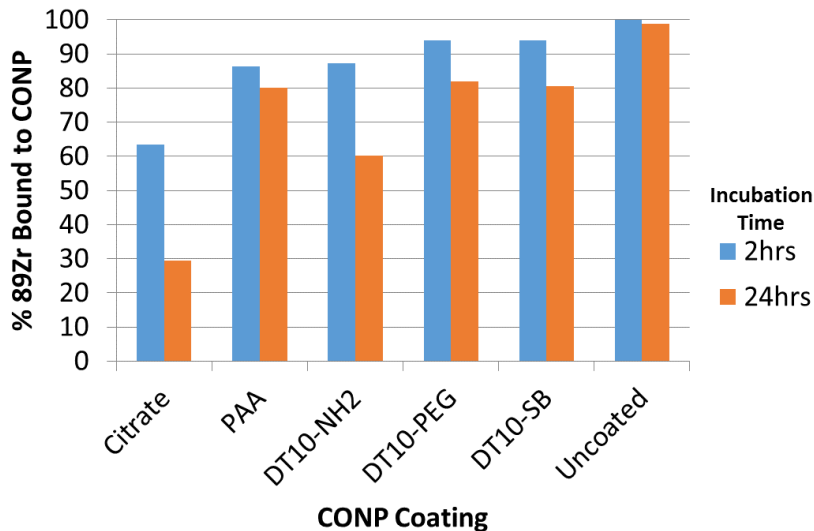


**Figure 39:** [$^{89}$Zr]CONP Stability – Desferoxamine (DFO) Challenge. DFO, a strong chelator, was incubated with the various coated and uncoated [$^{89}$Zr]CONPs using a molecular wright cutoff (MWCO) method by which >95% of $^{89}$Zr bound to DFO passes through the filter, while $^{89}$Zr labeled CONPs are retained. Results show that $^{89}$Zr was successfully incorporated into the core of CONPs, with some coatings showing less stability, notably citrate and DT10-NH$_2$ coated [$^{89}$Zr]CONPs.

## 4.1.2. Radio- and UV-HPLC of [$^{89}$Zr ]CONPs

A radio- and UV-HPLC method was used to determine the coincidence of signal from CONPs and $^{89}$Zr. Free $^{89}$Zr as $^{89}$ZrCl$_2$ does not elute through the column, so analysis of RCP could not be done by this method. However, HPLC results did show that the radioactive signal detected matched exactly with the UV signal of CONPs (254 nm), demonstrating the proof of concept that radioactive signal represents the nanoparticle location, as seen in **Figure 40**. *In vivo* stability of [$^{89}$Zr ]CONPs was also demonstrated by analyzing blood samples at 2 hours post i.v. injection, seen in **Figure 41**, and showing the same coincidence of UV and radioactive signal and validating *in vivo* signal detection representing CONP distribution.
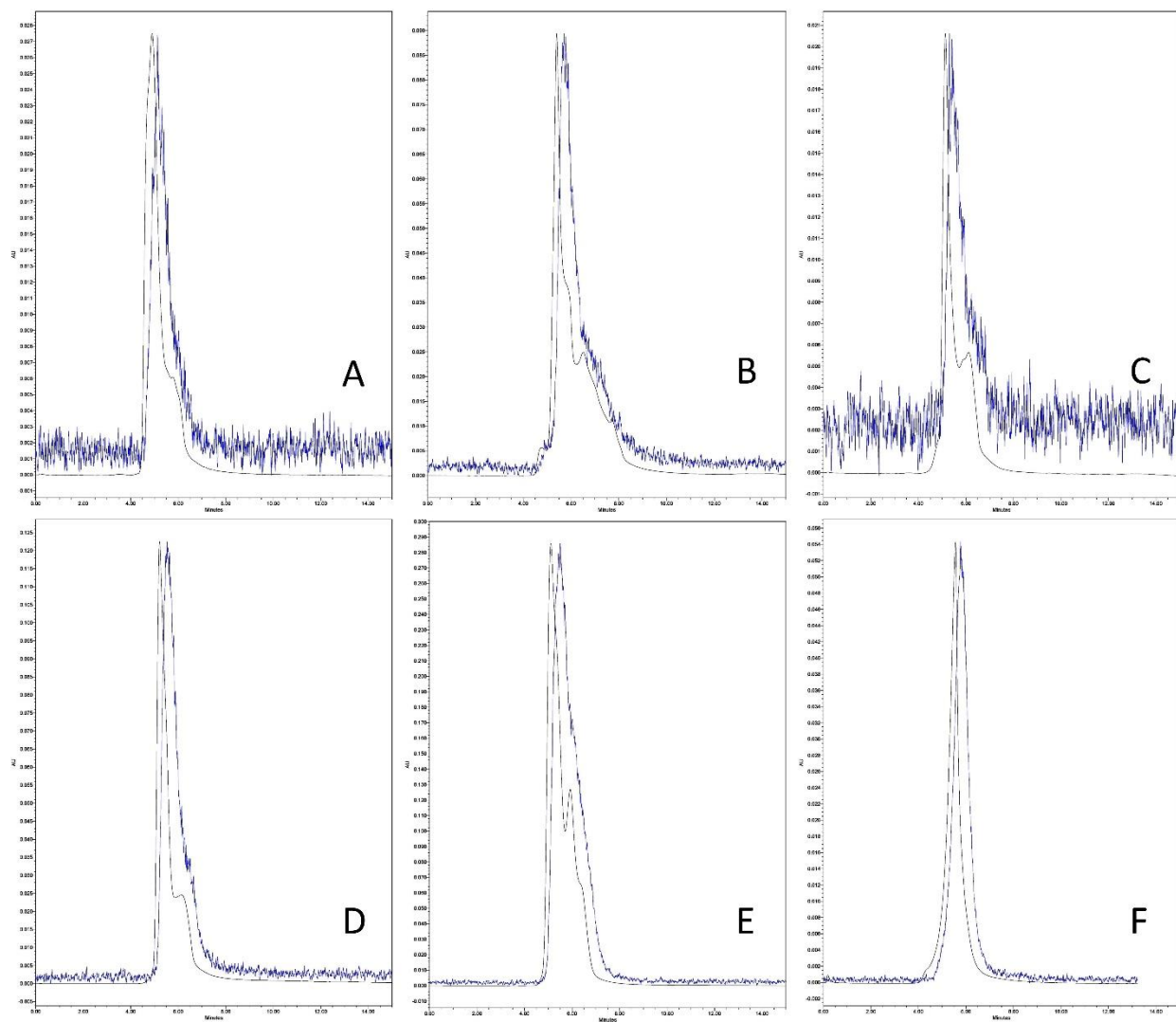
**Figure 40**: HPLC UV and radioactivity retention times of [89Zr]CONPs. Uncoated (A) [$^{89}$Zr]CONPs and citrate (B), DT10-NH$_2$ (C), DT10-PEG (D), DT10-SB (E) and PAA (F) coated [$^{89}$Zr]CONPs were injected into HPLC and detected by UV (254nm) of CONP and radioactivity of $^{89}$Zr.
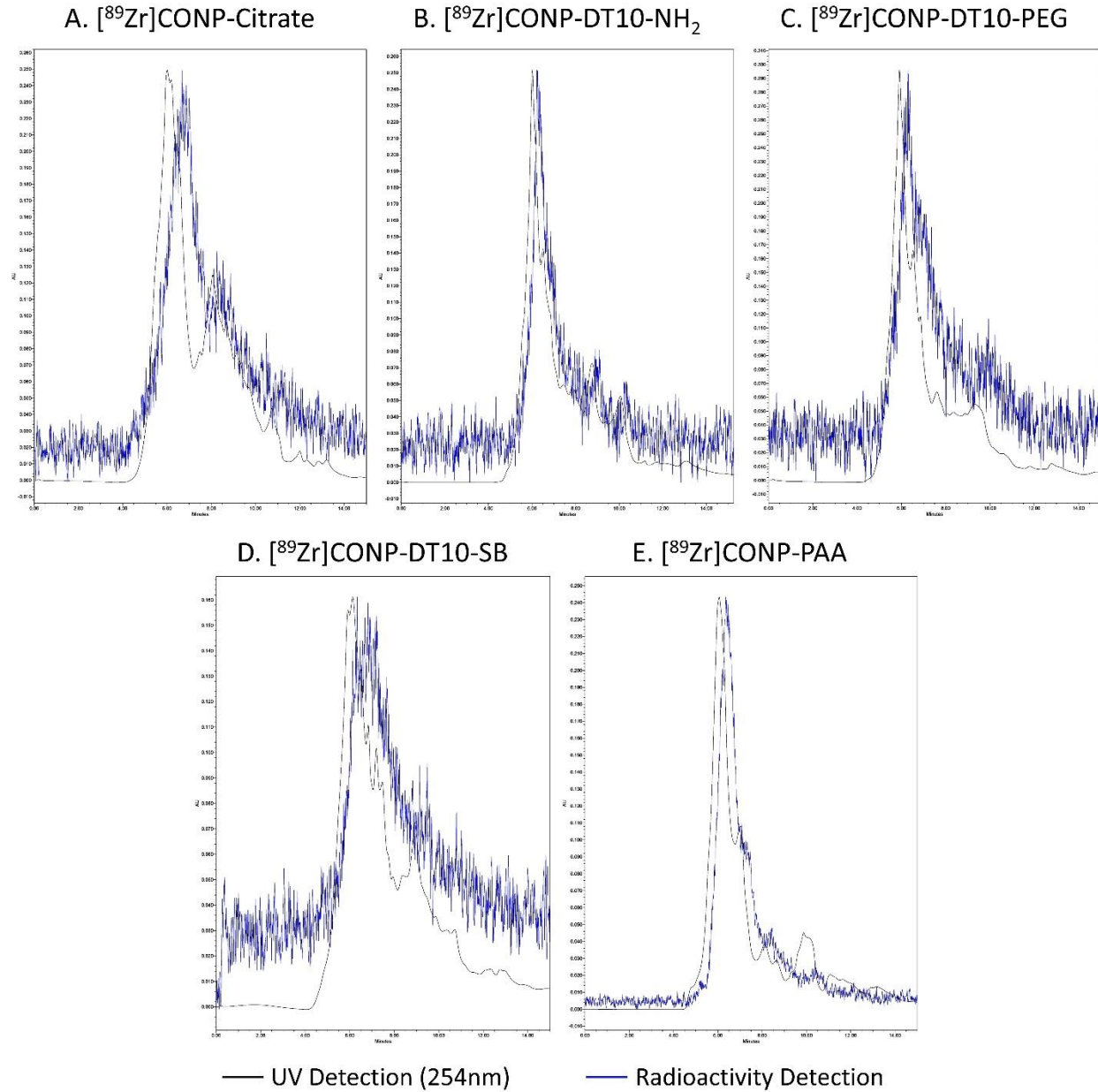
**Figure 41**: HPLC UV and radioactivity retention times for 2 hour plasma samples from mice i.v. injected with [$^{89}$Zr]CONPs. Citrate (A), DT10-NH2 (B), DT10-PEG (C), DT10-SB (D) and PAA (E) coated [$^{89}$Zr]CONPs were i.v. injected into C57B/6 mice and plasma samples were taken at 2 hours. Plasma samples were injected into HPLC and detected by UV (254nm) of CONP and radioactivity of 89Zr. The plasma sample from the mouse injected with uncoated [$^{89}$Zr]CONPs did not have enough radioactivity for detection.

## 4.2.     *Autocatalytic Activity of CONPs and [$^{89}$Zr]CONPs*

In order to determine that the various coated CONPs and [$^{89}$Zr]CONPs retain redox cycling

ability, and autocatalytic assay was done with $H_2O_2$. The autocatalytic properties of CONPs are

measured in a reaction in $H_2O_2$ as the color change of CONPs reflects their change in oxidation

state, recorded as absorbance at 420 nm by a well plate reader. CONPs react quickly with $H_2O_2$

and gradually return to their original oxidation state over the course of a few days, which was not

affected by the coating of CONPs, as seen in **Figure 42**, and even shows that the uncoated

CONPs did not return to baseline as effectively as the coated CONPs. As previously reported,

the reduction process of intrinsically radiolabeled CONP was observed to be faster than the non-

radiolabeled CONPs which reflects the improved recycling of radioisotope-doped CONPs.[52] The
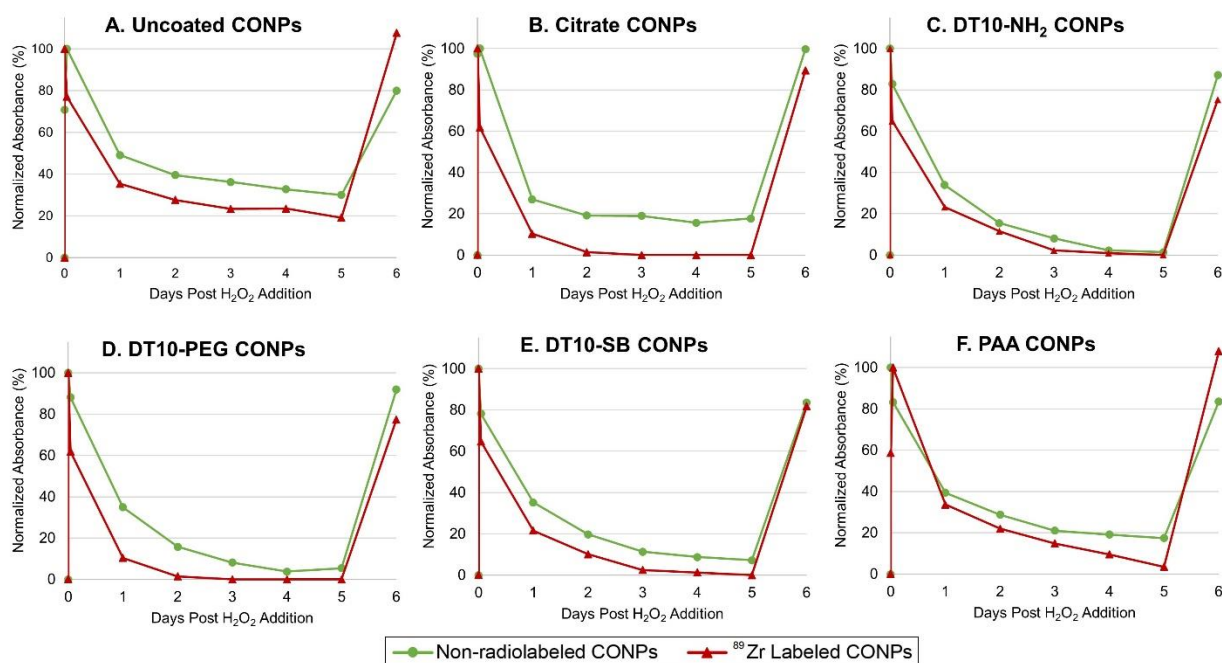


**Figure 42**: CONPs' and [$^{89}$Zr]CONPs' cycling redox reaction with $H_2O_2$. $H_2O_2$ was added to 0.5 mg/mL solutions of non-radiolabeled and $^{89}$Zr labeled uncoated CONPs (A) and citrate (B), DT10-NH$_2$ (C), DT10-PEG (D), DT10-SB (E) and PAA (F) coated CONPs and [$^{89}$Zr]CONPs. Absorbance was monitored at 420 nm to test for their ability to reduce $H_2O_2$. Absorbance was normalized to initial solution absorbance (0%) and to highest absorbance after reaction (100%) and was monitored over 5 days. Zero percent corresponds to CONPs being primed for radical scavenging, whilst 100% represents CONPs being fully oxidized. Initial measurements were taken before $H_2O_2$ addition, immediately after and 1 hour after addition. On day 6, $H_2O_2$ was again added to demonstrate true redox cycling with increased absorbance similar to initial reaction. (Mean ± SEM, n=3)

reason for the apparent improvement in redox reaction cycling of intrinsically radiolabeled CONPs is interesting and could possibly be due energy absorption, emitted from the radioisotope. This could be a means by which to increase the rate of conversion of $Ce^{4+}$ to $Ce^{3+}$ within radiolabeled CONP and increase redox reaction capacity. Interestingly, the same phenomenon was observed when the CONPs were exposed to UV light, reducing the time for recovery from days to hours, further supporting the theory that absorbing forms of electromagnetic energy affect their redox properties. **Figure 42** also shows that $H_2O_2$ was added again at day 6 to ensure the ability to repeatedly perform redox reactions. All coated and uncoated CONPs showed true redox cycling with similar shifts in absorbance compared to the first addition of $H_2O_2$.

### 4.2.1. pH Dependent Autocatalytic Activity

To determine if pH could affect the reaction of CONPs with $H_2O_2$, the autocatalytic reaction was repeated with PAA-CONP in buffered solutions of 6.6, 7.0, and 7.4, as seen in **Figure 43**. PAA-CONP showed a slight decrease in reaction with $H_2O_2$ at pH 7.0, though not significant (142% vs 130%, p = 0.064). At pH 6.6 PAA-CONP showed a signification 49% decrease in reaction with $H_2O_2$ (142% vs 72%, p < 0.0001). This shows that CONPs have a reduced ability to act as an antioxidant with a very small shift towards acidic pH, indicating a possible mechanism by which they are unable to protect cancerous tissue due to the acidity of the tumor microenvironment.

79
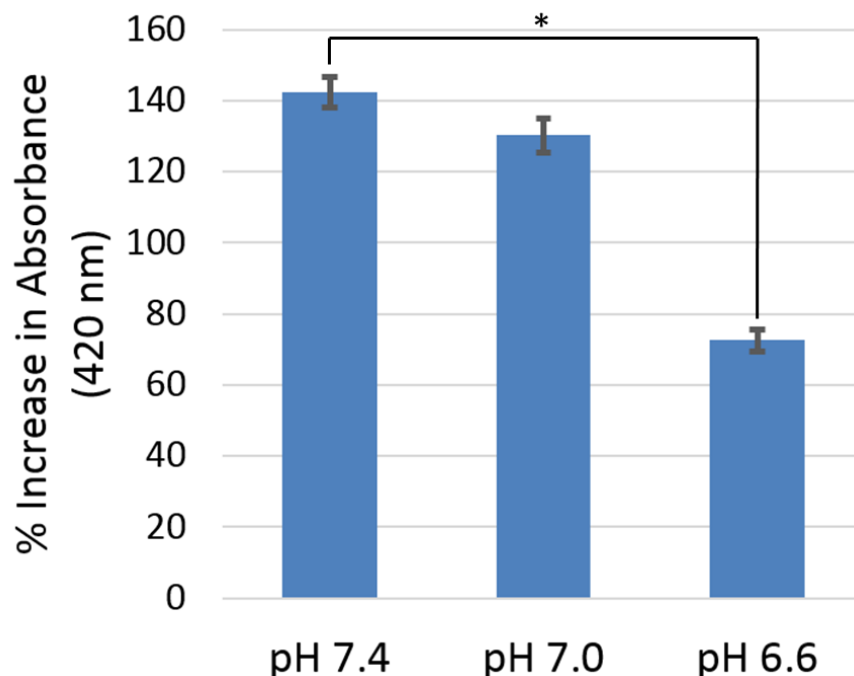
**Figure 43**: PAA-CONPs' pH dependent redox reaction with $H_2O_2$. $H_2O_2$ was added to 0.5mg/mL solutions of PAA-CONP, buffered to pHs of 7.4, 7.0, and 6.6. The initial increase is absorbance, monitored at 420 nm, was measured, indicating the change in oxidation state of surface cerium from $Ce^{3+}$ to $Ce^{4+}$. Compared to PAA-CONPs at pH 7.4, at pH 7.0 they showed a small but not significant decrease in reaction (142% vs 130%, p = 0.064), while at 6.6 they showed a significant decrease (142% vs 72%, **\*** p < 0.0001), indicating a strong effect of pH on redox ability, decreasing as pH decreases. (Mean ± SEM, n=6)

## 4.3. Cell Viability of COLO-205 and HCT-116 with Increasing Concentrations of CONPs and [$^{89}$Zr]CONPs

The toxicity of CONPs and radiolabeled CONPs has been shown to be very low *in vitro*.[52,70] To ensure that toxicity was not increased by $^{89}$Zr, [$^{89}$Zr]CONPs were incubated in increasing concentrations with two cell lines and viability was determined following 24hr incubation, seen in Figure **44**. For a decrease greater than 5%, toxicity in COLO-205 colon cancer cells was only seen with [$^{89}$Zr]CONP-PAA at the highest concentration of 120ug/mL, while in HCT-116 colon cancer cells only the [$^{89}$Zr]CONP-citrate and [$^{89}$Zr]CONP-PAA showed toxicity, again only at the highest concentration. None of the other coatings showed toxicity over 5% in these cell lines up to the highest [$^{89}$Zr]CONP concentration tested.

80

## A. COLO205 Cells

## B. HCT-116 Cells

Legend: ■ 1 µg/mL    ■ 10 µg/mL    ■ 40 µg/mL    ■ 80 µg/mL    ■ 120 µg/mL
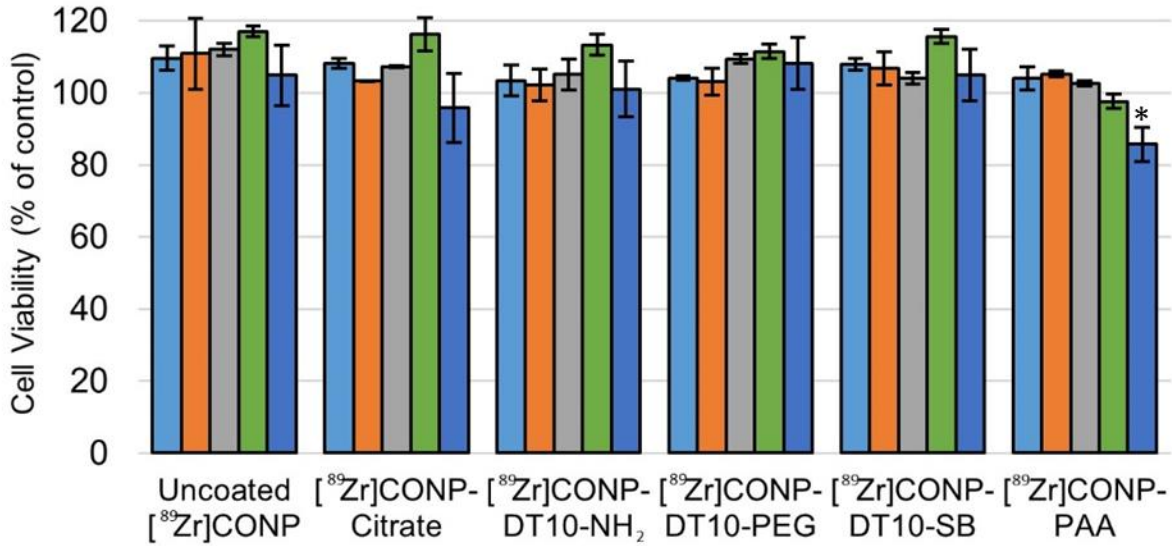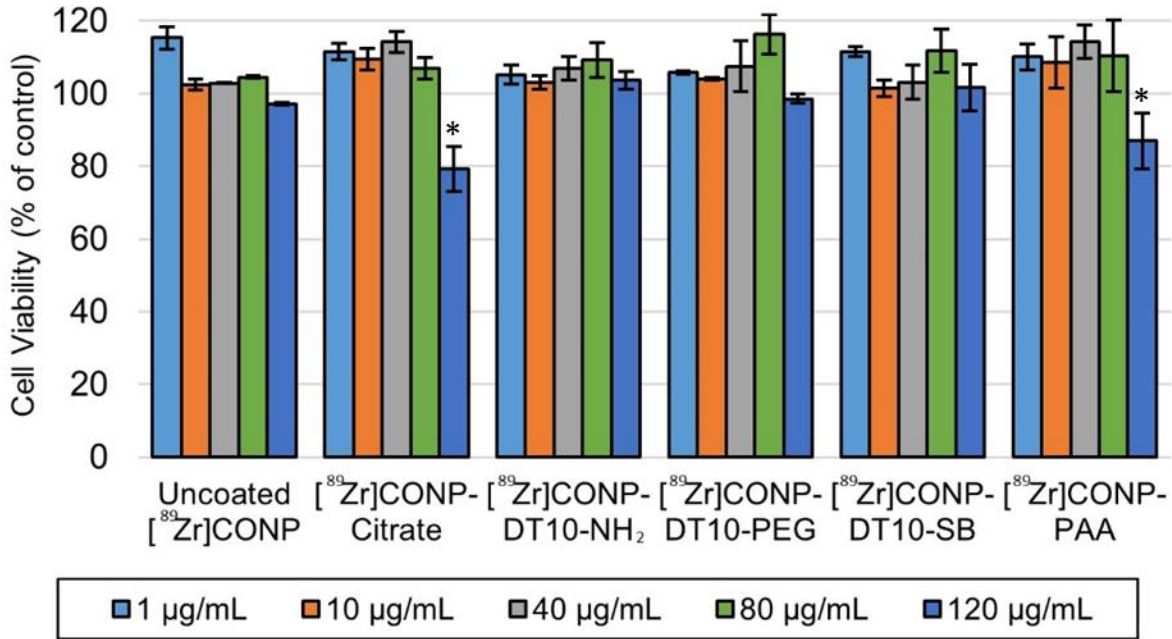
**Figure 44**: [$^{89}$Zr]CONPs' effect on cell viability. [$^{89}$Zr]CONPs were incubated in increasing concentrations from 1 to 120 µg/mL in two colon cancer cell lines, COLO-205 (A) and HCT-116 (B), and cell viability measured using Cell Titer-Glo Assay. Only citrate (HCT-116) and PAA (COLO-205 and HCT-116) coated CONPs showed significant toxicity, and only at the highest concentration tested of 120 µg/mL (Mean ± SEM, n=3, * p < 0.05)

81

## 4.4.    Comparison of Uptake of Coated and Uncoated [⁸⁹Zr]CONPs in COLO-205 and HCT-116 in Different pH Media

Uptake of PAA-[⁸⁹Zr]CONPs in COLO-205 and HCT-116 cells was seen to be altered by the pH of the growth media in an inconsistent manner when comparing the two cell lines, seen in **Figure 45**. For COLO-205, uptake was similar at pH 7.4 and 7.0 (p = 0.343), but decreased significantly by 89% at pH 6.6 (p = 0.0006). For uptake of PAA-[⁸⁹Zr]CONPs in HCT-116 cells, uptake was seen to decrease significantly by 23% in pH 7.0 media compared to pH 7.4 media (p = 0.012). However, at pH 6.6 the uptake increase by 40% compared to pH 7.4 (p = 0.008).
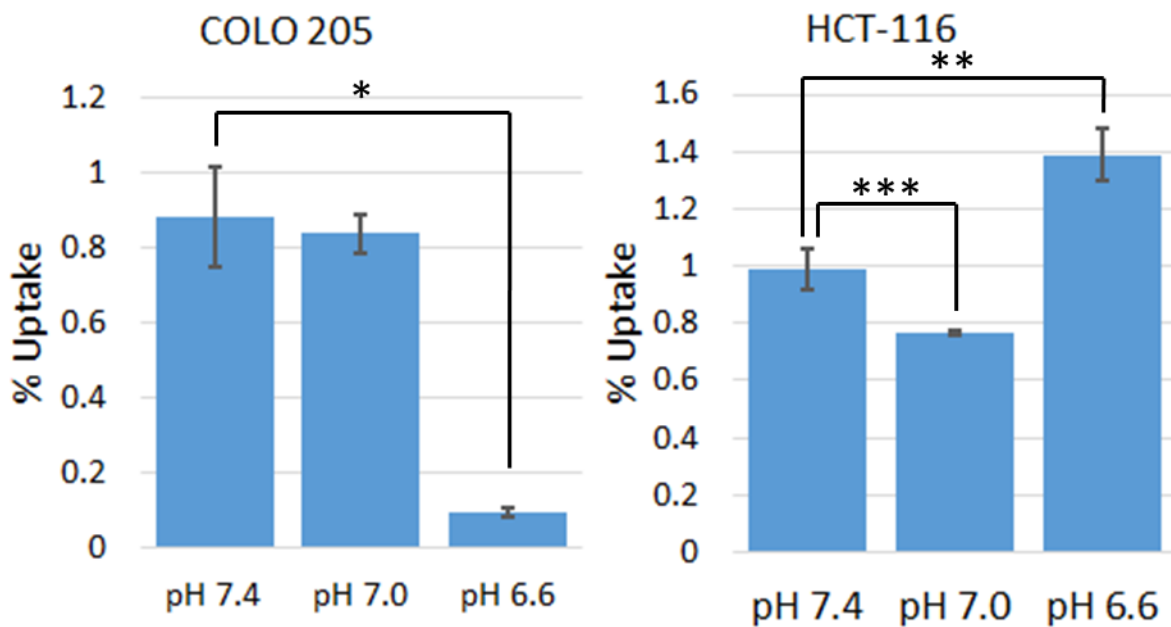


**Figure 45**: Uptake of PAA-[⁸⁹Zr]CONPs in COLO-205 and HCT-116 cells. Uptake of PAA-[⁸⁹Zr]CONPs was significantly decreased at pH 6.6 in COLO-205 cells, compared to pH 7.0 and 7.4 (* p = 0.0006). However, uptake changes were not consistent across cell lines, with HCT-116 cells showing decreased uptake a pH 7.0 (** p = 0.012), and increased uptake at pH 6.6 (*** p = 0.008) when compared to pH7.4. (Mean ± SEM, n=3)

## 4.5. pH Dependent Radioprotection of CONPs in HCT-116 cells

Clonogenic assay results for HCT-116 cells irradiated or treated with CONPs before irradiation in pHs of 7.4 and 7.0 showed a marginal difference in radioprotection, seen in **Figure 46**. PAA-CONP pre-treatment before irradiation for cells in pH 7.4 media showed a slight increase in % plating efficiency compared to cells only irradiated, though not significant (15% vs 13.1%, p = 0.068). Pre-treatment with PAA-CONPs before irradiation in pH 7.0 media showed no change in % plating efficiency, indicating no protection of cancer cells from radiation at pH 7.0 (2.0% vs 2.2%, p = 0.333). This study warranted an *in vivo* examination of whether normalization of the pH microenvironment in tumor would cause CONPs to have radioprotection that is absent at lower pH.
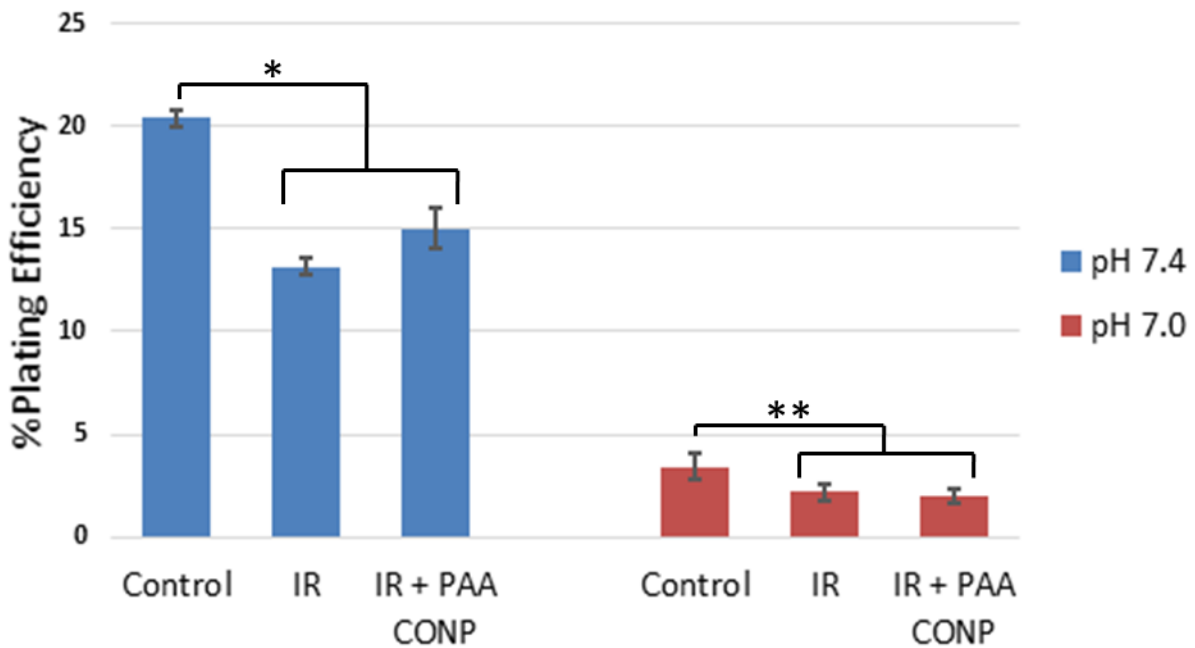


**Figure 46**: Change in % plating efficiency of irradiated HCT-116 cells when incubated with PAA-CONP and in different pH media. Clonogenic assay of HCT-116 cells irradiated with 5 Gray in pH 7.4 media showed an increase in % plating efficiency when incubated with PAA-CONP when compared to cells only irradiated, though not significant (p = 0.068). When incubated in pH 7.0 media, there was no difference in % plating efficiency when comparing cells irradiated with PAA-CONP versus irradiated alone (p = 0.333). (Mean ± SEM, n=3, * p < 0.01, ** p < 0.05)

## 4.6. Clonogenic Assay of PAA-CONP Treated and Irradiated Xenograft Tumors

Control and PAA-CONP pretreated mice with HCT-116 xenograft tumors given whole body

dose of 10 Gray had their tumors removed and plated for clonogenic measurement in comparison

to control and PAA-CONP only treated mice. PAA-CONP alone showed no effect on % plating

efficiency compared to control (p = 0.10), but both irradiated and PAA-CONP treated and

irradiated tumors showed significant decrease in % plating efficiency (p < 0.00001), as seen in

**Figure 47**. Further, PAA-CONP pre-treatment showed enhanced killing of tumor, with a

significant decrease in % plating efficiency compared to radiation alone (p < 0.00001). This

indicates possible radiosensitization where CONPs may enhance the killing effects of radiation

in tumor, as also seen in previous research (**Figure 9**).[9]
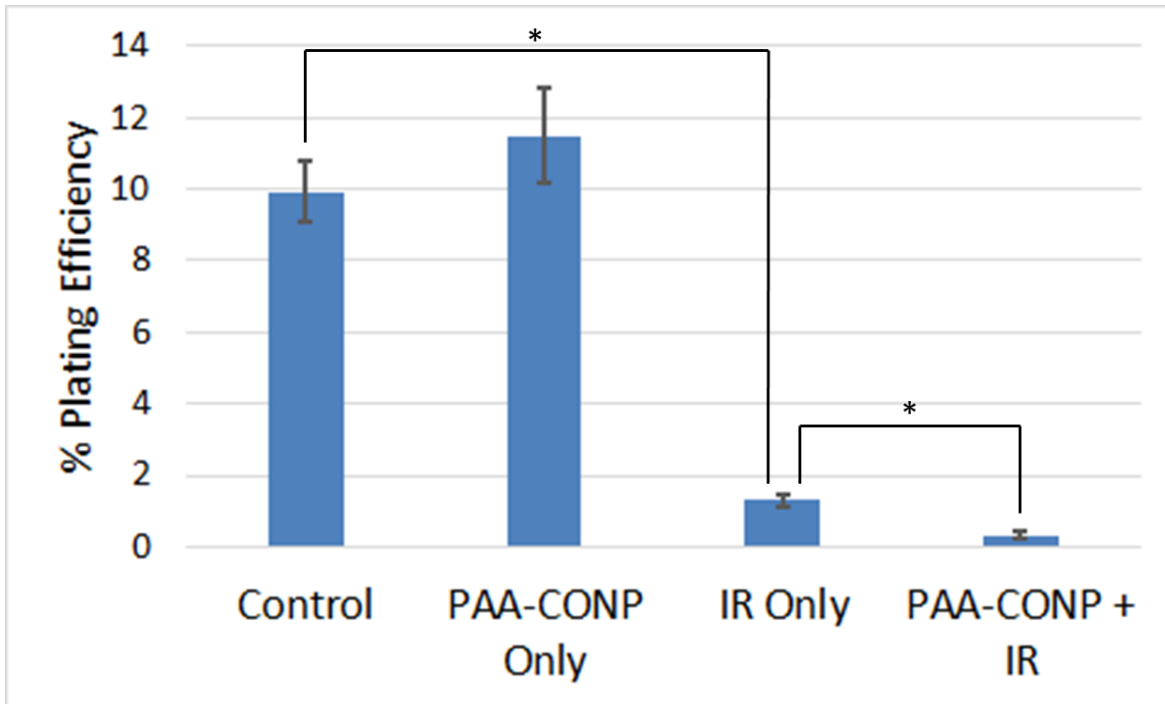


**Figure 47**: Change in % plating efficiency of irradiated xenograft HCT-116 tumors when administered PAA-CONP.
Clonogenic assay of HCT-116 xenograft tumors irradiated with 10 Gray showed a significant decrease in % plating
efficiency both when pre-treated with PAA-CONPs and with radiation alone as compared to control tumors (both p
< 0.00001). PAA-CONP treatment alone showed no effect on % plating efficiency compared to control (p = 0.10).
Compared to tumors only irradiated, PAA-CONP treated irradiated tumors showed further decrease in % plating
efficiency (p < 0.00001). This may indicate a radiosensitization by CONPs. (Mean ± SEM, n=6, * p < .00001)

## 4.7. *Biodistribution*

Biodistribution results are given in terms of *ex vivo* gamma counts of major organs and images and video of PET imaging of uncoated and coated [$^{89}$Zr]CONPs. $^{89}$ZrCl$_2$ was also examined to ensure results were not due solely to $^{89}$Zr signal separated from the nanoparticles.

### 4.7.1. *Ex Vivo* Gamma Counting Results

*Ex vivo* biodistribution for all uncoated and coated [$^{89}$Zr]CONPs at 2 and 24 hours is shown in **Figure 48**. The general PET imaging profiles of the coated and uncoated CONPs is in accordance with the ex vivo biodistribution data. Both imaging and ex vivo analysis showed the majority of the uncoated [$^{89}$Zr]CONPs in the lung, with elevated uptake in the liver and spleen. The coated [$^{89}$Zr]CONPs showed a much more general distribution to most organs, with uptake in the liver and spleen, with preferential kidney uptake for citrate and PAA coated [$^{89}$Zr]CONPs. Comparing uptake in the liver and spleen at 24 hours, [$^{89}$Zr]CONP-PAA showed the least uptake (**Figure 49A&B**). [$^{89}$Zr]CONPs' also show significant 24 hour uptake in the gallbladder and feces, indicating hepatobiliary excretion, with [$^{89}$Zr]CONP-DT10-SB showing particularly high excretion by this method (**Figure 49C&D**).

**Figure 50** compares the uptake of [$^{89}$Zr]CONPs in several major organs and tumor. Uncoated [$^{89}$Zr]CONPs show highest uptake in the lungs and heart, but the least in every other organ. Among the coated [$^{89}$Zr]CONPs, PAA shows the most consistent high uptake in all organs. [$^{89}$Zr]CONP-citrate and [$^{89}$Zr]CONP-PEG show highest uptake in tumors.
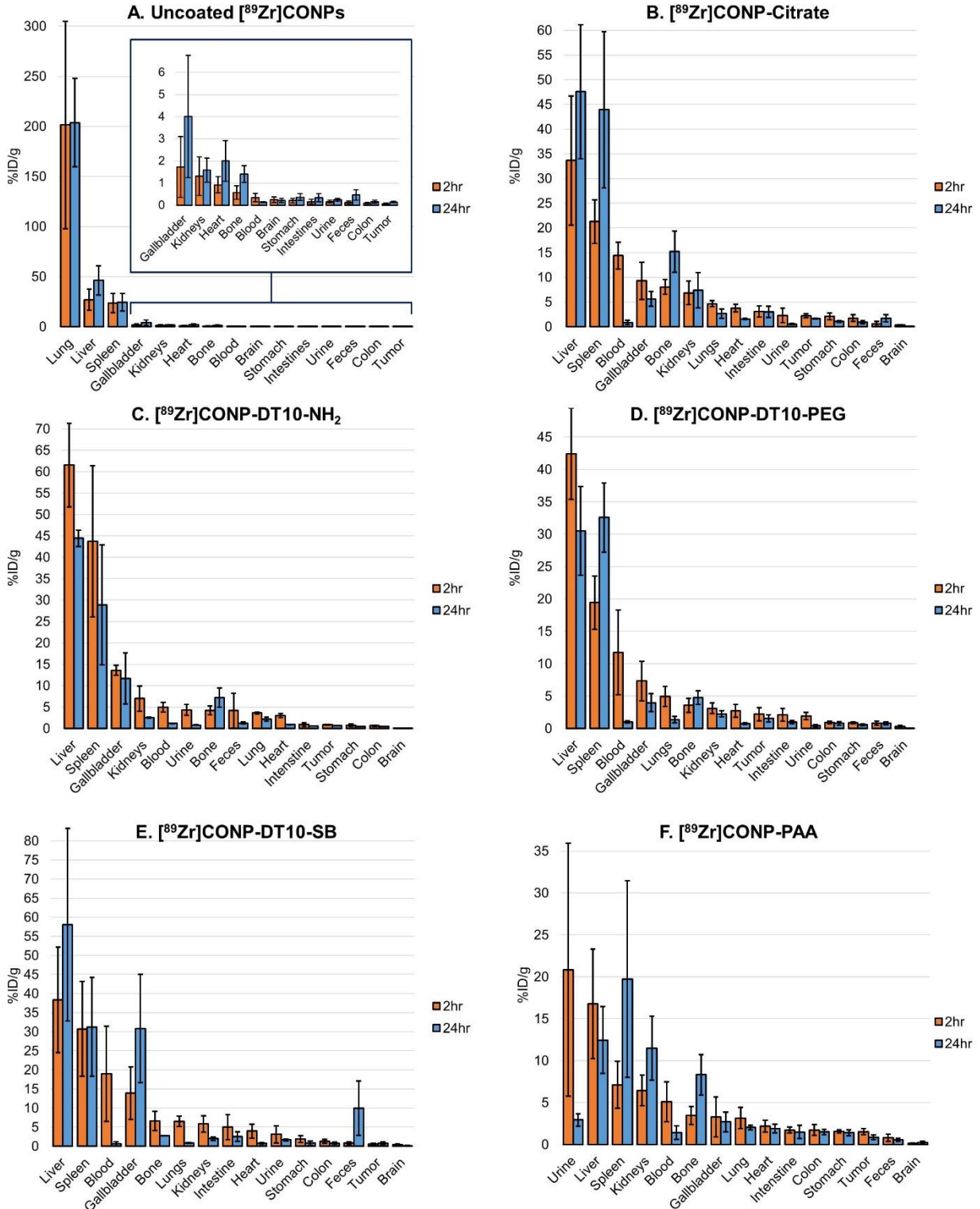
**Figure 48**: Uptake of [$^{89}$Zr]CONPs in all excised tissues. Mice tail vein injected with uncoated [$^{89}$Zr]CONP (A), [$^{89}$Zr]CONP-Citrate (B), [$^{89}$Zr]CONP-DT10-NH$_2$(C), [$^{89}$Zr]CONP-DT10-PEG (D), [$^{89}$Zr]CONP-DT-SB (E) and [$^{89}$Zr]CONP-PAA (F) were sacrificed at 2 and 24 hours post-injection and tissues were weighed and gamma counted and percent injected dose per gram (%ID/g) was determined. Organs are presented in order of highest to lowest uptake (at 2 hours), from left to right. (Mean ± SEM, n=3-6)
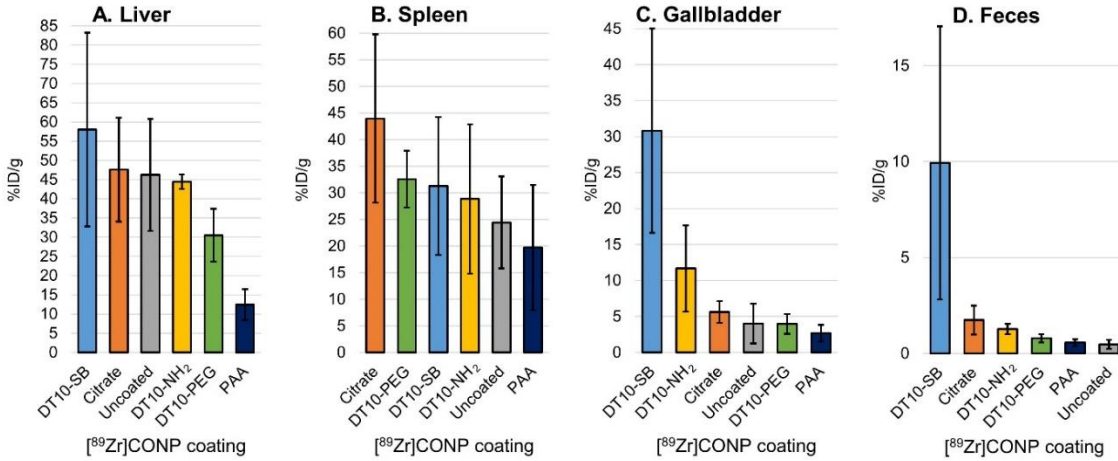
**Figure 49**: [$^{89}$Zr]CONPs' reticuloendothelial uptake and hepatobiliary clearance at 24 hours. Uptake in the organs of the reticuloendothelial system, liver (A) and spleen (B), at 24 hours is compared as a function of [$^{89}$Zr]CONP coating. Hepatobiliary clearance through the gallbladder (C) and feces (D) at 24 hours is also compared. Uptake is presented in order of highest to lowest uptake, from left to right. (Mean ± SEM, n=3-6)
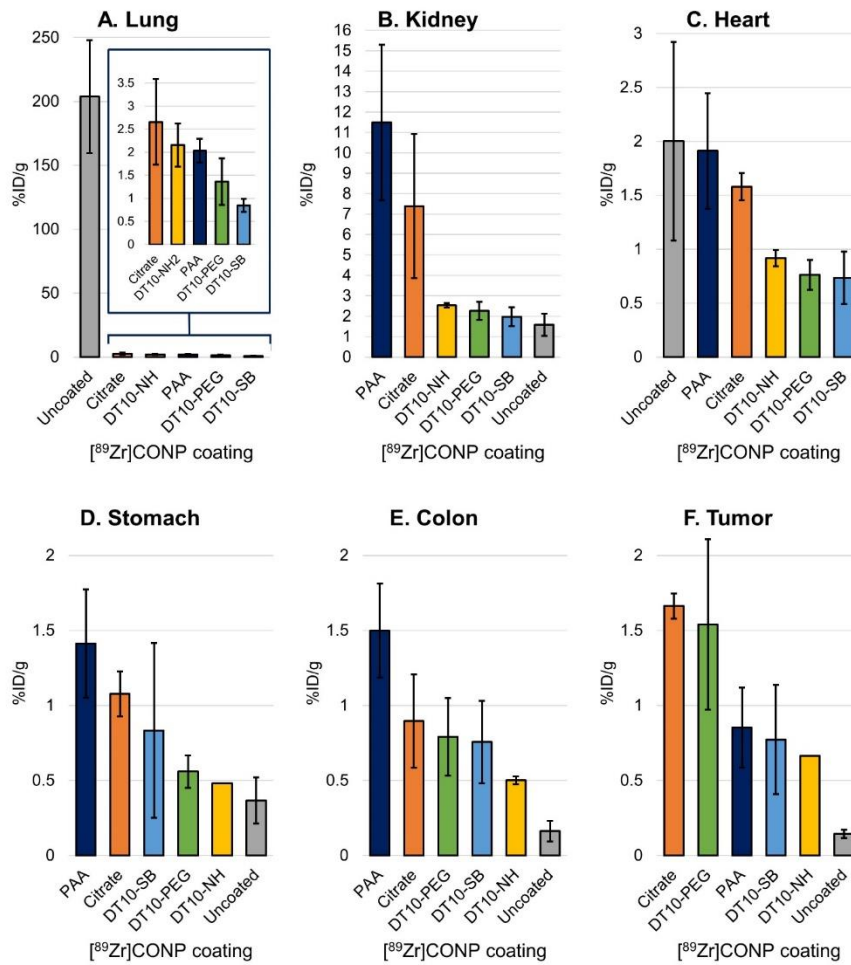


**Figure 50**: Comparative uptake of [$^{89}$Zr]CONPs in major organs and tumor at 24 hours. Uptake in the lungs (A), kidney (B), heart (C), stomach (D), colon (E) and tumor (F) at 24 hours is compared as a function of [$^{89}$Zr]CONP coating. Uptake is presented in order of highest to lowest uptake, from left to right. (Mean ± SEM, n=3-6)

87

## 4.7.2. Whole Body Activity of Mice Injected with [$^{89}$Zr]CONPs

Whole body radioactivity of C57BL/6 mice injected with the various coated and uncoated [$^{89}$Zr]CONPs showed high retention in all but PAA-[$^{89}$Zr]CONPs, as seen in **Figure 51**. This is likely due to the high uptake in the reticuloendothelial system and very slow excretion through the feces. However, PAA-[$^{89}$Zr]CONPs' show excellent pharmacokinetics with high renal clearance of 75% between 2 and 4 hours. More importantly, this clearance does seem to affect the uptake of PAA-[$^{89}$Zr]CONPs in other tissues, where it can be seen to be taken up as much or more than all the other coated and uncoated [$^{89}$Zr]CONPs in most tissues.
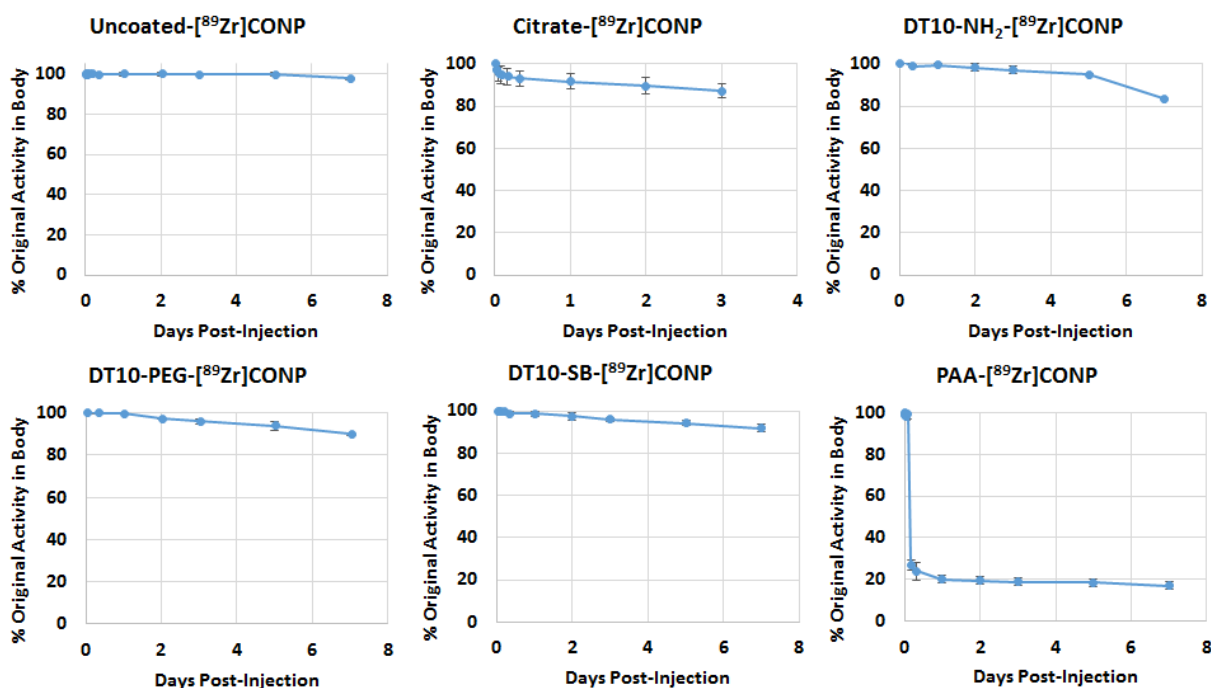


**Figure 51**: Excretion of [$^{89}$Zr]CONPs over the course of one week. High doses of the various coated and uncoated [$^{89}$Zr]CONPs were i.v. injected into C57BL/6 mice and total body radioactivity was monitored over the course of one week. All coated and uncoated [$^{89}$Zr]CONPs except PAA-[$^{89}$Zr]CONPs showed high retention of activity, indicating little excretion of the nanoparticles. However, PAA-[$^{89}$Zr]CONPs showed a 75% reduction in activity between 2 and 4 hours, likely all in the urine according to PET imaging and *ex vivo* biodistribution data. During the course of the experiment, all mice injected with citrate[$^{89}$Zr]CONPs died on day 3, and two mice injected with DT10-NH$_2$-[$^{89}$Zr]CONPs died on day 3 and 5, indicating toxicity at the high dose (~40 mg/kg) given. All other mice showed good tolerance of the high dose. (Mean ± SEM, n=3)

### 4.7.3. *In Vivo* PET-CT Imaging of [$^{89}$Zr]CONPs

PET-CT dynamic scans were done for each type of [$^{89}$Zr]CONP, which images the distribution of the nanoparticles during the first hour after injection. Videos of each [$^{89}$Zr]CONP dynamic scan can be found in the **Supplementary Video Section.** Maximum intensity projections of the dynamic scans at times between 1 and 60 minutes, after injection, are presented in **Figure 52**. The majority of the activity of the uncoated [$^{89}$Zr]CONPs immediately shows in the lungs. Over the next hour, uptake of the uncoated [$^{89}$Zr]CONPs increases in the liver and spleen, which indicates uptake by the reticuloendothelial system (RES) through phagocytosis, commonly to NP biodistribution.[36,37] Unlike uncoated [$^{89}$Zr]CONPs, all of the coated [$^{89}$Zr]CONPs showed blood flow driven distribution at least for the first minute. Liver and spleen uptake are also seen across all of the coated [$^{89}$Zr]CONPs. Among the coatings, the PAA and citrate were unique due to their ability to be cleared by the kidneys into the urine. This clearance was apparent within the first minute for [$^{89}$Zr]CONP-citrate, with the kidneys having higher uptake at this time, and [$^{89}$Zr]CONPs appearing in the urine by 5 minutes. For [$^{89}$Zr]CONP-PAA, kidney uptake and urine clearance are seen by 30 minutes. Of the DT10-based coatings, DT10-NH$_2$, after showing distribution in the blood stream for the first minute, only shows concentrated activity in the liver and spleen after 5 minutes. The DT10-SB coating shows continuous blood circulation over the first hour, but also shows concentrated signal in the liver and spleen after 5 minutes. The DT10-PEG coating showed undiminished blood distribution over the first hour, with much less signal from the liver and spleen.
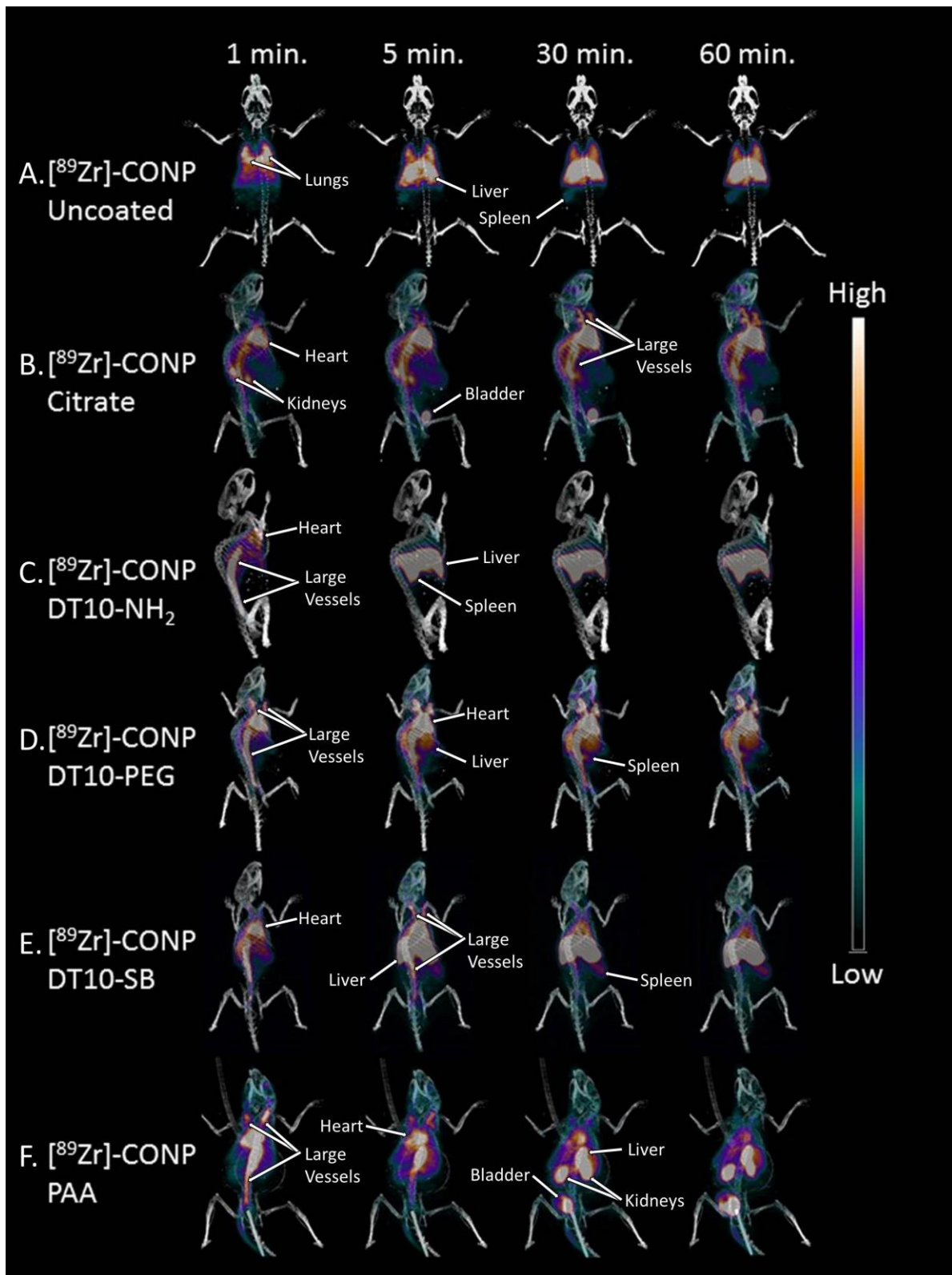
**Figure 52**: Maximum intensity projections from PET-CT dynamic scans after injection of [$^{89}$Zr]CONPs. Mice were tail vein injected with uncoated [$^{89}$Zr]CONP (A), [$^{89}$Zr]CONP-Citrate (B), [$^{89}$Zr]CONP-DT10-NH$_2$(C), [$^{89}$Zr]CONP-DT10-PEG (D), [$^{89}$Zr]CONP-DT-SB (E), [$^{89}$Zr]CONP-PAA (F) and the distribution was imaged by PET-CT over the course of one hour. Images were rotated to best show major organ uptake.

90

## 4.7.4. Analysis of $^{89}ZrCl_2$ Biodistribution

To further validate use of radioactive $^{89}Zr$ as an inherent signal for CONP detection, $^{89}ZrCl_2$ was i.v. tail vein injected and PET-CT and *ex vivo* biodistribution were performed, as seen in **Figures 53 and 54**. The results were consistent with previous $^{89}ZrCl_2$ biodistribution studies.[106] The distribution of $^{89}ZrCl_2$ was significantly different compared to the distribution of any the [$^{89}Zr$]CONPs. This demonstrates the radioactive signal was indicative of [$^{89}Zr$]CONP distribution and not that of free $^{89}Zr$.
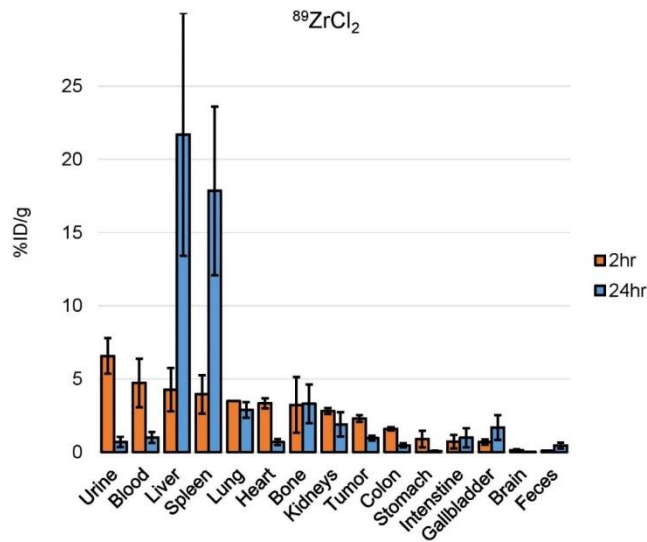


**Figure 53**: Uptake of [$^{89}Zr$]-Chloride in all excised tissues. Mice tail vein injected with [$^{89}Zr$]-Chloride were sacrificed at 2 and 24 hours post-injection and tissues were weighed and gamma counted and percent injected dose per gram (%ID/g) was determined. Organs are presented in order of highest to lowest uptake (at 2 hours), from left to right. (Mean ± SEM, n=3)
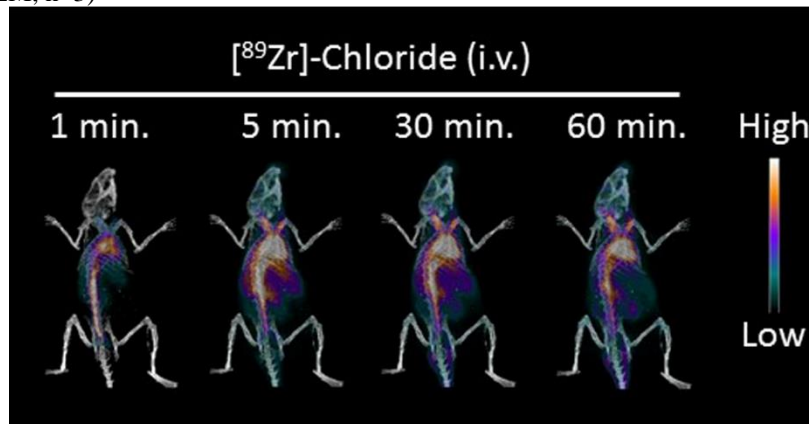


**Figure 54**: Maximum intensity projections from PET-CT dynamic scans after injection of [$^{89}Zr$]-Chloride. A mouse was tail vein injected with [$^{89}Zr$]-Chloride and the biodistribution was imaged by PET-CT over the course of 1 hour. Images were rotated to best show major organ uptake.

91

### 4.7.5. Other Routes of Administration of [89Zr]CONPs

Other than i.v. administration of [89Zr]CONPs, i.p. and oral administration routes were also tested. The distribution results of both i.p. and oral administration were poor, with the [89Zr]CONPs not leaving the intraperitoneal cavity after i.p. injection and passing through the gastrointestinal tract with minimal uptake after oral administration. Representative images of DT10-NH$_2$ and PAA coated [89Zr]CONPs show the lack of uptake at 24 hours (**Figure 55**) and *ex vivo* biodistribution showed uptake no higher than one percent injected dose per gram in any organs from either administration route (data not shown).
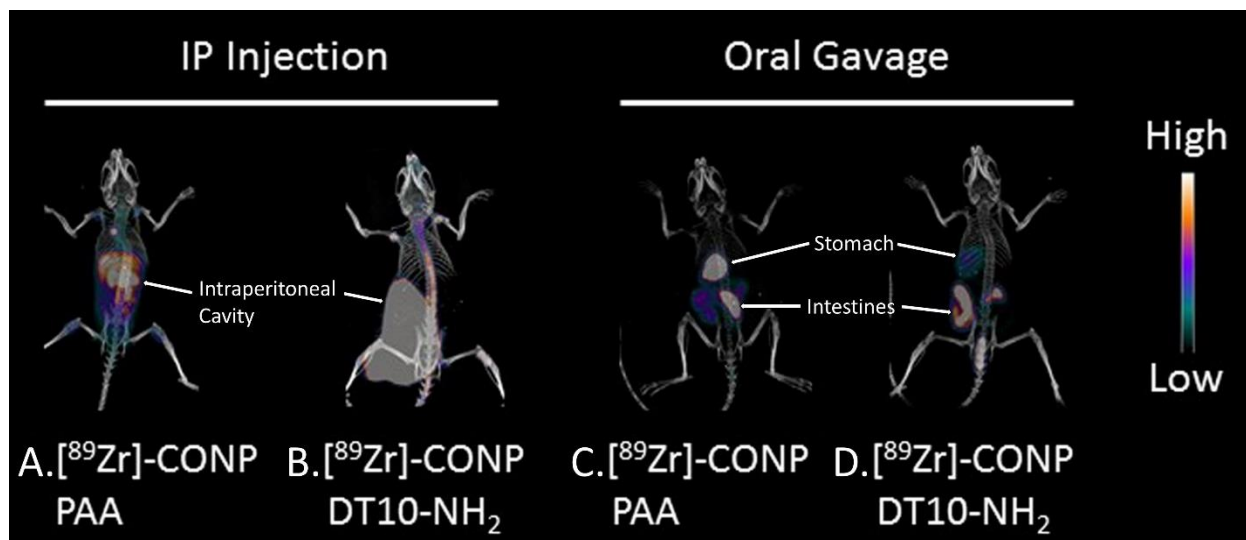


**Figure 55**: Maximum intensity projections from PET-CT scans 24 hour after i.p. injection and oral gavage of [89Zr]-CONP-PAA and [89Zr]-CONP-DT10-NH$_2$. Mice were i.p. injected or given oral gavage of PAA (A, C) and DT10-NH$_2$ (B, D) [89Zr]-CONPs and the biodistribution was imaged by PET-CT 24 hours after injection/gavage. Images were rotated to best show major organ uptake.

## 4.8. [18F]FDG Uptake Irradiated Colon Tumors with and without CONP Pre-Treatment

Analysis of [18F]FDG images before and after radiation treatment with or without CONP pre-treatment showed slight differences in tumor response based on the type of CONP given. While none of coatings showed significant difference in reduction of functional tumor volume

92

compared to radiation alone, all but one CONP variation showed less tumor control overall, as seen in **Figure 56**. Citrate CONPs, DT10-PEG CONPs, and uncoated CONPs pre-treatment before irradiation all showed less tumor functional volume reduction compared to irradiation alone. Reduction of tumor functional volume from radiation alone was 54%, compared to 34% for citrate CONP (p = 0.067), 27% for DT10-PEG (p = 0.056), and 28% for uncoated CONP (p = 0.069). While none show significance due to the large variation in tumor response, it appears that these variations of CONP seem to show some protection of the tumor from radiation, which would prevent expected tumor control and would reduce therapeutic index. On the other hand, PAA-CONP showed virtually no difference in tumor functional volume reduction compared to irradiation alone (54% vs 53%, p = 0.39). While it cannot be ruled out that the other variations of CONPs do not show radioprotection in tumor, PAA-CONP is the most likely among the tested CONPs to lack radioprotection of tumor.
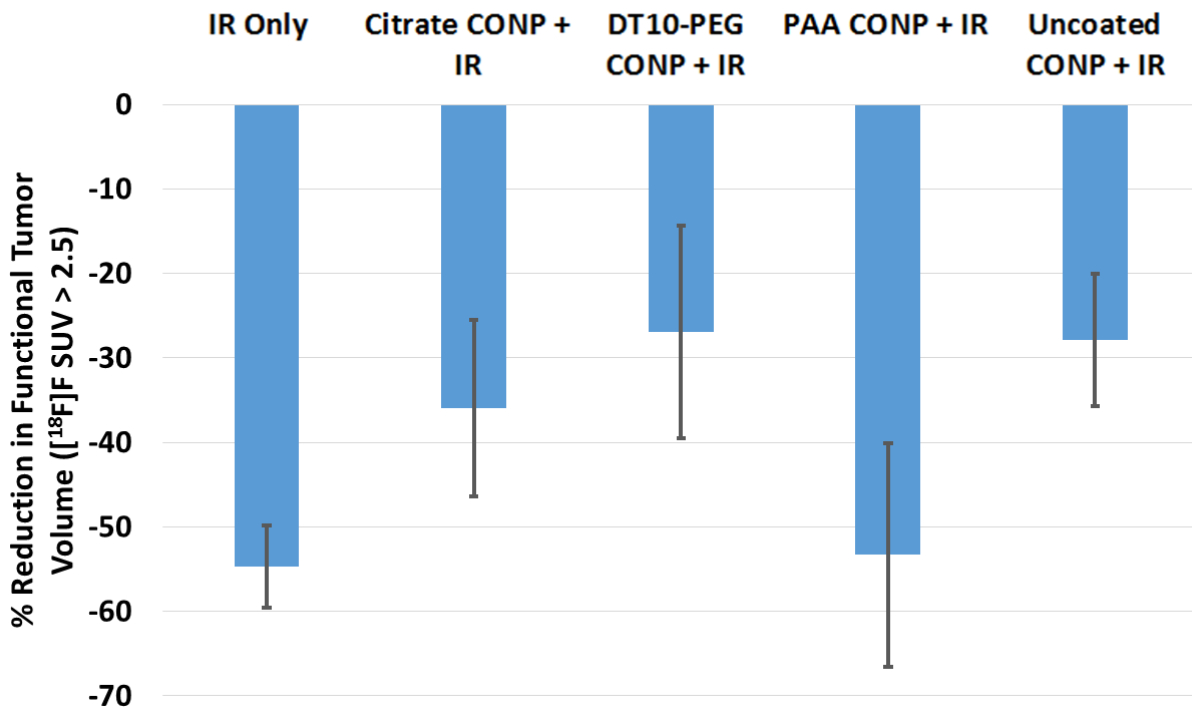


**Figure 56**: Analysis of spontaneous colon tumor response to radiation with and without CONPs as measured by [$^{18}$F]FDG PET imaging before and two weeks after radiation. All irradiated tumors showed a decrease in functional

tumor volume, but only PAA-CONP pre-treatment showed the same level of tumor control compared to irradiation alone. (Mean ± SEM, n=3-5)

## 4.9.    Colon Tissue Response to Radiation with and without CONP or Amifostine Pre-Treatment

C57BL/6 mouse colons were irradiated by the SARRP system with or without the various CONP or amifostine pre-treatment. Colons were harvested 4 hours after irradiation, sectioned, and stained on slides. The apoptotic index was measured by comparing the ratio of staining for apoptosis and background nuclear staining, as seen in **Figure 57**. The apoptotic index extremely low in untreated mice, as expected, and was highest in mice that were only irradiated. It was significantly decreased in all treated mice (citrate-CONP p = 0.024, PAA-CONP p = 0.047, DT10-PEG-CONP p = 0.025, uncoated CONP p = 0.034, and amifostine p = 0.039). These results demonstrate that all coated CONPs retain the ability to be radioprotective, and show the same level of protection as a clinical radioprotective drug.
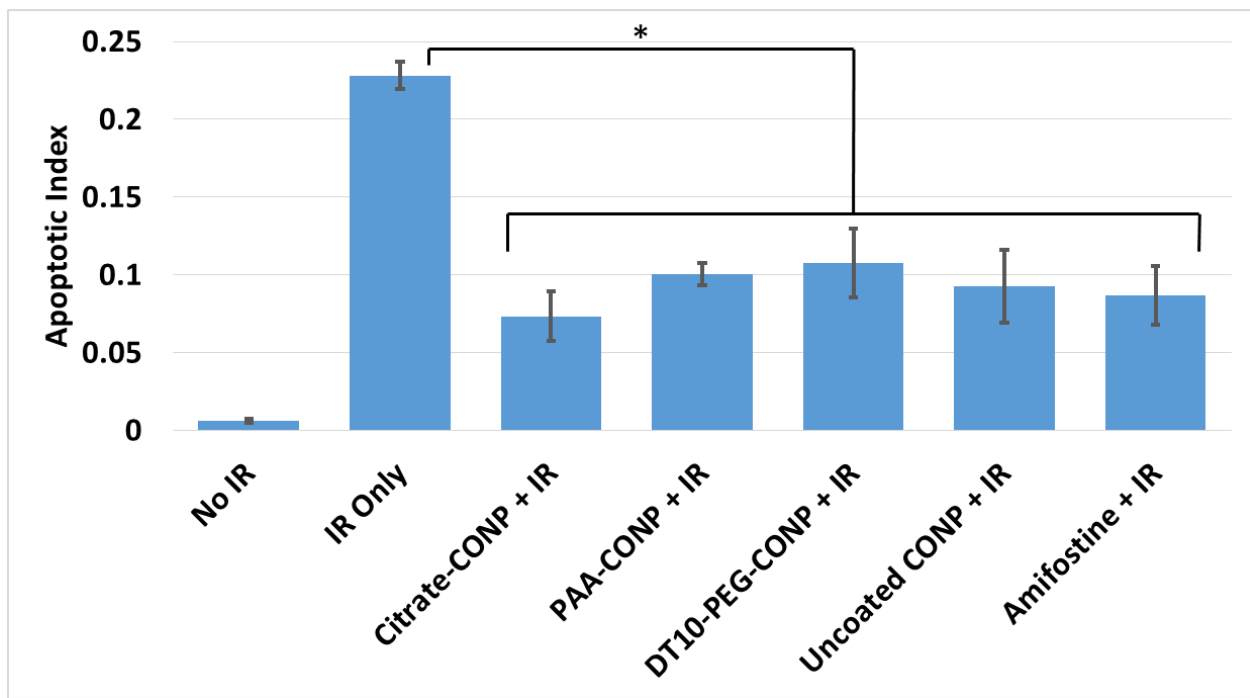


**Figure 57**: Apoptotic index in the colons of control mice and mice 4 hours after irradiation with or without CONP or amifostine pre-treatment. The apoptotic index of mouse colons was measured by *ex vivo* imaging of sections of

94

colon stained for apoptosis with a background nuclear stain for quantification by ratio measurement. Control colons showed very low apoptosis, while highest was seen in colons only irradiated. All pre-treatments showed decrease in apoptosis, indicating radioprotection, including citrate-CONP $p = 0.024$, PAA-CONP $p = 0.047$, DT10-PEG-CONP $p = 0.025$, uncoated CONP $p = 0.034$, and amifostine $p = 0.039$. (Mean $\pm$ SEM, n=3-6, * $p < 0.05$)

## *4.10.* *pH Measurement of Xenograft Tumors*

Before response of CONPs' radioprotection to tumor normalization could be measured, the method of tumor normalization needed to be verified. Three methods of pH measurement were used to determine the normalization effects of sodium bicarbonate on tumor pH. pH mapping by MRI CEST methods were developed and used to perform *in vivo* pH measurement, while the two other methods, pH needle probe measurement and SNARF-5F fluorescent imaging, required sacrifice of the animals and are less desirable approaches for pH measurement.

### 4.10.1.    MRI CEST pH Mapping

pH mapping using MRI CEST imaging and analysis methods showed change in increase in pH in the tumor volume in response to bicarbonate therapy, as seen in **Figure 58**. The bicarbonate treated mouse shows that many areas in the tumor have increased in pH, validating the normalization effects of sodium bicarbonate treatment.
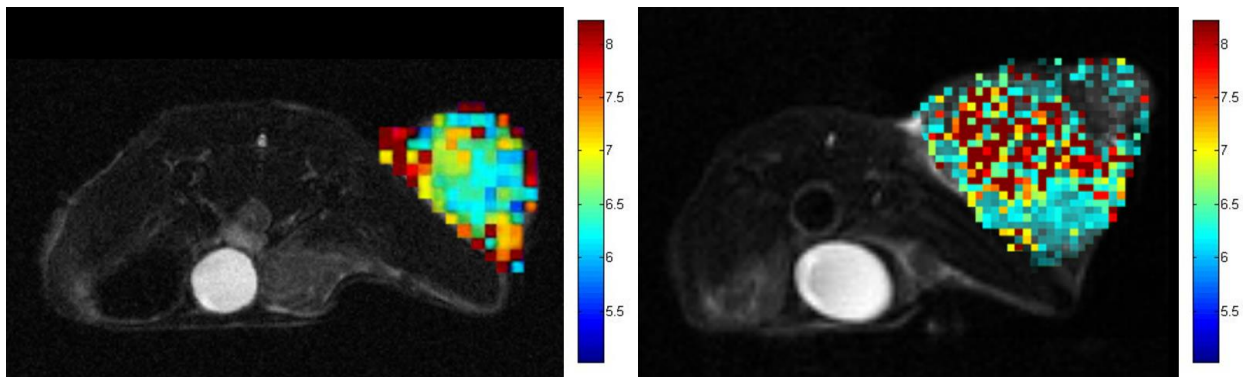


**Figure 58**: Map of tumor pH based on MRI CEST imaging and analysis, overlaid on $T_2$-weighted background image. HCT-116 xenograft bearing mice without (left) and with (right) sodium bicarbonate pre-treatment (1 M, 700 μL, oral) were imaged using a CEST protocol after iopamidol injection. The untreated mouse shows a low pH through the tumor volume, while the treated mouse shows increase in pH interspersed with low pH in the tumor volume. Areas without enough concentration of iopamidol for pH determination were removed.

### 4.10.2.    *Ex vivo* Validation of pH with pH Needle Probe and SNARF-5F Fluorescence Imaging of pH

*Ex vivo* analysis of tumor pH was done with a pH needle electrode probe, which was inserted into the tumors of HCT-116 xenograft bearing mice for direct pH measurement. The tumor pH of untreated animals ranged from 6.82 to 7.19. pH of HCT-116 xenograft tumors was also measured in mice three hours after sodium bicarbonate treatment. These tumors showed a much narrower range of pH, 7.20 to 7.33, and was significantly higher than untreated, as seen in **Figure 59** (6.92 vs 7.24, p < 0.00001).
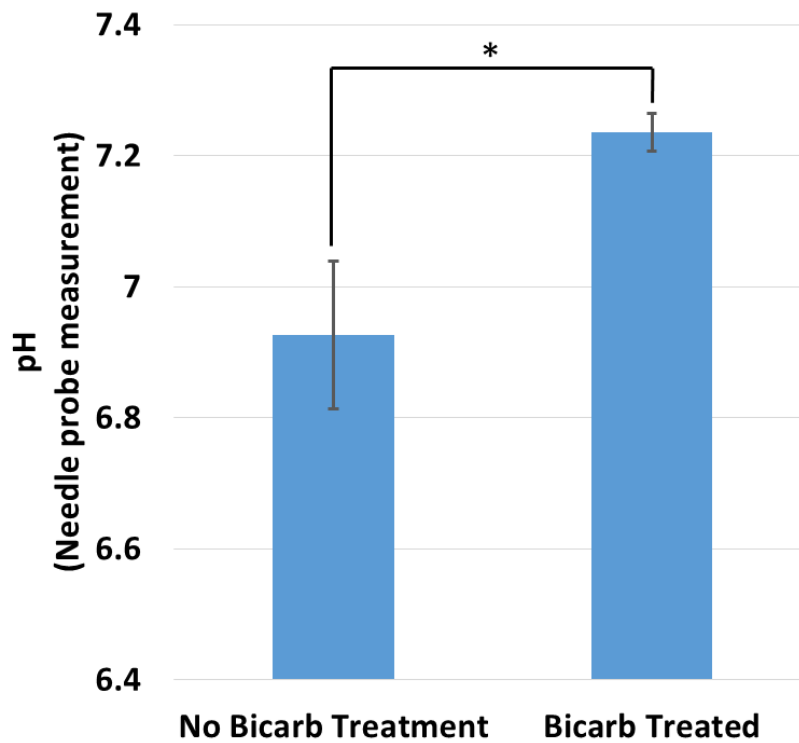


**Figure 59**: Needle pH probe direct measurements of tumor pH of untreated and sodium bicarbonate treated mice. Untreated mice showed a wider variation and significantly lower pH than mice treated with sodium bicarbonate (* p < 0.00001), indicating successful normalization of tumor microenvironment by sodium bicarbonate treatment. (Mean ± SEM, n=5-6)

### 4.10.1.    Tumor pH Imaging by SNARF-5F

*Ex vivo* tumor sections from mice injected with SNARF-5F were imaged and spectrally unmixed by using the spectrums of the reference SNARF-5F pH solutions. Images revealed heterogeneity with areas of low pH in untreated tumors, while tumors from mice treated with sodium bicarbonate showed much more homogenous pH that was closer to physiological pH of 7.4, as seen in **Figure 60**.
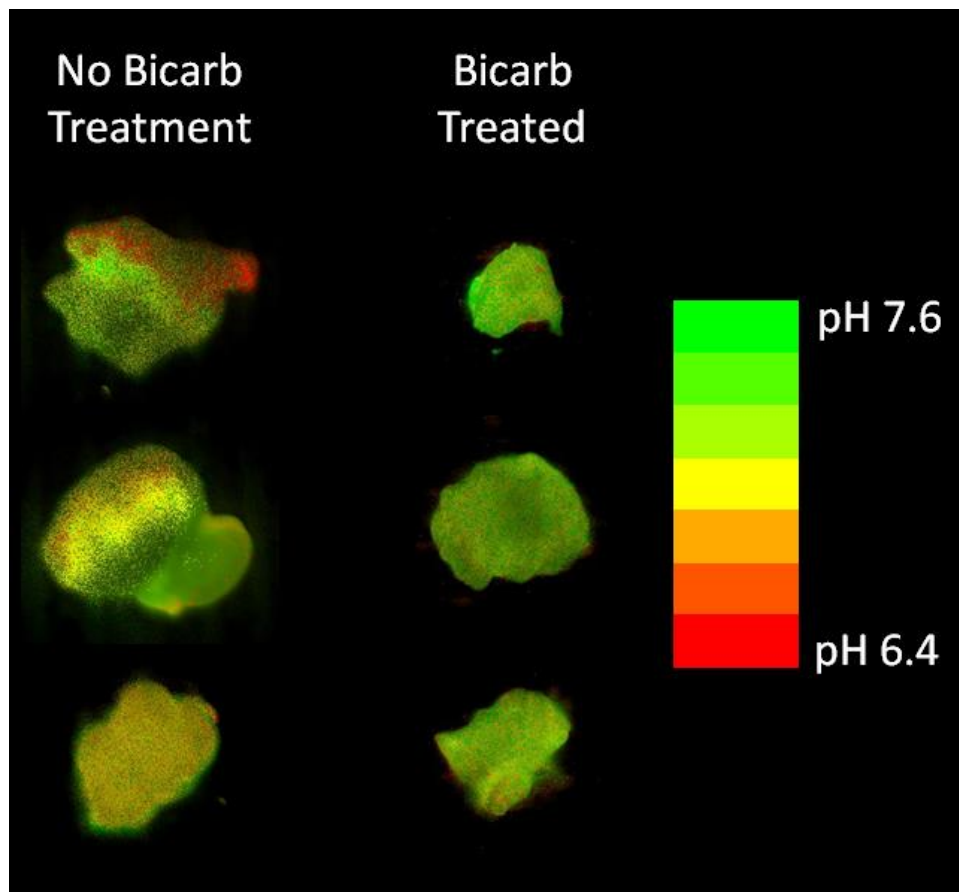


**Figure 60**: *Ex vivo* SNARF-5F imaging of tumor sections of untreated mice and sodium bicarbonate treated mice. Xenograft tumors that were sectioned from untreated (left) showed much more heterogeneity and lower pH than tumors from mice treated with sodium bicarbonate (right).

97

## 4.11. Effects of Tumor pH Normalization on PAA-CONPs Radioprotection of Xenograft Tumors

Volume change of irradiated mouse xenograft tumors with and without radiation and pre-treatment combinations of sodium bicarbonate alone, PAA-CONP alone, and sodium bicarbonate and PAA-CONP were measured by MRI before and two weeks after treatment, as seen in **Figure 61**. All radiation treatment groups saw significantly less increase in tumor volume than control mice except in sodium bicarbonate and PAA-CONP pre-treated mice (IR only $p = 0.039$, Bicarb + IR $p = 0.048$, PAA-CONP + IR $p = 0.039$, Bicarb and PAA + IR $p = 0.060$). While the difference in p-values are small, the significant difference in tumor response for non-normalized, lower pH tumors treated with PAA-CONP before radiation and lack of significant difference in tumor response for normalized, higher pH tumors supports the theory that change in pH alters CONPs' radioprotective properties *in vivo*.
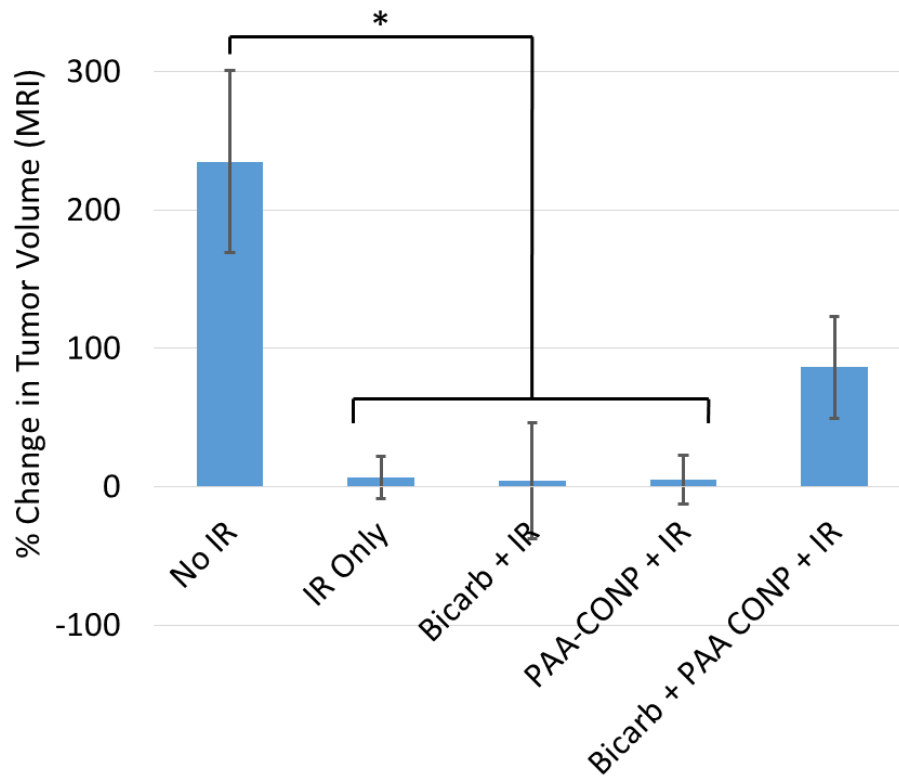
**Figure 61**: Percent increase in xenograft tumor volume in control and irradiated tumors with PAA-CONP alone, sodium bicarbonate alone, or sodium bicarbonate and PAA-CONP pre-treatment, as measured by MRI. MRI images were taken before and two weeks after treatment and volumes, measured in ImageJ by VolumEst, were compared in mice without treatment, irradiated only, pre-treated with sodium bicarbonate before irradiation, pre-treated with PAA-CONP before irradiation, or pre-treated with both sodium bicarbonate and PAA-CONP before irradiation. All irradiated tumors saw a significant decrease in tumor growth compared to control except sodium bicarbonate and PAA-CONP pre-treatment (IR only $p = 0.039$, Bicarb + IR $p = 0.048$, PAA-CONP + IR $p = 0.039$, Bicarb and PAA + IR $p = 0.060$). These results indicate radioprotective properties of CONPs may be absent in the acidic pH of the tumor, but return when the pH is normalized. (Mean $\pm$ SEM, n=3, * $p < 0.05$)

# 5. Chapter 5 – Discussion

## 5.1. Coated and $^{89}$Zr Labeled CONPs as Methods to Improve and Study Pharmacokinetics

$^{89}$Zr is an attractive PET radioisotope with increasing clinical use in immuno-PET imaging of receptor targeting antibodies and peptides.[107–110] It has a useful half-life of 78 hours, suitable for both short and long term kinetic studies. Preclinical and clinical research with $^{89}$Zr has been enhanced by the availability of the radioisotope from widely available medical cyclotrons. Although we have incorporated various radioisotopes into the CONP core, the use $^{89}$Zr allows for high sensitivity PET imaging and the potential for clinical translation. Doping of non-radioactive zirconium into the core of CONPs (with up to 15% efficiency), has been previously reported as very stable, with the retention of cerium oxide's native cubic fluorite structure.[111] Our results also showed good incorporation of stable zirconium, especially at 0.5%. These procedures used a much higher concentration of Zr, compared with the trace amount of $^{89}$Zr incorporated into [$^{89}$Zr]CONPs radiosynthesis, which is on the order of $10 - 100$ ng. While Radio-ITLC showed some instability of citrate-, PAA-, and DT10-SB coated [$^{89}$Zr]CONPs in retention of $^{89}$Zr activity, the results were comparable to other $^{89}$Zr compounds used for *in vivo* studies. UV- and radio-HPLC analysis showed that the radioactivity is associated with the CONP UV retention time from aqueous and *in vivo* blood samples, demonstrating good stability of [$^{89}$Zr]CONP *ex vivo*. This validates the use of the $^{89}$Zr radioactive signal to report on the overall CONP

www.manaraa.com

biodistribution. We have previously tested several materials, as CONP coating ligands, including glucose, cyclodextran, mannose, maltose, dextran-T10, ascorbic acid and dehydroascorbic acid, but all were deemed unworthy for pursuit due to low reaction yields or poor stability (data not shown). The investigated ligands in this paper all showed very high reaction yields and good stability over months to years, with the notable exception of citrate coated CONP, which had a stable shelf life of about two weeks before showing signs of aggregation. The functionalization of DT10 with sulfobetaine, amine and polyethylene glycol not only served to better stabilize the CONPs, but also allowed the determination of surface charge effects on CONP biodistribution, having negative, positive and near neutral surface charge, respectively.

## 5.2. Comparison of coatings and CONPs vs [$^{89}$Zr]CONP

Surface coatings on CONPs were able to change the physicochemical and biodistribution properties of CONPs while retaining their redox properties and low toxicity. $^{89}$Zr labeling was intended to not disrupt any of these properties, allowing for detection of the nanoparticles without affecting any other properties. This project was successful in achieving these aims, as described below.

### 5.2.1. Size and surface charge

Surface coating showed an excellent ability to reduce the size of CONPs, impart a surface charge on the nanoparticle, and stably dissolve in water and saline. The hydrodynamic size and zeta potential surface charge of coated and uncoated CONPs and their counterpart [$^{89}$Zr]CONPs were shown to be almost identical.

101

### 5.2.2. Autocatalytic activity

It was important to determine if there were any effects of the coating on the redox properties of CONPs so that they can still exert their anti-oxidant properties in a biologically relevant environment. The reaction of the coated CONPs with $H_2O_2$ and their cycling to their original oxidation state was not hindered, indicating that the coatings were not affecting the cerium oxide core from reacting with radicals in solution, nor its ability catalytically to cycle back to its original oxidation state.

The coated CONPs returned to baseline much more effectively than the uncoated CONPs. The apparent better recycling of the coated CONPs is possibly due to increased surface-area-to-volume ratio of smaller NPs, leading to an increased ability to react with $H_2O_2$ and cycle back. The addition of $H_2O_2$ on day 6 served to demonstrate true recycling of redox properties where the CONPs are able to react again with $H_2O_2$ with similar results to the initial reaction. [$^{89}$Zr]CONPs showed an enhanced cycling of redox ability, possibly due to energy imparted to the cerium on the surface by the radioactive isotope. This was further confirmed with UV light showing the same enhancement of redox cycling, though more studies need to be done to confirm this hypothesis.

### 5.2.3. Toxicity

Unlike other metal based NPs, CONP has been demonstrated to have very low toxicity in a number of studies.[112] Cell toxicity data showed the $^{89}$Zr CONPs are non-toxic up to very large concentrations. The toxicity of the PAA coated CONPs has been improved from previous studies that showed toxicity as low as 40 μg/ml.[52] The modified synthesis of coated CONPs, using a reduced ratio of coating molecule to cerium salt in the starting solution, resulted in significantly less toxicity of PAA CONPs, sowing toxicity only at the highest concentration tested at 120

µg/mL. *In vivo* toxicity was also indirectly monitored during the high dose injections (~40 mg/kg) required for PET imaging and whole body radioactivity monitoring. Only citrate- and DT10-NH$_2$ showed lethality at these doses, and appeared to be well tolerated in all other CONPs.

### 5.2.4. *In Vivo* Biodistribution

Through following the distribution of [$^{89}$Zr]CONPs, we were able to determine how the coated [$^{89}$Zr]CONPs compared to the uncoated in terms of organ uptake and retention. PET-CT imaging of [$^{89}$Zr]CONPs showed difference in biodistribution between the coated and uncoated NPs which was apparent by the first minute after i.v. injection. The uncoated [$^{89}$Zr]CONPs showed immediate distribution almost exclusively to the lung, with later increased uptake by the liver and spleen. It is most likely that the significant lung uptake of the uncoated [$^{89}$Zr]CONPs is due to aggregation to micrometer particles that become lodged in the capillary bed of the lungs on the first pass, similar to the lung handling of the lung imaging agent, $^{99m}$Tc macroaggregated albumin ($^{99m}$Tc-MAA).[113] This likely also explains why uncoated [$^{89}$Zr]CONPs have the highest uptake in the heart, again due to trapping after first pass following i.v. injection.

The images/video of the dynamic scans of the coated [$^{89}$Zr]CONPs show significant differences in distribution. The citrate, PAA and DT10-PEG coated [$^{89}$Zr]CONPs were able to avoid immediate uptake by the RES organs of liver and spleen. DT10-NH$_2$ and DT10-SB coated [$^{89}$Zr]CONPs showed high uptake in these organs after only 5 minutes. The strong positive and negative charge, respectively, of these coatings may make it easier for the endocytotic cells of the RES to sequester them from circulation, while the neutral coating of DT10-PEG allows longer escape from RES.[51] The PAA coated [$^{89}$Zr]CONPs were best able to avoid uptake by the RES, showing the lowest uptake in both the liver and spleen at 24 hours.

103

Renal clearance was enhanced in the PAA and citrate coated [89Zr]CONPs. With a hydrodynamic size less than 5.5 nm, citrate and PAA coated [89Zr]CONPs were able to be cleared through renal glomerular filteration.[114] The DT10 based coatings were above the size threshold for renal clearance, so they had minimal clearance through the urine. [89Zr]CONP-citrate renal clearance began almost immediately, with high uptake in the kidneys at 1 minute and appearance in the urine at 5 minutes. There was almost no evidence of activity in the urine at 2 hours post injection, indicating very rapid renal clearance. [89Zr]CONP-PAA showed renal clearance by 30 minutes and a slightly prolonged clearance, with activity still detected in the urine at 2 hours, but mostly cleared by 24 hours. Hepatobiliary clearance of [89Zr]CONPs was also seen, with uptake in the gallbladder, which empties into the intestines and is cleared by the feces. [89Zr]CONP-DT10-SB especially showed this method of excretion, with the highest activity in the gallbladder and feces at 24 hours.

The uptake of the [89Zr]CONPs in the major organs is important to note, as these organs are potential targets for protection from oxidative damage. The high uptake of uncoated [89Zr]CONPs in the lung and heart may mean they are good candidates for protection of those organs, but may also lead to prolonged retention and hence could have toxicity implications. Uncoated [89Zr]CONPs also showed the least uptake in all other major organs. Among the coated [89Zr]CONPs, PAA showed a more evenly distributed profile pattern in major organs, making it a good candidate for multiple tissue protection, such as during chemo- or radio-therapy. Compared to normal tissues, [89Zr]CONP-PAA also showed less uptake in colon tumor; this could have important implication during chemo- or radio-therapy where tumor protection is not desirable. Conversely, [89Zr]CONP-citrate showed more uptake in colon tumor compared to

normal colon. This may indicate that [$^{89}$Zr]CONP-citrate could be a useful candidate as an adjuvant anti-cancer agent.[72]

## 5.3.     pH Effects on CONPs

pH was shown to have an significant impact on CONPs ability to react with $H_2O_2$, reducing its ability to convert from $Ce^{3+}$ to $Ce^{4+}$ in slightly acidic pH, indicating a possible mechanism for lack of protection in the acidic tumor microenvironment. Uptake was also affected, but the two cell lines studies showed different results. COLO-205 cells showed decreased uptake only at pH 6.6, compared to pH 7.4 and 7.0, while HCT-116 showed decreased uptake at pH 7.0 but increase uptake at pH 6.6, compared to cells grown in pH 7.4 media. This may mean that tumor uptake of CONPs *in vivo* is unpredictable, but it should not be a concern if they show no protection in the tumor regardless. Clonogenic assay of cells grown in pH 7.4 showed an increase in colony formation when incubated in CONPs before being irradiated, though not significantly. There was no change in colony formation with and without CONPs at pH 7.0, indicating lower pH may be ideal for preventing radioprotection in tumors.

## 5.4.     Radiation Protection by CONPs in vivo

CONPs effects on irradiated tissue *in vivo* were measured in both spontaneous colon tumors and normal colon tissue, while the effects of tumor normalization on CONPs' radioprotection were measured in xenograft tumors.

### 5.4.1. Spontaneous Colon Tumor Response to CONPs/Radiation

[$^{18}$F]FDG PET imaging of colon tumors before and after radiation with the variations of CONPs showed that only PAA-CONP had no noticeable effect on tumor response compared to tumors that were only irradiated. While not significant compared to radiation alone, citrate-, DT10-PEG,

105

and uncoated CONPs showed a less of a decrease in functional tumor volume after irradiation, indicating less tumor control and possible radiation protection. PAA-CONPs' lack of protection of the tumor makes them ideal because a radioprotective drug should not adversely affect the therapeutic index of radiation therapy.

### 5.4.2. Protection of Colon Tissue

All of the tested CONPs were able to significantly reduce apoptosis in irradiated colon. Being the most important aspect of a radioprotective drug, the protection of normal tissue, it was encouraging to see that all formulations of CONPs showed this property. They also showed the same level of protection as amifostine, which would likely indicate CONPs ability to compete with this drug as a radioprotector, and be much more likely for widespread use in the clinic if its toxicity profile is as low as expected. This is indicative of the fact that the radioprotective properties are due to the core CONP redox properties while the different coatings influence cellular and tissue interactions within specific microenvironments.

### 5.4.1. Effects of pH Normalization in Tumors on CONPs Radioprotection

Normalization of the pH of irradiated xenograft tumors caused CONPs to not be able to show significant difference in tumor growth compared to control tumors, indicating that CONPs may retain their radioprotective properties if the pH of tumors is closer to a physiological pH of 7.4, while CONP treatment in tumors without normalization showed no radioprotection. This is supported by studies of the effects of pH on CONPs in solution and *in vitro*, and shows that acidic pH may be the reason CONPs show ideal radioprotection in normal tissue which is reduced in tumors.

106

# 6. Chapter 6 – Conclusions

## 6.1. Successful Synthesis of Coated and $^{89}$Zr Labeled CONPs

Reaction yields for both coated and $^{89}$Zr labeled CONPs were excellent and reproducible, with ~80% or greater yield for all reactions. The coating of and radioisotope incorporation into CONPs also were shown to be stable and have no effect on their redox properties and toxicity. Overall, the coating of and radioisotope incorporation into CONPs were shown to have no effect on their redox properties and toxicity.

## 6.2. Coating of CONPs Improves their Biodistribution and Pharmacokinetics

The type of coating on [$^{89}$Zr]CONPs greatly alters their biodistribution profile. Compared to uncoated [$^{89}$Zr]CONPs, coatings increased the uptake of [$^{89}$Zr]CONPs in all major organs except the lungs and heart. Higher uptake in radiation and chemo sensitive organs such as the colon, heart, lungs and kidneys, will hopefully improve dose-related performance of coated CONPs as a protective drug. A further indication of the promising clinical application of coated CONPs is the improved renal clearances of citrate and PAA coated [$^{89}$Zr]CONPs, and improved hepatobiliary clearance of [$^{89}$Zr]CONP-DT10-SB. This was especially noted with PAA-[$^{89}$Zr]CONPs in the whole body activity measurements where 75% cleared after only 4 hours. Improved clearance of

107

coated [$^{89}$Zr]CONPs may allow expedited translation to the clinic because clearance minimizes toxicity and allows radiological imaging, i.e. PET, as exemplified in this study.

## *6.3.     CONPs Show Similar Radioprotection Compared to Amifostine*

The radioprotection by CONPs in normal colon was shown to be no different than amifostine pre-treated mice. This demonstration of comparable performance compared to an established radioprotective drug shows even greater potential for CONPs' clinical application. It is especially important to note that the dose given in the clinic and for the mice in this study was 400 mg/kg, which is much higher than the dose, 1 mg/kg cerium weight, given for CONPs. Although more studies need to be performed, it is hoped that CONPs could see wider adoption than amifostine due to their likely less toxicity and potential targeted protection.

## *6.4.     pH Microenvironment of Tumors May Change the Antioxidant and Radioprotective Properties of CONPs*

PAA-CONPs appeared to show some radioprotection in xenograft tumors where pH was normalized, while absent in untreated tumors, indicating pH as a mechanism by which acidic tumors may prevent CONP radioprotection. While encouraging, these experiments need to be repeated due to the wide variation in tumor response and noticeable amount of necrosis in the tumors, which may have affected volume measurements by MRI imaging. This is a case where molecular imaging may not always be the best route for measurement of response. Experiments will have to be repeated, with *ex vivo* clonogenic assay of tumors being the best candidate excellent results from this study, as seen in **Section 4.6**.

## 6.5.     PAA-CONPs are a Good Candidate for Translation to the Clinic

From the studies done, it seems clear that there is one standout among the coated CONPs that were tested. PAA-CONPs best meet the four criteria set forth for an ideal radioprotective drug. Their biodistribution shows excellent uptake in normal tissues, with reduced uptake in the reticuloendothelial system and tumors while being excreted in the urine by 75% after only 4 hours. Their toxicity is low, with *in vitro* toxicity only at the highest dose tested and *in vivo* with a dose forty times the therapeutic dose being well tolerated by mice monitored over the course of one week. They show good protection of colon tissue measured as reduction of apoptosis, similar to uncoated CONPs and amifostine, an established radio-protective drug. They do not alter the radiation response of tumors, so therapeutic index of radiation in tumor should not be affected. It is therefore the conclusion that PAA-CONPs show the most promise for further investigation as a radioprotective drug.

# 7. Chapter 7 – Future Work

## *7.1.     Dose-Response Relationship*

Based on the research from this project, future studies will likely focus on therapeutic

applications of PAA-CONPs. Studies can be done on dose-response relationship to try to

determine if doses lower than 1 mg/kg cerium weight still have radioprotective effects and can

further reduce concerns for toxicity.

## *7.2.     Investigate Other Organ Systems*

The colon is one of many organ systems at risk during radiation therapy. Currently, there are

plans to study the esophagus, and surrounding tissue such as lungs and heart, for radioprotection

from CONPs. This research would have immediate application in the clinic due to the severe side

effects from radiation therapy of patients with esophageal cancer.

## *7.3.     Investigate Efficacy in Combination (Chemo and Radiation)*
## *        Therapy or Chemotherapy Alone*

Like radiation therapy, chemotherapy has severe side effects that decrease patient quality of life.

Many of the mechanisms of chemotherapeutic drugs rely on oxidative stress, which could be

prevented in normal tissues by CONPs with a similar mechanism as in radiation therapy. Due to

PAA-CONPs high uptake in the kidneys and high renal toxicity of many chemotherapeutics,

such as cisplatin, it is planned to determine if PAA-CONPs have a good application in reducing

110

chemo renal toxicity. Similarly, doxorubicin has cardiac toxicity, and CONPs will be studied to determine if they can reduce these side effects. Even just in studying CONPs as a radioprotective drug, it is still important to determine CONPs effects on chemotherapy because so many patients undergo combination radiation/chemo-therapy. Preliminary data shows retention of ejection fraction in rats pre-treated with CONPs before doxorubicin chemotherapy, which is normally decreased with doxorubicin therapy and is currently under further study.

## *7.4. Planning for CONPs use in the clinic*

We are currently planning collaboration with the MCV Massey Gastrointestinal Oncology Group and Dr. Khalid Matin to pursue a clinical trial for CONPs in esophageal cancer patients undergoing radiation therapy. Before first in human clinical trials, CONPs must go through preparation and testing. This includes developing an investigational new drug (IND) application and extensive toxicity studies. While clinical trials are still a ways off, we are currently planning collaboration with the MCV Massey Gastrointestinal Oncology Group and Dr. Khalid Matin to pursue a clinical trial for CONPs in esophageal cancer patients undergoing radiation therapy.

# Appendix

## *Research publications from this work*

- **McDonagh PR**, Sundaresan G, Yang L, Sun M, Mikkelsen R, Zweit J. Improving Pharmacological Profile of Cerium Oxide Nanoparticles Through Surface Modifications: Interrogated by Molecular PET Imaging of [$^{89}$Zr]CONP. *Nanomedicine: Nanotechnology, Biology and Medicine* (in preparation).

- Hoffman, D. Yang L, Sun M, Sundaresan G, **McDonagh PR**, Corwin F, Wang L, Thadigiri C, Zweit J. Intrinsically radiolabeled [$^{59}$Fe]-SPIONs for dual MRI/radionuclide detection. *Am J Nucl Med Mol Imaging* 4, 548–560 (2014).

- Yang L, Sundaresan G, Sun M, Jose P, Hoffman D, **McDonagh PR**, Lamichhane N, Cutler CS, Perez JM, Zweit J. Intrinsically radiolabeled multifunctional cerium oxide nanoparticles for *in vivo* studies. *J. Mater. Chem. B* 1, 1421-1431 (2013).

## *Conferences and Presentations*

- **McDonagh PR**, Yang L, Jose P, Sundaresan G, Alam A, Mikkelsen R, Zweit J. Molecular Imaging Approaches to Study Normal Tissue Protection by Multi-Functional Cerium Oxide Nanoparticles During Radiation Therapy. Poster presentation at AACR-SNMMI Joint Conference: State-of-the-Art Molecular Imaging in Cancer Biology and Therapy, Hard Rock Hotel, San Diego, CA, February 12, 2015.

- **McDonagh PR.** Multi-Modal Molecular Imaging to Study Radio-Protection by Cerium Oxide Nanoparticles. Invited Oral Presentation at the 39th International Conference and Expo on Advanced Ceramics and Composites, Hilton Daytona Beach Resort and Ocean Center, Daytona Beach, FL, January 27, 2014.

- Yang L, Sundaresan G, Sun M, Jose P, **McDonagh PR**, Zweit J. Intrinsically Radiolabeled Multifunctional Cerium Oxide nanoparticles for *in vivo* studies. Poster presentation at American Association of Cancer Research Annual Meeting 2013, Walter E. Washington Convention Center, Washington, DC, April 9, 2013.

# List of References

1.  Sun, M. *et al.* Highly stable intrinsically radiolabeled indium-111 quantum dots with multidentate zwitterionic surface coating: dual modality tool for biological imaging. *J. Mater. Chem. B* **2,** 4456–4466 (2014).

2.  Cancer Facts & Figures 2016 | American Cancer Society. Available at: http://www.cancer.org/research/cancerfactsstatistics/cancerfactsfigures2016/. (Accessed: 16th March 2016)

3.  Etheridge, M. L. *et al.* The big picture on nanomedicine: the state of investigational and approved nanomedicine products. *Nanomedicine* **9,** 1–14 (2013).

4.  Colon, J. *et al.* Cerium oxide nanoparticles protect gastrointestinal epithelium from radiation-induced damage by reduction of reactive oxygen species and upregulation of superoxide dismutase 2. *Nanomedicine* **6,** 698–705 (2010).

5.  Tarnuzzer, R. W., Colon, J., Patil, S. & Seal, S. Vacancy Engineered Ceria Nanostructures for Protection from Radiation-Induced Cellular Damage. *Nano Lett.* **5,** 2573–2577 (2005).

6.  Madero-Visbal, R. A. *et al.* Harnessing nanoparticles to improve toxicity after head and neck radiation. *Nanomedicine: Nanotechnology, Biology and Medicine* **8,** 1223–1231 (2012).

7.  Colon, J. *et al.* Protection from radiation-induced pneumonitis using cerium oxide nanoparticles. *Nanomedicine: Nanotechnology, Biology and Medicine* **5,** 225–231 (2009).

8. Celardo, I., Traversa, E. & Ghibelli, L. Cerium oxide nanoparticles: a promise for applications in therapy. *J. Exp. Ther. Oncol.* **9,** 47–51 (2011).

9. Wason, M. S. *et al.* Sensitization of Pancreatic Cancer Cells to Radiation by Cerium Oxide Nanoparticle-Induced ROS Production. *Nanomedicine* **9,** 558–569 (2013).

10. Frantz, C., Stewart, K. M. & Weaver, V. M. The extracellular matrix at a glance. *J Cell Sci* **123,** 4195–4200 (2010).

11. Balkwill, F. R., Capasso, M. & Hagemann, T. The tumor microenvironment at a glance. *J Cell Sci* **125,** 5591–5596 (2012).

12. Trédan, O., Galmarini, C. M., Patel, K. & Tannock, I. F. Drug Resistance and the Solid Tumor Microenvironment. *JNCI J Natl Cancer Inst* **99,** 1441–1454 (2007).

13. Schwarz, S. B. *et al.* Iodine-125 brachytherapy for brain tumours - a review. *Radiat Oncol* **7,** 30 (2012).

14. Decker, W. E., Erickson, B., Albano, K. & Gillin, M. Comparison of traditional low-dose-rate to optimized and nonoptimized high-dose-rate tandem and ovoid dosimetry. *International Journal of Radiation Oncology*Biology*Physics* **50,** 561–567 (2001).

14. Cancer Research UK. Diagram showing the position of the applicators for internal radiotherapy for cervical cancer. Wikipedia, the free encyclopedia (2014). http://creativecommons.org/licenses/by-sa/4.0/

16. Fakiris, A. J. *et al.* Intraperitoneal radioactive phosphorus (32P) and vaginal brachytherapy as adjuvant treatment for uterine papillary serous carcinoma and clear cell carcinoma: a phase II Hoosier Oncology Group (HOG 97-01) study. *Gynecologic Oncology* **96,** 818–823 (2005).

114

17. Dickie, G. J. & Macfarlane, D. Strontium and samarium therapy for bone metastases from prostate carcinoma. *Australasian Radiology* **43,** 476–479 (1999).

18. Parker, C. *et al.* Alpha Emitter Radium-223 and Survival in Metastatic Prostate Cancer. *New England Journal of Medicine* **369,** 213–223 (2013).

18. Username: Cepheiden. Particle therapy. Wikipedia, the free encyclopedia (2016). https://creativecommons.org/licenses/by-sa/3.0/deed.en

19. Username:Egg. Multi-leaf collimator. FN Motol, Prague, 2006-12-01. Wikipedia, the free encyclopedia (2006). https://creativecommons.org/licenses/by-sa/2.5/deed.en

20. Ekambaram, V. & Velayudham, R. Analysis of low dose level volumes in intensity modulated radiotherapy and 3-D conformal radiotherapy. International Journal of Cancer Therapy and Oncology 2, (2014). http://creativecommons.org/licenses/by/3.0/

22. Yanagihara, K. *et al.* Radiation-induced Apoptotic Cell Death in Human Gastric Epithelial Tumour Cells; Correlation Between Mitotic Death and Apoptosis. *International Journal of Radiation Biology* **67,** 677–685 (1995).

23. Barnett, G. C. *et al.* Normal tissue reactions to radiotherapy: towards tailoring treatment dose by genotype. *Nat. Rev. Cancer* **9,** 134–142 (2009).

24. Hall, E. J. *Radiobiology for the radiologist*. (Wolters Kluwer Health/Lippincott Williams & Wilkins, 2012).

25. Nair, C. K., Parida, D. K. & Nomura, T. Radioprotectors in radiotherapy. *J. Radiat. Res.* **42,** 21–37 (2001).

26. Citrin, D. *et al.* Radioprotectors and Mitigators of Radiation-Induced Normal Tissue Injury. *The Oncologist* **15,** 360–371 (2010).

27. Brizel, D. M. *et al.* Phase III Randomized Trial of Amifostine as a Radioprotector in Head and Neck Cancer. *JCO* **18,** 3339–3345 (2000).

28. De Souza, C. A. *et al.* Amifostine (WR-2721), a cytoprotective agent during high-dose cyclophosphamide treatment of non-Hodgkin's lymphomas: a phase II study. *Brazilian Journal of Medical and Biological Research* **33,** 791–798 (2000).

29. K. K Jain. *The handbook of nanomedicine*. (Humana Press, 2012).

30. Rizzo, L. Y., Theek, B., Storm, G., Kiessling, F. & Lammers, T. Recent Progress in Nanomedicine: Therapeutic, Diagnostic and Theranostic Applications. *Curr Opin Biotechnol* **24,** (2013).

31. Liu, H. & Webster, T. J. Nanomedicine for implants: A review of studies and necessary experimental tools. *Biomaterials* **28,** 354–369 (2007).

32. Singh, S. & Singh, A. Current status of nanomedicine and nanosurgery. *Anesth Essays Res* **7,** 237–242 (2013).

33. Patel, G. M., Patel, G. C., Patel, R. B., Patel, J. K. & Patel, M. Nanorobot: A versatile tool in nanomedicine. *Journal of Drug Targeting* **14,** 63–67 (2006).

34. Vinardell, M. P. & Mitjans, M. Antitumor Activities of Metal Oxide Nanoparticles. *Nanomaterials* **5,** 1004–1021 (2015).

35. Jong, W. H. D. & Borm, P. J. Drug delivery and nanoparticles: Applications and hazards. *International Journal of Nanomedicine* **3,** 133 (2008).

36. Kreuter, J. Drug targeting with nanoparticles. *Eur. J. Drug Metab. Pharmacokinet.* **19,** 253–256 (1994).

37. Cho, K., Wang, X., Nie, S., Chen, Z. (Georgia) & Shin, D. M. Therapeutic Nanoparticles for Drug Delivery in Cancer. *Clin Cancer Res* **14,** 1310–1316 (2008).

116

38. Thakor, A. S. & Gambhir, S. S. Nanooncology: The future of cancer diagnosis and therapy. *CAA Cancer Journal for Clinicians* **63,** 395–418 (2013).

39. De Jong, W. H. *et al.* Particle size-dependent organ distribution of gold nanoparticles after intravenous administration. *Biomaterials* **29,** 1912–1919 (2008).

40. Asati, A., Santra, S., Kaittanis, C. & Perez, J. M. Surface-Charge-Dependent Cell Localization and Cytotoxicity of Cerium Oxide Nanoparticles. *ACS Nano* **4,** 5321–5331 (2010).

41. Zhang, L. *et al.* Co-Delivery of Hydrophobic and Hydrophilic Drugs from Nanoparticle–Aptamer Bioconjugates. *ChemMedChem* **2,** 1268–1271 (2007).

42. Maincent, P. *et al.* Lymphatic Targeting of Polymeric Nanoparticles After Intraperitoneal Administration in Rats. *Pharm Res* **9,** 1534–1539 (1992).

43. Perez, J. M., Asati, A., Nath, S. & Kaittanis, C. Synthesis of Biocompatible Dextran-Coated Nanoceria with pH-Dependent Antioxidant Properties. *Small* **4,** 552–556 (2008).

44. Bianco, A., Kostarelos, K. & Prato, M. Applications of carbon nanotubes in drug delivery. *Current Opinion in Chemical Biology* **9,** 674–679 (2005).

45. Fernández-García, M. & Rodriguez, J. A. in *Encyclopedia of Inorganic and Bioinorganic Chemistry* (John Wiley & Sons, Ltd, 2011).

46. Sun, M., Yang, L., Jose, P., Wang, L. & Zweit, J. Functionalization of quantum dots with multidentate zwitterionic ligands: impact on cellular interactions and cytotoxicity. *J. Mater. Chem. B* **1,** 6137–6146 (2013).

47. Rocha, E. L. da, Caramori, G. F. & Rambo, C. R. Nanoparticle translocation through a lipid bilayer tuned by surface chemistry. *Phys. Chem. Chem. Phys.* **15,** 2282–2290 (2013).

48. Heidel, J. D. & Davis, M. E. Clinical developments in nanotechnology for cancer therapy. *Pharm. Res.* **28,** 187–199 (2011).

49. Kim, S. T., Saha, K., Kim, C. & Rotello, V. M. The Role of Surface Functionality in Determining Nanoparticle Cytotoxicity. *Acc. Chem. Res.* **46,** 681–691 (2013).

50. Nam, J. *et al.* Surface engineering of inorganic nanoparticles for imaging and therapy. *Advanced Drug Delivery Reviews* **65,** 622–648 (2013).

51. Xiao, K. *et al.* The effect of surface charge on in vivo biodistribution of PEG-oligocholic acid based micellar nanoparticles. *Biomaterials* **32,** 3435–3446 (2011).

52. Yang, L. *et al.* Intrinsically radiolabeled multifunctional cerium oxide nanoparticles for in vivo studies. *J. Mater. Chem. B* **1,** 1421–1431 (2013).

53. Albanese, A., Tang, P. S. & Chan, W. C. W. The Effect of Nanoparticle Size, Shape, and Surface Chemistry on Biological Systems. *Annual Review of Biomedical Engineering* **14,** 1–16 (2012).

54. Barros, A. B. de, Tsourkas, A., Saboury, B., Cardoso, V. N. & Alavi, A. Emerging role of radiolabeled nanoparticles as an effective diagnostic technique. *EJNMMI Research* **2,** 39 (2012).

55. Stockhofe, K., Postema, J. M., Schieferstein, H. & Ross, T. L. Radiolabeling of Nanoparticles and Polymers for PET Imaging. *Pharmaceuticals* **7,** 392–418 (2014).

55. Hoffman, D. et al. Intrinsically radiolabelled [59Fe]-SPIONs for dual MRI/radionuclide detection. Am J Nucl Med Mol Imaging 4, 548–560 (2014). https://creativecommons.org/licenses/by/2.0/

57. Celardo, I. *et al.* Ce$^{3+}$ ions determine redox-dependent anti-apoptotic effect of cerium oxide nanoparticles. *ACS Nano* **5,** 4537–4549 (2011).

118

58. Hirst, S. M. *et al.* Anti-inflammatory properties of cerium oxide nanoparticles. *Small* **5,** 2848–2856 (2009).

59. Hirst, S. M. *et al.* Bio-distribution and in vivo antioxidant effects of cerium oxide nanoparticles in mice. *Environ. Toxicol.* **28,** 107–118 (2013).

60. Das, S. *et al.* Cerium oxide nanoparticles: applications and prospects in nanomedicine. *Nanomedicine (Lond)* **8,** 1483–1508 (2013).

61. Eguchi, K., Setoguchi, T., Inoue, T. & Arai, H. Electrical properties of ceria-based oxides and their application to solid oxide fuel cells. *Solid State Ionics* **52,** 165–172 (1992).

62. Shin Tsunekawa, R. S. Origin of the Blue Shift in Ultraviolet Absorption Spectra of Nanocrystalline CeO2^|^minus;x Particles. *Materials Transactions, JIM* **41,** 1104–1107 (2000).

63. Izu, N., Shin, W., Matsubara, I. & Murayama, N. Development of Resistive Oxygen Sensors Based on Cerium Oxide Thick Film. *J Electroceram* **13,** 703–706 (2004).

64. Masui, T., Ozaki, T., Machida, K. & Adachi, G. Preparation of ceria–zirconia sub-catalysts for automotive exhaust cleaning. *Journal of Alloys and Compounds* **303–304,** 49–55 (2000).

65. Schubert, D., Dargusch, R., Raitano, J. & Chan, S.-W. Cerium and yttrium oxide nanoparticles are neuroprotective. *Biochem. Biophys. Res. Commun.* **342,** 86–91 (2006).

66. Heckman, K. L. *et al.* Custom Cerium Oxide Nanoparticles Protect against a Free Radical Mediated Autoimmune Degenerative Disease in the Brain. *ACS Nano* **7,** 10582–10596 (2013).

67. Das, M. *et al.* Auto-catalytic Ceria Nanoparticles Offer Neuroprotection to Adult Rat Spinal Cord Neurons. *Biomaterials* **28,** 1918–1925 (2007).

68. Zhou, X., Wong, L. L., Karakoti, A. S., Seal, S. & McGinnis, J. F. Nanoceria inhibit the development and promote the regression of pathologic retinal neovascularization in the Vldlr knockout mouse. *PLoS ONE* **6,** e16733 (2011).

69. Niu, J., Azfer, A., Rogers, L. M., Wang, X. & Kolattukudy, P. E. Cardioprotective effects of cerium oxide nanoparticles in a transgenic murine model of cardiomyopathy. *Cardiovasc. Res.* **73,** 549–559 (2007).

70. Wason, M. S. & Zhao, J. Cerium oxide nanoparticles: potential applications for cancer and other diseases. *Am J Transl Res* **5,** 126–131 (2013).

71. Sack, M. *et al.* Combination of conventional chemotherapeutics with redox-active cerium oxide nanoparticles--a novel aspect in cancer therapy. *Mol. Cancer Ther.* **13,** 1740–1749 (2014).

72. Pešić, M. *et al.* Anti-cancer effects of cerium oxide nanoparticles and its intracellular redox activity. *Chem. Biol. Interact.* **232,** 85–93 (2015).

73. Asati, A., Santra, S., Kaittanis, C., Nath, S. & Perez, J. M. Oxidase-like activity of polymer-coated cerium oxide nanoparticles. *Angew. Chem. Int. Ed. Engl.* **48,** 2308–2312 (2009).

74. Turley, S. J., Cremasco, V. & Astarita, J. L. Immunological hallmarks of stromal cells in the tumour microenvironment. *Nat Rev Immunol* **15,** 669–682 (2015).

75. Griffiths, J. R., McIntyre, D. J., Howe, F. A. & Stubbs, M. Why are cancers acidic? A carrier-mediated diffusion model for H+ transport in the interstitial fluid. *Novartis Found. Symp.* **240,** 46-62-67, 152–153 (2001).

76. Mahoney, B. P., Raghunand, N., Baggett, B. & Gillies, R. J. Tumor acidity, ion trapping and chemotherapeutics. I. Acid pH affects the distribution of chemotherapeutic agents in vitro. *Biochem. Pharmacol.* **66,** 1207–1218 (2003).

77. Tannock, I. F. & Rotin, D. Acid pH in tumors and its potential for therapeutic exploitation. *Cancer Res.* **49,** 4373–4384 (1989).

78. Rockwell, S., Dobrucki, I. T., Kim, E. Y., Marrison, S. T. & Vu, V. T. Hypoxia and radiation therapy: Past history, ongoing research, and future promise. *Curr Mol Med* **9,** 442–458 (2009).

79. Robey, I. F. *et al.* Bicarbonate increases tumor pH and inhibits spontaneous metastases. *Cancer Res.* **69,** 2260–2268 (2009).

80. Jain, R. K. Normalizing Tumor Microenvironment to Treat Cancer: Bench to Bedside to Biomarkers. *JCO* (2013). doi:10.1200/JCO.2012.46.3653

80. Massoud, T. F. & Gambhir, S. S. Molecular imaging in living subjects: seeing fundamental biological processes in a new light. Genes Dev. 17, 545–580 (2003). http://creativecommons.org/licenses/by-nc/4.0/

81. Maus, J. English: Image of the 'annihilation' process known in elementary physics. It shows how a positron (e+) is emitted from the atomic nucleus together with a neutrino (v). The positron moves then randomly through the surrounding matter where it hits several different electrons (e-) until it finally loses enough energy that it interacts with a single electron. This process is called an 'annihilation' and results in two diametrically emitted photons with a typical energy of 511 keV each. However, please note that under normal circumstances the photons are not emitted exactly diametrically (180 degrees). This is due to the remaining energy of the positron and therefore of the conservation of momentum. Wikipedia, the online encyclopedia (2009).

82. Maus, J. The image illustrates the processing principles of a positron emission tomograph (PET) commonly used in cancer diagnostics. It shows how during the annihilation process

two photons are emitted in diametrically opposite directions. These photons are registered by the scanner as soon as they arrive at the detector ring. After the registration, the data is forwarded to a processing unit which decides if two registered events are selected as a so-called coincidence event. All coincidences are forwarded to the image processing unit where the final image data is produced via mathematical image reconstruction procedures. Wikipedia, the online encyclopedia (2003).

84. Wester, H.-J. Nuclear Imaging Probes: from Bench to Bedside. *Clin Cancer Res* **13,** 3470–3481 (2007).

85. Jadvar, H. FDG PET in Prostate Cancer. *PET Clin* **4,** 155–161 (2009).

86. Kinahan, P. E. & Fletcher, J. W. PET/CT Standardized Uptake Values (SUVs) in Clinical Practice and Assessing Response to Therapy. *Semin Ultrasound CT MR* **31,** 496–505 (2010).

87. Deri, M. A., Zeglis, B. M., Francesconi, L. C. & Lewis, J. S. PET imaging with 89Zr: From radiochemistry to the clinic. *Nuclear Medicine and Biology* **40,** 3–14 (2013).

88. McRobbie, D. W. *MRI from picture to proton*. (Cambridge University Press, 2007).

89. Currie, S., Hoggard, N., Craven, I. J., Hadjivassiliou, M. & Wilkinson, I. D. Understanding MRI: basic MR physics for physicians. *Postgrad Med J* **89,** 209–223 (2013).

90. van Zijl, P. C. M. & Yadav, N. N. Chemical Exchange Saturation Transfer (CEST): what is in a name and what isn't? *Magn Reson Med* **65,** 927–948 (2011).

91. Hancu, I. *et al.* CEST and PARACEST MR contrast agents. *Acta Radiol* **51,** 910–923 (2010).

92. Chen, L. Q. *et al.* Evaluations of extracellular pH within in vivo tumors using acidoCEST MRI. *Magn Reson Med* **72,** 1408–1417 (2014).

92. Longo, D. L. et al. A General MRI-CEST Ratiometric Approach for pH Imaging: Demonstration of in Vivo pH Mapping with Iobitridol. J. Am. Chem. Soc. 136, 14333–14336 (2014). pubs.acs.org/page/policy/authorchoice/index.html

94. Longo, D. L. *et al.* Iopamidol as a responsive MRI-chemical exchange saturation transfer contrast agent for pH mapping of kidneys: In vivo studies in mice at 7 T. *Magn. Reson. Med.* **65,** 202–211 (2011).

95. Müller-Lutz, A. *et al.* Pilot study of Iopamidol-based quantitative pH imaging on a clinical 3T MR scanner. *Magn Reson Mater Phy* **27,** 477–485 (2014).

96. Wikipedia, M. at E. English: The figure explains the fluorescence phenomenon using energy level diagram. The left half shows the vibrational and electronic energy levels of an absorbing molecule. An electron in the lower energy level (ground energy level) absorb a laser photon and is transferred to an upper (excited) energy level. If this electron gives out a photon during the process of getting de-excited, then that photon is seen as a fluorescence signal. Wikipedia, the online encyclopedia (2007).

97. Zadelrob. English: Fluorescence excitation and emission spectra of 10 µM fluorescein in deionized water. Wikipedia, the free encyclopedia (2014). https://creativecommons.org/licenses/by-sa/3.0/deed.en

98. Whitaker, J. E., Haugland, R. P. & Prendergast, F. G. Spectral and photophysical studies of benzo[c]xanthene dyes: Dual emission pH sensors. *Analytical Biochemistry* **194,** 330–344 (1991).

99. Holland, J. P., Sheh, Y. & Lewis, J. S. Standardized methods for the production of high specific-activity zirconium-89. *Nucl Med Biol* **36,** 729–739 (2009).

123

100. Neufert, C., Becker, C. & Neurath, M. F. An inducible mouse model of colon carcinogenesis for the analysis of sporadic and inflammation-driven tumor progression. *Nat. Protocols* **2,** 1998–2004 (2007).

101. Raghunand, N., Mahoney, B., van Sluis, R., Baggett, B. & Gillies, R. J. Acute Metabolic Alkalosis Enhances Response of C3H Mouse Mammary Tumors to the Weak Base Mitoxantrone. *Neoplasia* **3,** 227–235 (2001).

103. Carulli, A. J., Samuelson, L. C. & Schnell, S. Unraveling intestinal stem cell behavior with models of crypt dynamics. Integrative Biology 6, 243 (2014). http://creativecommons.org/licenses/by/3.0/

103. Potten, C. S. & Grant, H. K. The relationship between ionizing radiation-induced apoptosis and stem cells in the small and large intestine. *Br J Cancer* **78,** 993–1003 (1998).

104. Hotze, E. M., Phenrat, T. & Lowry, G. V. Nanoparticle Aggregation: Challenges to Understanding Transport and Reactivity in the Environment. *Journal of Environmental Quality* **39,** 1909–24 (2010).

104. Holland, J. P. et al. Measuring the Pharmacodynamic Effects of a Novel Hsp90 Inhibitor on HER2/ neu Expression in Mice Using 89 Zr-DFO-Trastuzumab. PLOS ONE 5, e8859 (2010).

106. Holland, J. P. *et al.* 89Zr-DFO-J591 for immunoPET imaging of prostate-specific membrane antigen (PSMA) expression in vivo. *J Nucl Med* **51,** 1293–1300 (2010).

107. Börjesson, P. K. E. *et al.* Radiation Dosimetry of 89Zr-Labeled Chimeric Monoclonal Antibody U36 as Used for Immuno-PET in Head and Neck Cancer Patients. *J Nucl Med* **50,** 1828–1836 (2009).

108. Jacobson, O. *et al.* MicroPET imaging of integrin αvβ3 expressing tumors using 89Zr-RGD peptides. *Mol Imaging Biol* **13,** 1224–1233 (2011).

109. Perk, L. R. *et al.* Quantitative PET imaging of Met-expressing human cancer xenografts with 89Zr-labelled monoclonal antibody DN30. *Eur J Nucl Med Mol Imaging* **35,** 1857–1867 (2008).

110. Dijkers, E. C. *et al.* Biodistribution of 89Zr-trastuzumab and PET Imaging of HER2-Positive Lesions in Patients With Metastatic Breast Cancer. *Clinical Pharmacology & Therapeutics* **87,** 586–592 (2010).

111. Zhang, F. *et al.* Phases in Ceria–Zirconia Binary Oxide (1−x)CeO2–xZrO2 Nanoparticles: The Effect of Particle Size. *Journal of the American Ceramic Society* **89,** 1028–1036 (2006).

112. Wong, L. L. *et al.* Catalytic nanoceria are preferentially retained in the rat retina and are not cytotoxic after intravitreal injection. *PLoS ONE* **8,** e58431 (2013).

113. Peterson, C. C. & Bonte, F. J. Technetium-99m macroaggregated albumin: A new lung scanning agent. *The International Journal of Applied Radiation and Isotopes* **18,** 201–202 (1967).

114. Choi, H. S. *et al.* Renal Clearance of Nanoparticles. *Nat Biotechnol* **25,** 1165–1170 (2007).